TECHNISCHE UNIVERSITÄT DRESDEN

Langevin Dynamics Investigations of an Si(001) adapted XY Model

Master-Arbeit
zur Erlangung des Hochschulgrades
Master of Science
im Master-Studiengang Physik

vorgelegt von

Andreas Weitzel
geboren am 10.08.1999 in Fulda

Institut für Theoretische Physik
Fakultät Physik
Bereich Mathematik und Naturwissenschaften
Technische Universität Dresden
2024

Eingereicht am 02. April 2024

1. Gutachter: Prof. Dr. Ralf Schützhold
2. Gutachter: Prof. Dr. Roland Ketzmerick

Summary

Abstract

Langevin dynamics simulations are used to analyze the static and dynamic properties of an XY model adapted to the Si(001) dimers. The numerics utilise high-performance parallel computation methods on GPUs. The static exponent ν of the symmetry-broken XY model is determined to $\nu = 1.003$. A phase diagram for the critical temperature T_c as a function of the amplitude of the symmetry-breaking potential h shows the behaviour predicted by renormalization group calculations. The ratio of the correlation length amplitudes in the two spatial directions $\xi_{\parallel}^{+}$ and $\xi_{\perp}^{-}$ differs greatly from the Ising model. The dynamic critical exponent z is determined to be $z = 2.18$ and, together with ν, shows the behaviour of the Ising universality class. The quench exponent of a cool-down deviates with 0.445 strongly from the expected Kibble-Zurek scaling. The quench exponent shows no dependence on the damping η or h.

Zusammenfassung

Langevin-Dynamik-Simulationen werden zur Untersuchung der statischen und dynamischen Eigenschaften eines an die Si(001)-Dimere angepassten XY Modells verwendet. Die Numerik nutzt hochleistungsfähige parallele Berechnungsmethoden mittels GPUs. Der statische Exponent ν des symmetriegebrochenen XY Modells wird zu $\nu = 1.003$ bestimmt. Das Phasendiagramm für die kritische Temperatur T_c in Abhängigkeit der Amplitude des symmetriebrechenden Potentials h zeigt durch Renormierungsgruppen-Rechnung vorhergesagtes Verhalten. Das Verhältnis der Korrelationsamplituden in den zwei Raumrichtungen $\xi_{\parallel}^{+}$ und $\xi_{\perp}^{-}$ unterscheidet sich stark vom Ising-Modell. Der dynamische kritische Exponent z wird auf $z = 2.18$ bestimmt und zeigt, zusammen mit ν, das Verhalten der Ising Universalitätsklasse. Der Quench-Exponent bei Abkühlung weicht mit 0.445 stark vom erwarteten Kibble-Zurek-Wert ab. Der Quench-Exponent zeigt keine Abhängigkeit von der Dämpfung η oder h.

Contents

1 Introduction

1.1 Motivation

In the area of semiconductor technology, silicon has become the cornerstone material driving the innovations that power our modern world, the *Silicon Age* [1]. Its versatility, reliability, and abundance have solidified its position as the basic building block of the semiconductor industry, making silicon responsible for substantial recent developments [2]. Its semiconducting properties facilitate the creation of wafers and integrated circuits, which are the centerpieces of computers, smartphones, and virtually any current electronic device.

The most important part of integrated circuits are transistors. They function as switches which make up binary numbers and logic gates that every processor uses to do math. The speed at which processors perform calculations is majorly influenced by the number of transistors available [3]. Therefore, the pursuit of further miniaturization is crucial for performance enhancement. Experimental transistors approach wire diameters of about 2.5 nm [4]. This is close to the diameter of an individual silicon atom and silicon's lattice constant of about 0.2 nm [5] or 0.55 nm [6] respectively. At those scales, surface effects play an ever-increasing role in influencing the behavior and conductivity of the wires. Indeed, manufacturers have difficulties controlling the current flow through the channels of the transistors. Hence, a better understanding of the behavior of the surface is critical to ensure progress in classical computing.

Especially the Si(001) surface of monocrystalline silicon is important since it forms an interface with the oxide layer in transistors that isolates silicon wires from their environment. Moreover, silicon wafers are cut along the (001) plane. The orientation of the cut is important due to the fact that many of a crystal's structural and electronic properties are highly anisotropic.

While static properties of Si(001), e.g. possible surface configurations, their energies and electronic structures are thoroughly investigated [7, 8, 9, 10], the dynamic properties [11] are not yet well understood. The surface undergoes a continuous order-disorder phase transition with Ising critical exponents [12] between two surface geometries [13], leading to striking dynamic behavior at the critical point. A rich phenomenon to consider is the Kibble-Zurek mechanism [14, 15, 16] which describes the unavoidable non-adiabatic evolution of systems as they

cross phase boundaries. The time at which the system undergoes this transition is directly related to the size of ordered domains, that in turn influence the semiconducting [17, 18, 19] properties of the surface.

1.2 Thesis Structure

This thesis aims to contribute to the understanding of the dynamic behavior of Si(001) during a cooling quench. The already existing discrete Ising-like description of the surface is extended to a continuous XY-like model and adapted to the silicon surface. Well established molecular dynamics methods are used in combination with state-of-the-art parallel programming and GPU acceleration techniques to overcome the numerous numerical obstacles that are inherent to the nature of phase transitions. The used Langevin-type stochastic differential equations are motivated from a quantum mechanics point of view. Renormalization group techniques are discussed to set a theoretical baseline for the investigation of the phase transition.

Chapter 2 firmly concludes the current viewpoint and knowledge of the Si(001) surface and its order-disorder phase transition. Chapter 3 explores the renormalization group description of phase transitions to create a theoretical understanding for the following. It introduces the concept of universality and finite-size scaling methods that are used to investigate and interpret the simulation results. Chapter 4 explains the used numerics and derives the Langevin equation using open quantum systems considerations. Moreover, the anisotropic XY model is introduced and adapted to Si(001). The numerical implementation on graphical processing units is laid out in the beginning of Chapter 5. Subsequently, the results of various investigations like dynamic quenches, as well as static measurements, are presented. Chapter 6 summarizes the main points of the thesis and provides an outlook for further research. The appendix contains calculations to several parts of the work as well as benchmarks for the simulation.

2 The Si(001) Surface

2.1 Surface Reconstruction

Below a temperature of $T = 1687$ K, silicon crystallizes in a diamond cubic structure, as shown in Fig. 2.1, with a lattice constant of $a = 5.431$ Å [6]. When cutting this crystal structure along the crystallographic (001) plane, the resulting system exhibits a surface reconstruction. Surface atoms are left in a high-energy state with two dangling bonds. One of those bonds can be invested into forming a dimer with the neighboring Si atom in (110) direction [20], leading to a large surface energy reduction of roughly 1.8 eV per dimer [7, 21, 22]. The resulting dimers can further reduce their energy by buckling vertically. The dimers tilt to an angle of about 18° [7, 8], which lowers the surface energy by another 0.15 eV [23] per dimer. A charge transfer of approximately $0.1e$ [12, 24] is induced by the buckling.

Theoretical [7, 8, 23, 12] and experimental (low energy electron diffraction [9, 26, 12] and scanning tunnel microscope [27, 10]) have found the $c(4 \times 2)$ reconstruction, shown in Fig. 2.2 (b), to be the lowest energy geometry. It minimizes the interaction energy as well as the surface stress [8]. Si(001) was mapped onto the exactly solvable two dimensional Ising model in previous research [28, 8, 29, 11, 23]. In this framework, the dimer interaction is described by an effective coupling J (see subsection 4.4.1). The alternative buckling in both directions suggests an antiferromagnetic interaction along (110), $J_{\parallel}$, and across $(1\bar{1}0)$, $J_{\perp}$, the dimer rows, but the interaction across the row is actually ferromagnetic. However, the dimer interactions are strongly anisotropic, with $J_{\parallel}$ being much larger than $J_{\perp}$, causing a guaranteed alternating buckling in (110) direction. The ferromagnetic diagonal interactions $J_{\times}$ overpower $J_{\perp}$, so that diagonal alignment is preferred, which in

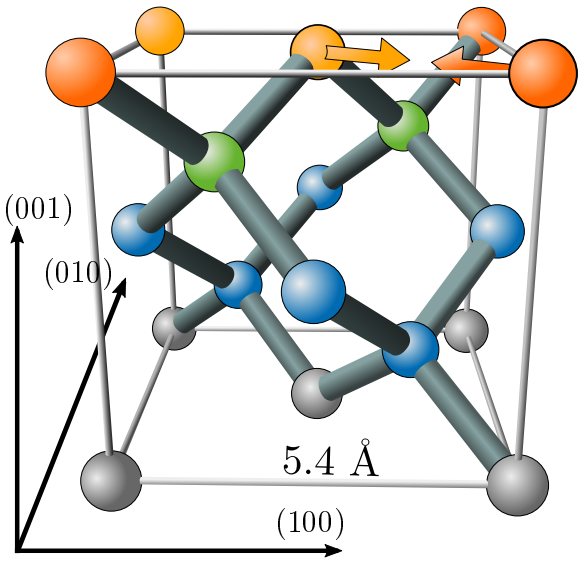

Figure 2.1: The crystalline structure of Si in its solid state is shown [25]. The orange silicon atoms dimerize during reconstruction of the (001) surface. The coordinate axes are denoted by their Miller indices and normal to their corresponding crystallographic planes. The coloring corresponds with Fig. 2.2

turn implies anti-alignment in $(1\bar{1}0)$ direction. It has been suggested that the dimer interaction is of dipole kind [8].

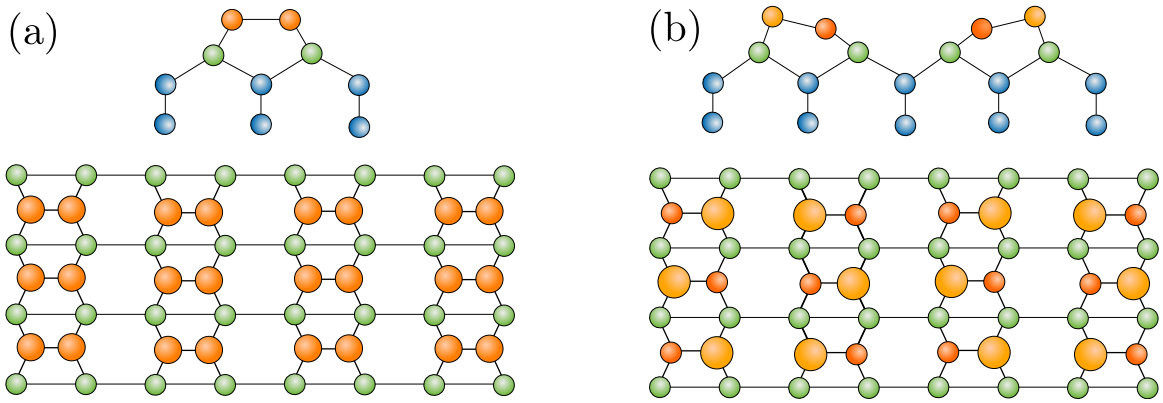

Figure 2.2: Si(001) surface geometries are shown from a side and top down perspective. **(a)** The formation of dimers results in the symmetric $p(2 \times 1)$ reconstruction and saves a large amount of 1.8 eV per dimer compared to the non-dimerized structure. **(b)** The dimers are unstable to vertical buckling. The buckling pattern that was found to have the lowest surface energy is the $c(4 \times 2)$ reconstruction. The coloring of the silicon atoms corresponds with Fig. 2.1. The surfaces are named using Wood's notation for overlayers. Adapted from [12].

2.2 Phase Transition of the Si(001) Surface

The silicon (001) surface exhibits an order-disorder phase transition from the disordered $p(2\times1)$ phase, as shown in Fig. 2.2 (a), to the ordered $c(4\times2)$ reconstruction at a critical temperature of about $T_c \approx 200$ K [13, 28]. The $p(2 \times 1)$ structure is short term for the disordered phase since fast flipping of the dimers at a frequency of about 10^{11} Hz [22] let the system appear to be in the $p(2 \times 1)$ state at high-temperature measurements. This continuous phase transition will be of central importance in the following discussion.

Below T_c, the strong anisotropy leads to long streaks of order along the dimer rows and short domains of order across the dimer rows. The parallel dimension of ordered patches is larger than the perpendicular direction by a factor of five [28]. Brand et al. [12, 28] find good agreement between the experimentally measured static critical properties of the Si(001) phase transition and the Ising universality class. Schaller et al. [11] employ kinetic Monte Carlo methods [30] to extract a dynamic Kibble-Zurek exponent that matches the expectation for the Ising model.

To understand the transition of the Si(001) surface, general knowledge of phase transitions will be laid out in the following.

3 Phase Transitions

The term *phase transition* describes the process of transition between system states by changing an external parameter, e.g. pressure p or temperature T. Common types are transitions from an unordered to an ordered state after cooling a system below its critical temperature T_c, like the transition from paramagnets to ferromagnets. Intuitively, the transitions occur as a result of free energy $F = U - TS$ minimization. At high temperatures, entropy S dominates, leading to unordered states, but, at low temperatures, the impact of the internal energy U is dominant. The minimization of U typically leads to a form of *symmetry-breaking* order dictated by the microscopic Hamiltonian. The degree of order is quantified by the *order parameter*, e.g. the magnetization in the case of ferromagnets.

Mathematical Definition

Consider a general system in the state Ω described by the effective Hamiltonian

$$\beta H = \beta \sum_{i}^{d} J_i \; G_i(\Omega) = \sum_{i}^{d} K_i \; G_i(\Omega), \tag{3.1}$$

with $\beta = 1/k_B T$ being the inverse temperature. The energy of the system is characterized by d effective coupling constants $K_i = \beta J_i$ and functionals of the microscopic state G_i. Let now N denote the number of components, or, equivalently, the number of lattice sites, and V the volume of the system in question. The *thermodynamic limit* $N \to \infty$ and $V \to \infty$ describes the limit to infinitely large systems while keeping the density N/V constant. For a system dependent on a set of $[K]$, the free energy per site f is defined as

$$f([K]) = \lim_{N \to \infty} \frac{F([K])}{N} \; . \tag{3.2}$$

With f, a precise definition of phase boundaries is possible. The coupling constants $[K]$ span the so called *phase space*. In this d-dimensional phase space, the free energy density f is analytic almost everywhere except for the possibility of non-analyticities at certain points, lines, planes, etc. up to dimensionality $d - 1$. The connected areas of analyticity are called *phases* and non-analyticities with dimension $d - 1$ are called *phase boundaries* or *critical manifolds* [31]. Since f has to be continuous everywhere, the phase boundaries come in two

classes:

1. At least one of the first derivatives $\frac{\partial f}{\partial K_i}$ is discontinuous across the phase transition. This case belongs to the *first-order phase transition*.
2. All derivatives $\frac{\partial f}{\partial K_i}$ are continuous. This transition is called the *continuous phase transition*.

The phase transition of the silicon surface is part of the continuous phase transitions. As the thermodynamic limit is never obtained, descriptions using f are not always reliable. The correlation length ξ, which describes the spatial extent of fluctuations in the system, gives a criterion for accurate predictions. If the system size L is much greater than the correlation length $\xi \ll L$, the considered system can be expected to exhibit the ideal behavior described by f.

Phase transitions display rich phenomena like the divergence of the correlation length ξ at the critical point. The reason for the universality of this behavior across different systems will be outlined in the next section by using renormalization group theory.

3.1 Renormalization Group Considerations

The *renormalization group* (RG) theory is a general framework used to study phase transitions and particle physics. It employs scale invariance arguments, i.e. the self-similarity characteristics of systems at different length scales, to investigate their properties. It enables to explain the origins of singular behavior in phase transitions and universality. These properties are used extensively throughout this research and, therefore, the foundations will be presented briefly.

Consider an infinite two dimensional lattice with Ising-like spins s_{mn} on each site, described by a Hamiltonian of form as in Eq. (3.1). The sites are denoted by a tuple of indices (m, n). First, we follow Kadanoff [32] and divide the system into squares of length $\ell > 1$ expressed in lattice spacing units a. The resulting blocks B_{ij} are denoted by a new set of indices (i, j). Their ℓ^2 spins are mapped onto a single block spin

$$S_{ij}^{(\ell)} \propto \sum_{(m,n)\in B_{ij}} s_{mn} \ . \tag{3.3}$$

The obtained $S_{ij}^{(\ell)}$ define a new Ising system, but on a different length scale with a new lattice spacing like shown in Fig. 3.1. Now, it is proposed that there is a set of coupling constants $[K^{(\ell)}]$, so that the total free energy stays the same.

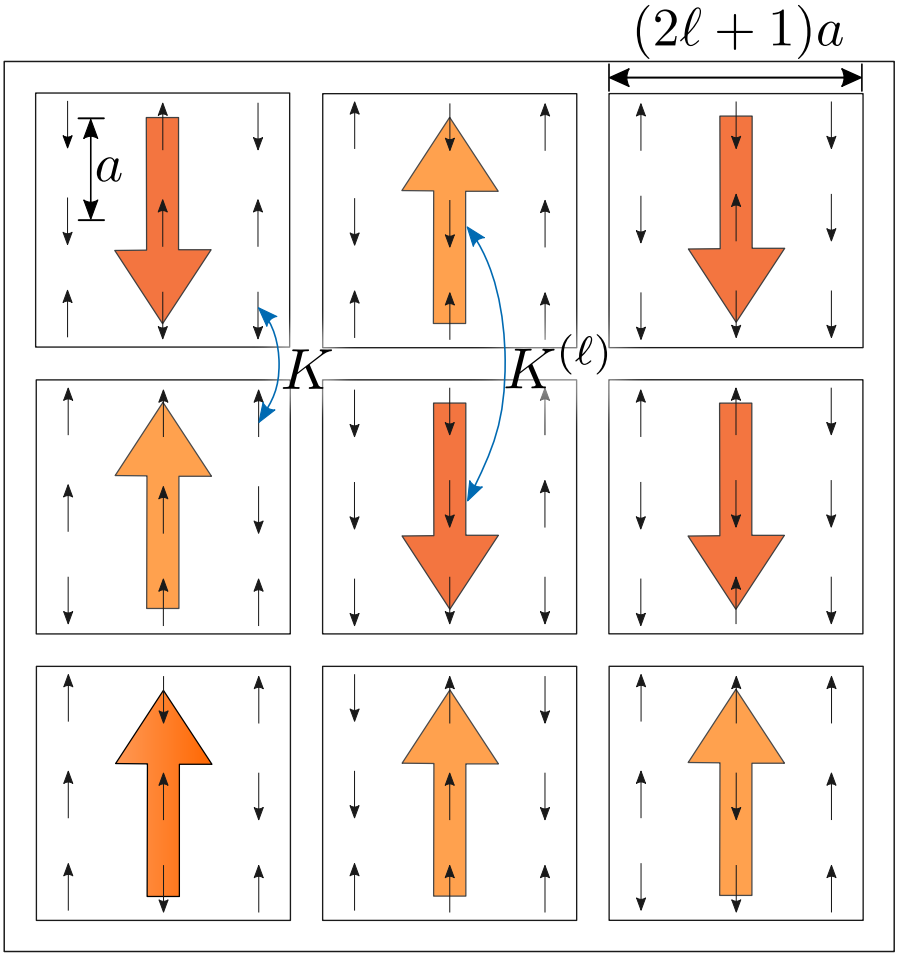

Figure 3.1: In Kadanoff's block spin picture, blocks B_{ij} of Ising-spins s_{mn} are combined to a composite spin $S_{ij}^{(\ell)}$. One possible RG transformation $R^{(\ell)}$ would be to group $(2\ell+1)$ spins and map $S_{ij}^{(\ell)} = \text{sign}\left(\sum_{(m,n)\in B_{ij}} s_{mn}\right)$. Under the RG transformation the coupling constants change from K to $K^{(\ell)} = R^{(\ell)}(K)$.

In terms of the free energy density we can state

$$f\left([K]\right) = \ell^{-2} f\left([K^{(\ell)}]\right) \ . \tag{3.4}$$

The free energy density after the transformation has to increase by a factor ℓ^2 as it is expressed in an ℓ-times larger length scale. The same considerations are made for the correlation length, resulting in

$$\xi\left([K]\right) = \ell \xi\left([K^{(\ell)}]\right) \ . \tag{3.5}$$

In addition to preserving the free energy, an RG transformation has to reflect the symmetries of the system to ensure that the transformed Hamiltonian keeps the original symmetries. Suppose we know a valid RG transformation $R^{(\ell)}$, so that

$$[K^{(\ell)}] = R^{(\ell)}([K]) \ . \tag{3.6}$$

An RG transformation reduces the system degrees of freedom to $N^{(\ell)} = \ell^{-2} N$. Tracing out all degrees of freedom with successive transformations, in principle, provides knowledge of the partition function. Even though each transformation is analytic, the singularities of phase transitions can arise after an infinite number of RG iterations that are required to integrate all degrees of freedom in the thermodynamic limit. Applying several RG transformations traces a trajectory in coupling constant space $[K^{(\ell_1)}] \to [K^{(\ell_2)}] \to ... \to [K^{(\ell_n)}]$, called the *RG flow*. This trajectory is almost always attracted to fixed points. The behavior of a system near a fixed point is the origin of scaling and enables the extraction of important information, e.g. the shape of the phase diagram.

A fixed point of the RG map satisfies

$$[K^{(*)}] = R^{(\ell)}\left([K^{(*)}]\right) \ . \tag{3.7}$$

At this point the correlation length transforms according to

$$\xi\left([K^{(*)}]\right) = \xi\left([K^{(*)}]\right)/\ell \ , \tag{3.8}$$

so that the correlation length either has to be 0 or ∞. The same is true for the free energy density. In proximity of a fixed point, the i-th coupling constant K_i and its transformation $K_i^{(\ell)}$ is written as

$$K_i = K_i^{(*)} + \delta K_i \qquad \text{and} \qquad K_i^{(\ell)} = R^{(\ell)}(K_i^{(*)} + \delta K_i) = K_i^{(*)} + \delta K_i^{(\ell)} \ . \tag{3.9}$$

In general, the RG Transformation of K_i is dependent on all K, so that

$$K_i^{(\ell)} = K_i^{(\ell)}([K]) = K_i^{(\ell)}(K_1^{(*)} + \delta K_1, K_2^{(*)} + \delta K_2, ...). \tag{3.10}$$

The Taylor expansion of $K_i^{(\ell)}$ around the fixed point $[K^{(*)}]$ yields the linearized RG Transformation

$$K_i^{(\ell)} = K_i^{(*)} + \sum_j \left.\frac{\partial K_i^{(\ell)}}{\partial K_j}\right|_{K_j=K_j^{(*)}} \delta K_j + O((\delta K_j)^2) = K_i^{(*)} + \delta K_i^{(\ell)} + O((\delta K_j)^2)\ . \tag{3.11}$$

Omitting terms quadratic or higher in δK_j identifies

$$\delta K_i^{(\ell)} = \sum_j \left.\frac{\partial K_i^{(\ell)}}{\partial K_j}\right|_{K_j=K_j^{(*)}} \delta K_j\ . \tag{3.12}$$

We write the partial derivatives as a matrix

$$M_{ij}^{(\ell)} = \left.\frac{\partial K_i^{(\ell)}}{\partial K_j}\right|_{K_j=K_j^{(*)}}\ , \tag{3.13}$$

and construct an eigenvalue problem

$$M^{(\ell)}\boldsymbol{k}_\sigma = \lambda_\sigma^{(\ell)}\boldsymbol{k}_\sigma\ , \tag{3.14}$$

where σ labels the eigenvalues. The eigenvectors $\boldsymbol{k}_\sigma$ are printed in bold letters. Two consecutive RG Transformations by l_1 and l_2 have to yield the same result as one by $l_1 l_2$, implying that

$$M^{(\ell_1)}M^{(\ell_2)} = M^{(\ell_2)}M^{(\ell_1)} = M^{(\ell_1\ell_2)}\ . \tag{3.15}$$

Since the matrices commute and, therefore, share a set eigenvectors, the corresponding eigenvalues satisfy

$$\lambda_\sigma^{(\ell_1)}\lambda_\sigma^{(\ell_2)} = \lambda_\sigma^{(\ell_1\ell_2)}\ . \tag{3.16}$$

Differentiating Eq. (3.16) with respect to l_2 yields

$$\frac{\mathrm{d}}{\mathrm{d}l_2}\left(\lambda_\sigma^{(\ell_1)}\lambda_\sigma^{(\ell_2)}\right) = \lambda_\sigma^{(\ell_1)}\left(\frac{\mathrm{d}}{\mathrm{d}l_2}\lambda_\sigma^{(\ell_2)}\right) + \left(\frac{\mathrm{d}}{\mathrm{d}l_2}\lambda_\sigma^{(\ell_1)}\right)\lambda_\sigma^{(\ell_2)} = \left(\frac{\mathrm{d}}{\mathrm{d}l_2}\lambda_\sigma^{(\ell_2)}\right)\lambda_\sigma^{(\ell_1)} \tag{3.17}$$

for the left hand side and

$$\frac{\mathrm{d}}{\mathrm{d}l_2}\lambda_\sigma^{(\ell_1\ell_2)} = \frac{\mathrm{d}}{\mathrm{d}(l_2 l_1)}\lambda_\sigma^{(\ell_1\ell_2)}\frac{\partial}{\partial l_2}(l_1 l_2) = l_1\frac{\mathrm{d}}{\mathrm{d}(l_1 l_2)}\lambda_\sigma^{(\ell_1\ell_2)} \tag{3.18}$$

for the right hand side. Setting $l_2 = 1$ in Eq. (3.16) gives $\lambda_\sigma^{(\ell_1)}\lambda_\sigma^{(1)} = \lambda_\sigma^{(\ell_1)}$, resulting in the conclusion that $\lambda_\sigma^{(1)} = 1$. By inserting, the differential equation

$$\frac{\mathrm{d}}{\mathrm{d}l_2}\lambda_\sigma^{(\ell_2)}\bigg|_{l_2=1}\lambda_\sigma^{(\ell_1)} = y_\sigma\lambda_\sigma^{(\ell_1)} = l_1\frac{\mathrm{d}}{\mathrm{d}l_1}\lambda_\sigma^{(\ell_1)} \tag{3.19}$$

with

$$y_\sigma = \frac{\mathrm{d}}{\mathrm{d}l_2}\lambda_\sigma^{(\ell_2)}\bigg|_{l_2=1} \tag{3.20}$$

is obtained. A solution to Eq. (3.19) is

$$\lambda_\sigma^{(\ell)} = \ell^{y_\sigma}\ , \tag{3.21}$$

with y_σ being independent of ℓ. This is an important result in the process of showing the origin of scaling. The $\boldsymbol{k}_\sigma$ are vectors in the coupling constant space, so Eq. (3.14) indicates that some δK_i grow and some shrink when applying RG transformations, depending on the eigenvalue $\lambda_\sigma^{(\ell)}$. Three cases are distinguished:

1. *Relevant* directions and eigenvalues: $|\lambda_\sigma^{(\ell)}| > 1$, meaning that $y_\sigma > 0$ and δK in direction of $\boldsymbol{k}_\sigma$ grow.
2. *Irrelevant* directions and eigenvalues: $|\lambda_\sigma^{(\ell)}| < 1$, meaning that $y_\sigma < 0$ and δK in direction of $\boldsymbol{k}_\sigma$ shrink.
3. *Marginal* directions and eigenvalues: $|\lambda_\sigma^{(\ell)}| = 1$, meaning that $y_\sigma = 0$ and δK in direction of $\boldsymbol{k}_\sigma$ do not change.

After many iterations, only the relevant eigenvalues will be important, as shrinking δK_i will not impact the RG flow significantly. If we differ from the fixed point in a relevant direction, the distance to the fixed point will increase and the RG transformation flow will move away from the fixed point. Deviations in irrelevant direction flow into the fixed point.

A simplified understanding can be achieved for a system satisfying

$$\frac{\partial K_i^{(\ell)}}{\partial K_j}\bigg|_{K_j=K_j^{(*)}} = \delta_{ij}\frac{\partial K_j^{(\ell)}}{\partial K_j}\bigg|_{K_j=K_j^{(*)}}\ , \tag{3.22}$$

so that $M^{(\ell)}$ becomes diagonal and the eigendirections $\boldsymbol{k}_\sigma$ point along the axes of the phase space defined by $[K]$. If the eigenvalue $\lambda_\sigma^{(\ell)}$ to $\boldsymbol{k}_\sigma$ is larger than one, the coupling K_σ will grow. In this case, K_σ is a relevant coupling constant.

Consider a system with only one coupling constant $K = J/k_BT$, or, equivalently, just the

temperature T, and choose T in the vicinity of a fixed point $T^{(*)}$. Apply a RG transformation to T and consider the difference

$$T^{(\ell)} - T^{(*)} = R^{(\ell)}(T) - T^{(*)} \ . \tag{3.23}$$

Using Eq. (3.11), we can rewrite

$$R^{(\ell)}(T) = T^{(*)} + \delta T^{(\ell)} = T^{(*)} + \left.\frac{\partial T^{(\ell)}}{\partial T}\right|_{T=T^{(*)}} \delta T = T^{(*)} + \lambda^{(\ell)} \delta T \ , \tag{3.24}$$

since $M^{(\ell)}$ has only one component and δT is therefore automatically in eigenvector direction with eigenvalue

$$\lambda^{(\ell)} = \left.\frac{\partial R^{(\ell)}(T)}{\partial T}\right|_{T=T^{(*)}} \ . \tag{3.25}$$

Equation (3.23) then becomes

$$\varepsilon^{(l)} = \lambda^{(\ell)} \varepsilon \overset{\text{Eq. (3.21)}}{=} \varepsilon l^{y_\varepsilon} \ , \tag{3.26}$$

in terms of the *reduced temperature* $\varepsilon = \frac{T - T^{(*)}}{T^{(*)}}$. After n RG iterations, this gives

$$\varepsilon^{(nl)} = (l^{y_\varepsilon})^n \, \varepsilon \ . \tag{3.27}$$

Now consider again the transformation of the correlation length after n RG transformations

$$\xi(\varepsilon) = l^n \xi(\varepsilon^{nl}) = l^n \xi(l^{n y_\varepsilon} \varepsilon) \ . \tag{3.28}$$

Substituting $\tau = l^{n y_\varepsilon} \varepsilon$ into Eq. (3.28) yields

$$\xi(\varepsilon) = \tau^{1/y_\varepsilon} \varepsilon^{-1/y_\varepsilon} \xi(\tau) =: \varepsilon^{-1/y_\varepsilon} F_\xi(\tau^{1/y_\varepsilon}) \ , \tag{3.29}$$

with a scaling function $F_\xi(\tau^{1/y_\varepsilon})$. Equation (3.29) shows that the correlation length diverges at the critical point $\varepsilon \to 0$. This is the origin of the singular behavior of phase transitions! Using Eq. (3.26) and (3.25), a valid RG transformation $R^{(\ell)}$ directly provides the exponent y_ε via

$$y_\varepsilon = \frac{1}{l} \ln \left(\left.\frac{\partial R^{(\ell)}(T)}{\partial T}\right|_{T=T^{(*)}} \right) \ . \tag{3.30}$$

The only restrictions imposed on $R^{(\ell)}$ were that it keeps the total free energy invariant, and that it reflects the symmetries of the system. Those properties do not depend on the microscopic details of the considered system, which is the reason for universality.

3.2 Universality and Static Scaling

The last section traced the origin of universality and scaling in phase transitions. This section will deal with the term *universality* and its implications in more detail.

Scaling laws like Eq. (3.29) can be derived for various system quantities. In the context of phase transitions, *static scaling* describes the power law dependence of a system quantity **in equilibrium**, e.g. the correlation length ξ, on a coupling parameter, e.g. the temperature T. The exponent of this power law is called the *critical exponent*. Some important scaling relations are shown in Table 3.1. Comparing the scaling law of ξ with Eq. (3.29) identifies

$$\frac{1}{y_\varepsilon} = \nu \ . \tag{3.31}$$

The prefactors of the power laws are called the *critical amplitudes* and ν, α, etc. are the mentioned critical exponents. The superscript $\pm$ denotes whether the phase transition is approached from below $(-)$ or above $(+)$ the critical temperature T_c. The critical exponents are the same on both sides of the transition, but the amplitudes vary.

The scaling laws are only valid in the thermodynamic limit for $\varepsilon \to 0$, as the derivation in Section 3.1 assumed that the system is in the vicinity of a critical point. Otherwise, they exhibit **corrections to scaling** [33, 34] which result from irrelevant and marginal eigenvalues of the RG transformations as well as *finite-size* corrections [35, 31].

Systems that share the same set of critical exponents belong to the same *universality class*. Section 3.1 showed that the exponents can be calculated solely from the RG transformation which suggests that systems with similar transformations exhibit similar critical behavior. Indeed it is found that the universality class of a system only depends on

- the **symmetry group** of the system Hamiltonian,
- the **dimensionality** of the problem, and
- whether the interaction between the components is **short-ranged**, usually meaning that the interaction at distance r decays faster than r^{-2}.

In contrast to the critical exponents, the critical amplitudes are not universal, but their ratios, e.g. ξ^+/ξ^-, are.

The concept of universality is practical to investigate real systems at the critical point. Due to scale invariance and self similarity, the microscopic dynamics of a system become irrelevant at $\varepsilon = 0$. Its behavior can then be approximated by a simplified, ideally exactly solvable, model.

Table 3.1: Some important scaling laws are summarized in the notation of [33], except for ξ. The universal critical exponents α, β, etc. are the same above and below the phase transition. In contrast, the nonuniversal critical amplitudes may differ at different sides of the critical point. Hence, they are labeled with a superscript $\pm$. The dimensionality is denoted by d.

Name	Symbol	Scaling
specific heat	C_H	$T_c C_H \approx A^{\pm}\lvert\varepsilon\rvert^{-\alpha}$
order parameter	Ψ, M	$\lvert M\rvert \approx B\lvert\varepsilon\rvert^{-\beta}$
susceptibility	χ	$\chi \approx C^{\pm}\lvert\varepsilon\rvert^{-\gamma}$
correlation length	ξ	$\xi \approx \xi^{\pm}\lvert\varepsilon\rvert^{-\nu}$
two-point correlation function	$C(\vec{r})$	$C(\vec{r}) \propto \lvert\vec{r}\rvert^{-d+2-\eta}$

The extraction of critical exponents is notoriously difficult for various reasons, one being the inaccessibility of the thermodynamic limit, another *critical slowing down* (see Section 3.4). The following section will explain the mentioned finite-size corrections to static scaling and illustrate how they can be used to analyze critical exponents.

3.3 Finite-Size Scaling and Critical Exponent Extraction

3.3.1 Extension to Finite Systems

The upcoming numerical implementation is limited in system size and computation time. The topic of *finite-size scaling* (FSS) analyzes the deviations of finite systems from the ideal behavior. It can be employed to determine critical properties and will be useful when evaluating the simulation.

The system size L transforms after RG transformation according to

$$R^{(\ell)}(L) = L^{(l)} = L/l \ , \tag{3.32}$$

analogous to the correlation length. Extending the transformation of the free energy density of Eq. (3.4) by a dependence on the system size yields

$$f\left([K], L^{-1}\right) = l^{-2} f\left([K^{(l)}], {L^{(l)}}^{-1}\right) = l^{-2} f\left([K^{(l)}], lL^{-1}\right) \ , \tag{3.33}$$

the finite-size scaling of f. Let $K_1 = \varepsilon$ be the reduced temperature. Close to the critical point Eq. (3.26) can be used to write Eq. (3.33) in terms of eigenvalues

$$f\left(\varepsilon, K_2, ..., L^{-1}\right) = l^{-2} f\left(\varepsilon l^{y_\varepsilon}, K_2 l^{y_2}, ..., lL^{-1}\right) \ . \tag{3.34}$$

The system size behaves like a relevant coupling constant with an eigenvalue of

$$\lambda_L = l \ , \qquad \text{implying that} \qquad y_L = 1 \ . \tag{3.35}$$

Accordingly, the system size has to be tuned to criticality for the phase transition to occur. Like ε, the inverse system size has to be set to zero $L^{-1} = 0$ which is equivalent to taking the thermodynamic limit. As a result, real, finite systems deviate from the behavior dictated by scaling laws. The actual correlation length cannot outgrow the system size $\xi_L \leq L$, so the divergence of ξ is rounded at the phase transition. In addition, the peak of $\xi_L(T)$ is shifted [35]. The ideal behavior of ξ is sketched versus the behavior of a finite system in Fig. 3.2.

Now consider Eq. (3.28) extended by L-dependence, reading

$$\xi(\varepsilon, L^{-1}) = l\xi(\varepsilon l^{y_\varepsilon}, lL^{-1}) = \varepsilon^{-\nu} F_\xi(L^{-1}\varepsilon^{-\nu}) \ , \tag{3.36}$$

with F_ξ as in Eq. (3.29). Introducing a new scaling function $F' = (L\varepsilon^\nu)^{-1} F_\xi$ yields

$$\xi(\varepsilon, L^{-1}) = \varepsilon^{-\nu}(L\varepsilon^\nu) F'(L\varepsilon^\nu) = L F'(L\varepsilon^\nu) \ . \tag{3.37}$$

In the limit $L \to \infty$ and close to $\varepsilon = 0$, ξ has to scale like $\xi(\varepsilon, 0) \propto \varepsilon^{-\nu}$ implying that

$$\lim_{L\to\infty} \lim_{\varepsilon\to 0} F'(L\varepsilon^\nu) \propto (L\varepsilon^\nu)^{-1} \ . \tag{3.38}$$

The correlation length is capped for finite L so that at the critical point $\xi(0, L^{-1}) \propto L$. For F' this means

$$\lim_{\varepsilon\to 0} F'(L\varepsilon^\nu) \propto \text{const.} \ , \tag{3.39}$$

showing that the scaling function does not diverge. Therefore, a Taylor expansion around $\varepsilon = 0$ is reasonable and results in

$$\frac{L}{\xi(\varepsilon, L^{-1})} = A + B\varepsilon L^{1/\nu} + O(\varepsilon^2) \ . \tag{3.40}$$

That equation is an important result, since it can be used to calculate two central quantities. Firstly, curves of $L/\xi(\varepsilon, L^{-1})$ for different L intersect at the critical point $\varepsilon = 0$. Hence, by determining this intersection, one can extract the critical temperature T_c, which is usually not known a priori. Secondly, by computing the gradient

$$\frac{\partial}{\partial\varepsilon}\left(\frac{L}{\xi(\varepsilon, L^{-1})}\right) = BL^{1/\nu} \tag{3.41}$$

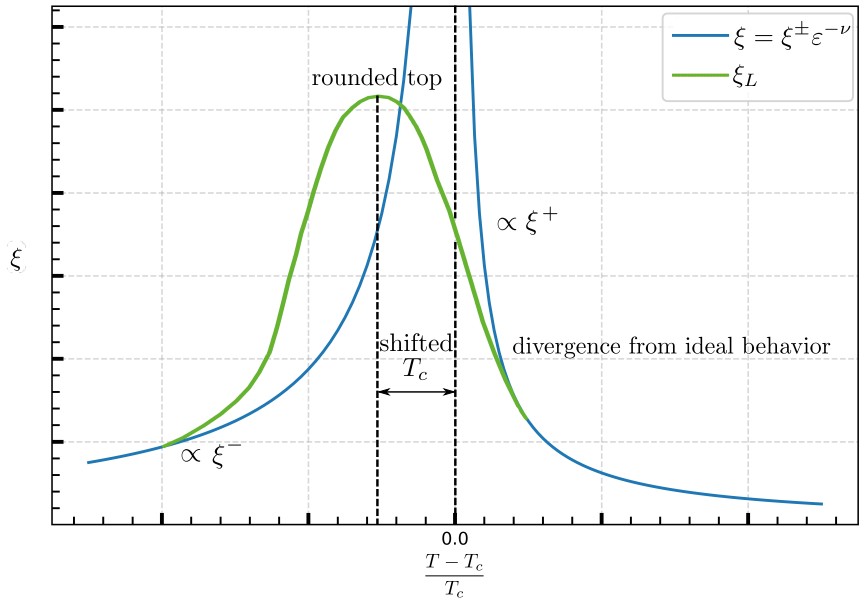

Figure 3.2: The equilibrium correlation length ξ is shown versus the reduced critical temperature. In the thermodynamic limit, ξ diverges at the critical point according to a power law, as depicted by the blue line. For finite systems, the singularity of ξ appears rounded as shown by the green curve. The peak position is shifted to an effective critical temperature.

for various L, one can determine the critical exponent ν. This method is more reliable than, for example, trying to fit to the original scaling law Eq. (3.29) because of the reasons mentioned at the end of Section 3.2.

3.3.2 Binder Cumulant

Finite-size scaling laws like Eq. (3.40) can be derived for any thermodynamic quantity [33, 36]. The Binder cumulant U_L, introduced by K. Binder in [37], is frequently used to investigate simulations. It is defined as

$$U_L = \frac{\langle M_L^4 \rangle}{\langle M_L^2 \rangle^2} \,, \tag{3.42}$$

with M_L being the lattice average

$$M_L = \frac{1}{N_L} \sum_i s_i \tag{3.43}$$

of a system of size L with N_L lattice sites. The lattice sites are characterized by s_i. The ensemble average $\langle \cdot \rangle$ denotes the mean of infinitely many system realizations. Its finite-size

scaling is analogous to Eq. (3.40) given by

$$U_L = U^* + U\varepsilon L^{1/\nu}\left(1 + WL^{-\omega} + ...\right) \ , \tag{3.44}$$

including corrections resulting out of the largest irrelevant eigenvalue $1/|y_1| = \omega$ [38]. To extract the critical exponent ν, a linear fit to

$$\ln\left(\frac{\partial U_L}{\partial \varepsilon}\right) \approx \ln\left(UL^{1/\nu}\right) = \ln(U) + \frac{1}{\nu}\ln(L) \tag{3.45}$$

is performed. For Ising lattices, it can be shown [37] that the cumulant has a value of $U_L = 1$ far below the critical temperature and approaches $U_L = 3$ for high temperatures. In between, cumulants for different L exhibit an intersection at $U_L = U^*$. These implications can be generalized to spin dimensionalities larger than one [39] and have been shown to be consistent with the XY model [40, 41]. The Binder cumulant is generally easy to compute and extract.

3.4 Dynamic Scaling and the Kibble-Zurek Mechanism

3.4.1 The Relaxation Time τ and the Critical Exponent z

Aside from static scaling, *dynamic critical phenomena* are of central importance to describe phase transitions. Dynamic scaling describes how much time fluctuations in systems take to equilibrate. That time is called the *relaxation time* τ_k and is typically specified for different length scales with the wavenumber k. The zero wavenumber relaxation time $\tau_0 = \tau$ quantifies relaxation on the largest length scales. Its scaling [42]

$$\tau = \tau_\xi \xi(\varepsilon)^z \tag{3.46}$$

defines a new *dynamic critical exponent* z, as well as a proportionality constant τ_ξ. Plugging in the known scaling of $\xi(\varepsilon)$ from Section 3.2 yields

$$\tau(\varepsilon) = \tau_\xi \xi(\varepsilon)^z = \tau_\xi \left(\xi^\pm |\varepsilon|^{-\nu}\right)^z := \tau_\varepsilon^\pm |\varepsilon|^{-\nu z} \ , \tag{3.47}$$

with $\tau_\varepsilon^\pm = \tau_\xi \xi^\pm$. As the correlation length diverges, so does the relaxation time. Interpreting ξ as a characteristic length at which system components are still influenced by each other provides an intuitive explanation for this divergence. The maximum speed for the propagation of interactions in the system is the respective speed of sound. Even the speed of sound needs an infinite amount of time to cover the diverging correlation distance. In practice, the propagation will be much slower than the speed of sound. This is the, in Section 3.2 mentioned, phenomenon of critical slowing down. As the reduced temperature approaches $\varepsilon \to 0$, it takes the system longer and longer to equilibrate. It then becomes a computational challenge to re-

lax large systems. However, since static scaling laws describe quantities in equilibrium and are only valid in the thermodynamic limit for $\varepsilon \to 0$, large, critical systems have to be considered. That dilemma is partially solved by the finite-size techniques of Section 3.3.

Analogous to the static phenomena, the dynamic scaling is universal as well. The static and dynamic universality classes are not independent, but the dynamic ones form subgroups of the static classes. Apart from the indicators described in Section 3.2, the conservation laws that are fulfilled by the system, as well as Poisson-bracket relations between the order parameter and the conserved quantities are decisive for the respective dynamic class. The important anisotropic Ising model is part of Model A as specified by Hohenberg and Halperin [42]. Its dynamic critical exponent can be expressed in terms of

$$z = 2 + c\eta \ , \tag{3.48}$$

with η as in Table 3.1 and c a constant to be determined.

3.4.2 Quenches and the Freeze-out of Domains

Systems like the Si(001) surface that exhibit order-disorder phase transitions usually have multiple possible orderings in the low temperature state. Boundaries between domains of different order, called domain walls, are stable topological defects. The *Kibble-Zurek mechanism* (KZM) describes the behavior of ξ after driving a system through its critical point [14, 15, 16]. It directly relates the correlation length to the static and dynamic critical exponents ν and z through a scaling law that has been verified in numerous experiments [43, 44, 45]. Therefore, it can be used to describe the final density of topological defects. The KZM shall be a central point of the upcoming investigations and is explained in the following.

We will solely consider linear quenches, specifically the cool down of a system linear in time t. The speed of cooling is characterized by the *quench timescale* τ_Q defined by

$$\varepsilon(t) = \frac{t}{\tau_Q} \ . \tag{3.49}$$

For slow quenches sufficiently far away from the critical point, the system will evolve adiabatically, i.e. thermodynamic quantities like ξ assume their equilibrium values. As the system approaches the phase transition at $t = 0$, the derivative

$$\frac{\partial}{\partial t}\xi(\varepsilon(t)) = -\nu\xi^{\pm}\frac{(\tau_Q)^{\nu}}{t^{-(\nu+1)}} \tag{3.50}$$

diverges and at some point will eventually outgrow the reaction capability of the system.

The actual correlation length will deviate from its equilibrium behavior as shown in Fig. 3.3. The timepoint $\hat{t}$ of divergence from the equilibrium behavior is called the *freeze-out*, since the current state of the system effectively becomes frozen in comparison with the equilibrium values. The KZM states that the freeze-out occurs roughly at

$$\tau(\hat{t}) = \hat{t} \ . \tag{3.51}$$

At this point, the system will not have time to equilibrate until the critical point is passed. The system quantities after the quench will be directly related to their equilibrium values at $\hat{t}$. Combining

$$\hat{t} = \varepsilon(\hat{t})\tau_Q \qquad \text{and} \qquad \hat{t} = \tau(\hat{t}) = \tau(\varepsilon(\hat{t})) = \tau_\varepsilon^{\pm}\left|\varepsilon(\hat{t})\right|^{-\nu z} \tag{3.52}$$

yields the reduced temperature at $\hat{t}$

$$\left|\varepsilon(\hat{t})\right| = \left(\frac{\tau_\varepsilon^{\pm}}{\tau_Q}\right)^{\frac{1}{1+\nu z}} \ . \tag{3.53}$$

For the scaling of the final correlation length this results in

$$\xi \propto \hat{\xi} := \xi(\varepsilon(\hat{t})) = \xi_0/|\varepsilon(\hat{t})|^{\nu} = \xi_0 \left| \frac{\tau_Q}{\tau_\varepsilon^{\pm}} \right|^{\frac{\nu}{1+\nu z}} , \tag{3.54}$$

so the frozen value of the ξ scales with the quench timescale like $\hat{\xi} \propto \tau_Q^{\frac{\nu}{1+\nu z}}$. The freeze-out of the correlation length implies domains of order with an extent proportional to $\hat{\xi}^2$. The domain walls separating ordered areas may influence different properties of the surface, including conductivity, an important quantity for the semiconductor industry. Knowledge of how the defect density on the surface behaves might help to prepare ideal silicon surfaces.

It is important to note that the KZM is a statistical phenomenon and will only be able to predict how the frozen correlation lengths behave on average for many quenches or very large systems. In general, the freeze-out correlation length $\hat{\xi}$ as well as the final correlation length will naturally differ from the predicted behavior, at least locally.

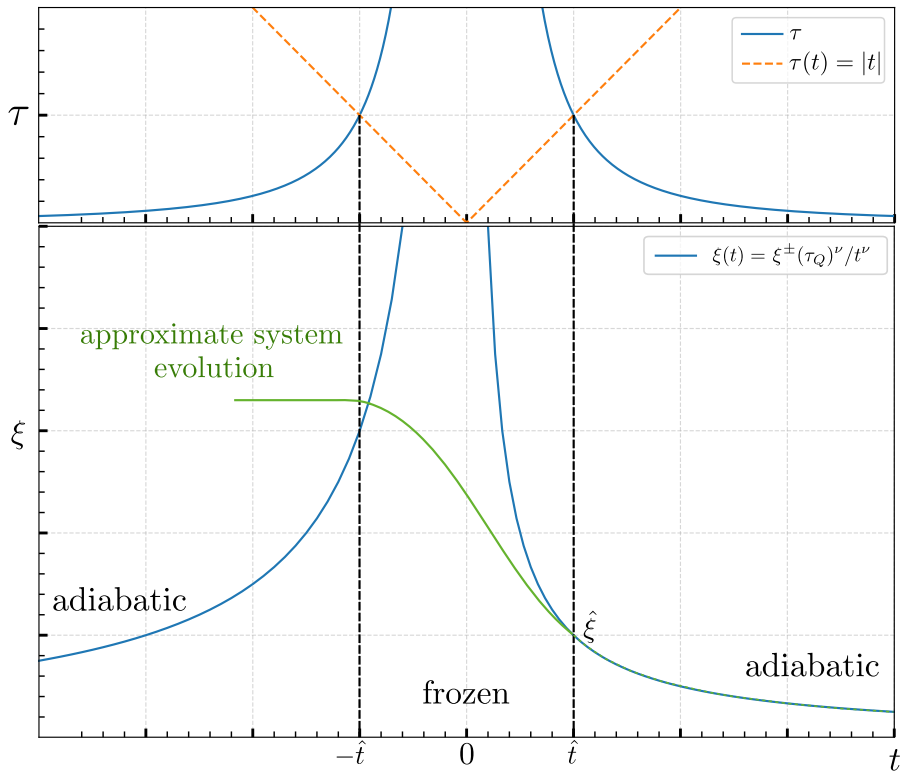

Figure 3.3: In the top plot the divergence of the relaxation time τ, i.e. the critical slowing down, is shown in blue versus the time t during a linear quench. The freeze-out of the current state occurs at roughly $\tau(\hat{t}) = \hat{t}$, visualized by the intersection with the dotted orange line. In the bottom plot, the divergence of the equilibrium ξ on the quench time is shown. Before $\hat{t}$, an initially equilibrated system evolves approximately adiabatic when quenched, following the blue line. After the freeze-out, the actual correlation diverges from the equilibrium behavior, shown by the sketched green line. Note that, in this parameterization, a cooling quench runs from $t > 0$ to $t < 0$. The frozen domain walls are topologically stable in time.

4 Simulating Dynamics

While most numerical studies of phase transitions rely on Monte Carlo techniques [46, 47, 48], this work, inspired by Laguana and Zurek [49], focuses on the use of *stochastic differential equations* (SDEs). Their mathematical basics and a derivation of a Langevin equation for our case will be outlined in the following.

4.1 Stochastic Differential and Langevin Equations

4.1.1 Stochastic Differential Equations

Stochastic differential equations are the stochastic generalizations of common differential equations like

$$y(t + \mathrm{d}t) = y(t) + A(y(t), t)\mathrm{d}t \ , \tag{4.1}$$

with an infinitesimal time interval $\mathrm{d}t$ and a given function $A(y(t), t)$. Equation (4.1) describes a *continuous, memoryless, deterministic* process. For every time point $t + \mathrm{d}t$, one can predict the value $y(t + \mathrm{d}t)$ knowing the values $y(t)$ and $\mathrm{d}t$. Stochastic differential equations describe continuous, memoryless, *stochastic* processes, also called continuous *Markov processes*. For each point in time, definite probabilities are assigned to all $y(t+\mathrm{d}t)$. Those properties impose strict limitations on a generalization of Eq. (4.1). It turns out that the generalization must be of the form

$$y(t + \mathrm{d}t) = y(t) + A(y(t), t)\mathrm{d}t + D^{1/2}\left(y(t), t\right) n(t)(\mathrm{d}t)^{1/2} \ . \tag{4.2}$$

The random variable $n(t)$ is the unit normal random variable $\mathcal{N}(0, 1)(t) \equiv n(t)$. $A(y(t), t)$ and $D(y(t), t)$ are called the *drift* and *diffusion* function. Equation (4.2) is called the standard form *Langevin equation* and represents an update formula for the continuous Markov process. It is the only way to construct a mathematically self-consistent formulation, meaning that performing one step $\mathrm{d}t$ or two steps $\alpha\mathrm{d}t$ and $(1 - \alpha)\mathrm{d}t$, $\alpha \in (0, 1)$, yield equivalent results. Proof is given in the appendix of [50].

The probability density $P(u)$, for $\mathcal{N}(\mu, \sigma^2)$ with mean μ and standard deviation σ to take on

the value u, is given by

$$P(u) = \frac{1}{\sqrt{2\pi\sigma^2}} e^{-\frac{(u-\mu)^2}{2\sigma^2}} \ . \tag{4.3}$$

Normal random variables satisfy

$$a + b\mathcal{N}(\mu, \sigma^2) = \mathcal{N}(a + b\mu, b^2\sigma^2) \ . \tag{4.4}$$

To obtain the widely used *differential* or *white noise* form of the Langevin equation out of Eq. (4.2), we define the *Gaussian white noise process* $\Gamma(t)$ by

$$\Gamma(t) := \lim_{\mathrm{d}t\to 0} \mathcal{N}(0, 1/\mathrm{d}t) = \lim_{\mathrm{d}t\to 0} \frac{n(t)}{(\mathrm{d}t)^{1/2}}. \tag{4.5}$$

Its expectation values $\langle \cdot \rangle$ satisfy

$$\langle \Gamma(t) \rangle = 0 \qquad \text{and} \qquad \langle \Gamma(t)\Gamma(t+t') \rangle = \delta(t') \ . \tag{4.6}$$

Rearranging Eq. (4.2) to

$$\frac{y(t+\mathrm{d}t) - y(t)}{\mathrm{d}t} = A(y(t), t) + D^{1/2}(y(t), t)\frac{n(t)}{(\mathrm{d}t)^{1/2}} \ , \tag{4.7}$$

and taking the limit $\mathrm{d}t \to 0$ yields the differential form

$$\frac{d}{\mathrm{d}t} y(t) = A(y(t), t) + D^{1/2}(y(t), t)\Gamma(t) \ . \tag{4.8}$$

Einstein showed that $A(y(t), t)$ and $D(y(t), t)$ are not independent if they are supposed to accurately describe a thermodynamic system [51]. Their relation will be subject of the next section.

4.1.2 Ornstein-Uhlenbeck Process and Brownian Motion

In the simulation of the silicon surface, the movement of each dimer is modeled in a double well potential (see subsection 4.4.3), whereby thermal fluctuations are taken into account. Hence, the movement of the dimer is modeled as Brownian motion.

Ornstein-Uhlenbeck process

The Ornstein-Uhlenbeck (OU) process is central to the mathematical description of Brownian motion with linear forces. It describes a continuous Markov process with drift and diffusion

functions of the form

$$A(y(t),t) = -\frac{1}{\zeta}y(t) \qquad \text{and} \qquad D(y(t),t) = c\ . \tag{4.9}$$

The constants ζ and c are the *relaxation time* and the *diffusion constant*. Plugging those functions into Eq. (4.2) gives

$$y(t+\mathrm{d}t) = y(t) - \frac{1}{\zeta}y(t)\mathrm{d}t + c^{1/2}n(t)(\mathrm{d}t)^{1/2}\ . \tag{4.10}$$

The quantity $y(\mathrm{d}t)$ is normally distributed since it is the sum of a constant $y(0)(1-\frac{\mathrm{d}t}{\zeta})$ and the normal random variable $n(\mathrm{d}t)$. Hence, $y(2dt)$ is normally distributed, being the linear combination of two statistically independent normal random variables $y(\mathrm{d}t)$ and $n(2dt)$. By induction, $y(t)$ is normally distributed for all times. Calculating mean and variance of $y(t)$ defines its distribution. Using the properties of Eq. (4.6), the differential equations for the first and second moment of y are calculated to

$$\langle y(t+\mathrm{d}t)\rangle = \langle y(t)\rangle - \frac{1}{\zeta}\langle y(t)\rangle\,\mathrm{d}t\ , \tag{4.11}$$

and

$$\left\langle y^2(t+\mathrm{d}t)\right\rangle = \left\langle y^2(t)\right\rangle - \frac{2}{\zeta}\left\langle y^2(t)\right\rangle\mathrm{d}t + c\ \mathrm{d}t\ . \tag{4.12}$$

Solving them with the initial condition $y(0) = y_0$ yields the mean

$$\langle y(t)\rangle = y_0 e^{-t/\zeta} \tag{4.13}$$

and the variance

$$\left\langle y^2(t)\right\rangle - \langle y(t)\rangle^2 = \frac{c\zeta}{2}\left(1-e^{-2t/\zeta)}\right) \tag{4.14}$$

of $y(t)$. This determines the distribution of $y(t)$ to be

$$y(t) = \mathcal{N}\left(y_0 e^{-t/\zeta}, \frac{c\zeta}{2}\left(1-e^{-2t/\zeta)}\right)\right) \overset{t\to\infty}{=} \mathcal{N}\left(0, \frac{c\zeta}{2}\right)\ . \tag{4.15}$$

Langevin's approach

Now consider, in analogy to the dimers, a particle with mass m and momentum p that is coupled to a reservoir of temperature T. Langevin hypothesized [52] that the interaction with the bath results in a dissipative drag force $-(\eta/m)p(t)$, proportional to a dampening constant η as well as a fluctuating force $F(t)$.

By Newton's second law, its equation of motion is given by

$$\frac{\mathrm{d}}{\mathrm{dt}}p(t) = -\frac{\eta}{m}p(t) + F(t). \tag{4.16}$$

This equation is identified with Eq. (4.10) at $y(t) \equiv p(t)$

$$\frac{\mathrm{d}}{\mathrm{dt}}p(t) = -\frac{1}{\zeta}p(t) + c^{1/2}\Gamma(t). \tag{4.17}$$

According to Maxwell-Boltzmann statistics, the directional velocity of the particles will be normally distributed around $\mu_v = 0$ with a standard deviation of $\sigma_v^2 = k_B T/m$. Using Eq. (4.6), for the momentum distribution

$$p(t \to \infty) = \mathcal{N}(0, mk_B T) \tag{4.18}$$

follows. Comparing Eqs. (4.15) and (4.18) shows that

$$\frac{c\zeta}{2} = mk_B T \ , \qquad \text{or, equivalently,} \qquad c = 2k_B T\eta \ . \tag{4.19}$$

Hence, the fluctuating force $F(t)$ can be restated as

$$F(t) = \sqrt{2k_B T\eta}\,\Gamma(t) \ , \tag{4.20}$$

confirming that drift and diffusion are not independent. That is a simple form of the powerful *fluctuation-dissipation theorem*. For a particle **in a potential** $V(x)$, one eventually obtains the equations of motions

$$\frac{\mathrm{d}}{\mathrm{dt}}x(t) = \frac{1}{m}p(t) \qquad \text{and} \tag{4.21}$$

$$\frac{\mathrm{d}}{\mathrm{dt}}p(t) = -\frac{\eta}{m}p(t) - \frac{\partial V(x)}{\partial x} + \sqrt{2k_B T\eta}\Gamma(t) \ . \tag{4.22}$$

Methods of numerical solution of the Langevin equation will be presented in Section 4.3. First, the applicability of the Langevin equation for the silicon surface will be verified.

4.2 Quantum Mechanical Considerations

4.2.1 Caldeira-Leggett Master Equation

The silicon surface is a complex system subject to quantum mechanical interactions between the surface atoms, as well as with the bulk. The bulk is much larger than the surface and acts as a thermal reservoir, engaging with the dimers through lattice excitations. Systems that are

coupled to an environment are subject of the theory of open quantum systems, which will be used to derive a set of coupled Langevin equations.

Consider the *Caldeira-Leggett model* [53] for a quantum mechanical particle of mass m, moving in a potential $V(\hat{x})$. We can write its **free Hamiltonian** $\hat{H}_S$ as

$$\hat{H}_S = \frac{1}{2m}\hat{p}^2 + V(\hat{x}) \ , \tag{4.23}$$

with the position and momentum operators $\hat{x}$ and $\hat{p}$. The reservoir, which is the silicon bulk, is modeled as a set of harmonic oscillators with frequencies ω_n. The bath Hamiltonian $\hat{H}_B$ can be formulated in terms of the bosonic annihilation and creation operators $\hat{b}_n^\dagger$ and $\hat{b}_n$, or in terms of the canonically conjugated position $\hat{x}_n$ and momentum $\hat{p}_n$ operators

$$\hat{H}_B = \sum_n \hbar\omega_n \left(\hat{b}_n^\dagger \hat{b}_n + \frac{1}{2}\right) = \sum_n \left(\frac{1}{2m_n}\hat{p}_n^2 + \frac{1}{2}m_n\omega_n^2\hat{x}_n^2\right) \ . \tag{4.24}$$

We assume that $\hat{x}$ is linearly coupled to the $\hat{x}_n$. Positivity of the global Hamiltonian can be ensured by introducing the interaction $\hat{H}_I$ as

$$\hat{H}_B + \hat{H}_I + \hat{H}_c = \sum_n \hbar\omega_n \left(\hat{b}_n^\dagger + \frac{\kappa_n}{\sqrt{2\hbar m_n\omega_n^3}}\,\hat{x}\right)\left(\hat{b}_n + \frac{\kappa_n}{\sqrt{2\hbar m_n\omega_n^3}}\,\hat{x}\right) \ , \tag{4.25}$$

with the coupling constants κ_n. Note that, strictly speaking, $\hat{b}^{(\dagger)}$ acts on the bath and $\hat{x}$ on the system Hilbert space. Unity operators on the respective Hilbert spaces that are required to add them up rigorously are omitted. The positivity of Hamiltonian (4.25) is guaranteed because of the square form of the terms. Positive Hamiltonians maintain a lower spectral bound, ensuring that unphysical runaway solutions are prohibited. The interaction Hamiltonian $\hat{H}_I$ is identified as

$$\hat{H}_I = -\hat{x}\otimes\sum_n \kappa_n\sqrt{\frac{\hbar}{2m_n\omega_n}}\left(\hat{b}_n + \hat{b}_n^\dagger\right) = -\hat{x}\otimes\sum_n \kappa_n\hat{x}_n =: -\hat{x}\otimes\hat{B} \ , \tag{4.26}$$

and the *counter-term* $\hat{H}_c$ is

$$\hat{H}_c = \hat{x}^2\sum_n \frac{\kappa_n^2}{2m_n\omega_n^2} \ . \tag{4.27}$$

In the following, the counter-term is absorbed into $\hat{H}_S$. The Hamiltonian of the combined system is given by

$$\hat{H}_{SB} = \hat{H}_S + \hat{H}_B + \hat{H}_I \ . \tag{4.28}$$

The composite system is visualized for the case of the Si(001) surface in Fig. 4.1. Since it is neither possible, nor required to solve the dynamics of the entire Hamiltonian, a probabilistic description will be developed. In quantum mechanics, this is achieved by modeling the system density matrix $\hat{\rho}_S$. In the following, operators in **interaction picture** are printed **bold** and $\hbar$ is set to one. The density matrix of the composite system in interaction picture with respect to $\hat{H}_S + \hat{H}_B$ is given by

$$\hat{\boldsymbol{\rho}}_{SB} := e^{\mathrm{i}\left(\hat{H}_S+\hat{H}_B\right)t}\hat{\rho}_{SB}e^{-\mathrm{i}\left(\hat{H}_S+\hat{H}_B\right)t} \ . \tag{4.29}$$

The time evolution of $\hat{\boldsymbol{\rho}}_{SB}$ is

$$\frac{\partial}{\partial t}\hat{\boldsymbol{\rho}}_{SB}(t) = -\mathrm{i}\left[\hat{\boldsymbol{H}}_I(t), \hat{\boldsymbol{\rho}}_{SB}(t)\right] \ . \tag{4.30}$$

To derive an equation for $\hat{\boldsymbol{\rho}}_S$ the reservoir degrees of freedom are traced out

$$\begin{aligned}\frac{\partial}{\partial t}\hat{\boldsymbol{\rho}}_S(t) &= \mathrm{tr}_B\left\{\frac{\partial}{\partial t}\hat{\boldsymbol{\rho}}_{SB}(t)\right\} = -\mathrm{i}\ \mathrm{tr}_B\left\{\left[\hat{\boldsymbol{H}}_I(t), \hat{\boldsymbol{\rho}}_{SB}(t)\right]\right\} \\ &= -\mathrm{i}\ \mathrm{tr}_B\left\{\left[\hat{\boldsymbol{H}}_I(t), \hat{\rho}_{SB}(0)\right]\right\} - \int_0^t \mathrm{d}t'\ \mathrm{tr}_B\left\{\left[\hat{\boldsymbol{H}}_I(t), \left[\hat{\boldsymbol{H}}_I(t'), \hat{\boldsymbol{\rho}}_{SB}(t')\right]\right]\right\} \\ &= -\int_0^t \mathrm{d}t'\ \mathrm{tr}_B\left\{\left[\hat{\boldsymbol{H}}_I(t), \left[\hat{\boldsymbol{H}}_I(t'), \hat{\boldsymbol{\rho}}_S(t')\otimes\overline{\rho}_B\right]\right]\right\} \ .\end{aligned} \tag{4.31}$$

The second line in Eq. (4.31) is obtained by integrating Eq. (4.30) and solving for $\hat{\rho}_{SB}(0)$. Bath and system are assumed to be in a product state at the initial time $\hat{\rho}_{SB}(0) = \hat{\rho_S}(0)\otimes\overline{\rho}_B$. Therefore, the trace

$$\mathrm{tr}_B\left\{\left[\hat{\boldsymbol{H}}_I(t), \hat{\boldsymbol{\rho}}_{SB}(0)\right]\right\} = 0 \tag{4.32}$$

vanishes. The *Born approximation* assumes that the reservoir density matrix is stationary. In this case, $\hat{\boldsymbol{\rho}}_{SB}(t)$ decomposes to $\hat{\boldsymbol{\rho}}_{SB}(t) = \hat{\boldsymbol{\rho}}_S(t)\otimes\overline{\rho}_B$ for all times and the third line is obtained. The integrand in Eq. (4.31) typically decays rather fast (see Section A.1). Hence, the *Markov approximation* [54] is applicable. That involves the replacement $\hat{\boldsymbol{\rho}}_S(t') \to \hat{\boldsymbol{\rho}}_S(t)$, as well as sending the upper limit of the integral to infinity. Substituting $\tau = t - t'$ yields the *Redfield-II* master equation

$$\frac{\partial}{\partial t}\hat{\boldsymbol{\rho}}_S(t) = -\int_0^\infty \mathrm{d}\tau\ \mathrm{tr}_B\left\{\left[\hat{\boldsymbol{H}}_I(t), \left[\hat{\boldsymbol{H}}_I(t-\tau), \hat{\boldsymbol{\rho}}_S(t)\otimes\overline{\rho}_B\right]\right]\right\} \ . \tag{4.33}$$

Transforming Eq. (4.33) back to the Schrödinger picture gives

$$\frac{\partial}{\partial t}\hat{\rho}_S(t) = -\mathrm{i}\ \left[\hat{H}_S, \rho_S(t)\right] - \int_0^\infty \mathrm{d}\tau\ \mathrm{tr}_B\left\{\left[\hat{H}_I, \left[\hat{\boldsymbol{H}}_I(-\tau), \hat{\rho}_S(t)\otimes\overline{\rho}_B\right]\right]\right\} \ . \tag{4.34}$$

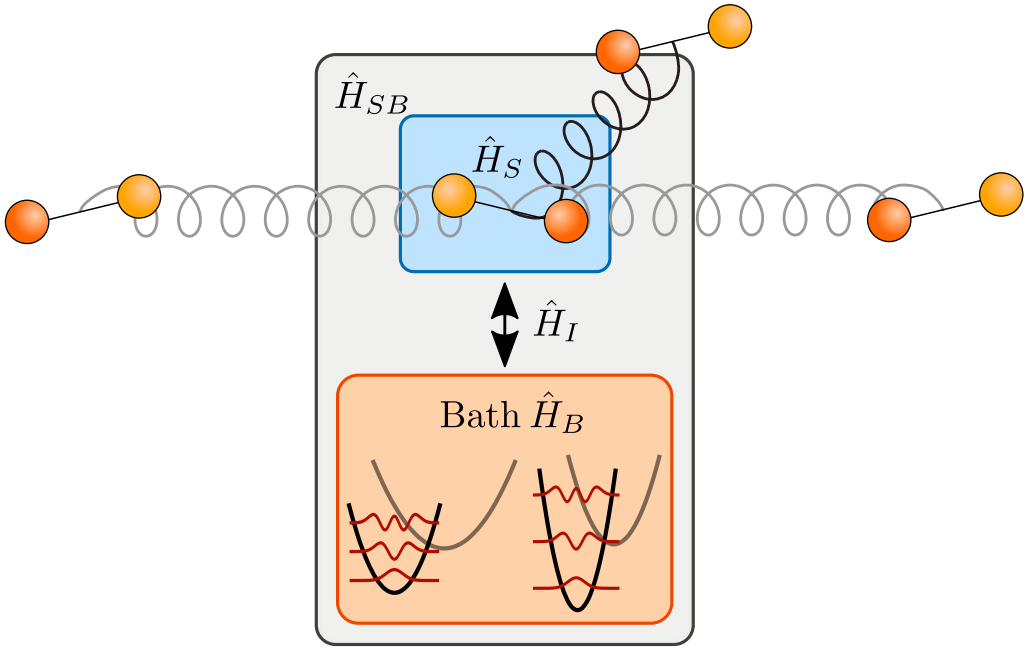

Figure 4.1: In the theory of open quantum systems, a system that is thermally coupled to an environment is modeled by a composite Hamiltonian $\hat{H}_{SB} = \hat{H}_S + \hat{H}_B + \hat{H}_I$. $\hat{H}_S$ denotes the system Hamiltonian describing the potential acting on the dimer. The reservoir is modeled as a set of harmonic oscillators captured in $\hat{H}_B$. The interaction between a dimer and the bath are contained in $\hat{H}_I$. We approximate that every dimer is coupled to a separate bath.

The integral in the second term of Eq. (4.34) can be rearranged to

$$\int_0^\infty \mathrm{d}\tau \left(\frac{\mathrm{i}}{2} D(\tau) \Big[\hat{x}, \{ \hat{\boldsymbol{x}}(-\tau), \hat{\rho}_S(t) \} \Big] - \frac{1}{2} D_1(\tau) \Big[\hat{x}, \big[\hat{\boldsymbol{x}}(-\tau), \hat{\rho}_S(t) \big] \Big] \right) , \tag{4.35}$$

with the noise kernel $D_1(\tau)$ and dissipation kernel $D(\tau)$ defined as in Section A.1. The noise and dissipation kernels disappear on the timescale of the relaxation τ_B of the reservoir. When performing the Markov approximation, it is assumed that this timescale is much shorter than the relaxation time of the system τ_S. This is used again by approximating $\hat{\boldsymbol{x}}(-\tau)$ by its free dynamics

$$\hat{\boldsymbol{x}}(-\tau) = \hat{x} - \hat{p}\tau \ . \tag{4.36}$$

For large $\tau > \tau_B$ the integrand decays quickly and in the case $\tau < \tau_B < \tau_S$ Eq. (4.36) is valid in good approximation. Plugging the free dynamics into Eq. (4.35) allows for the evaluation of the integrals (see Section A.1). This eventually yields the *Caldeira-Leggett master equation*

$$\frac{\mathrm{d}}{\mathrm{d}t}\rho_S(t) = \underbrace{-\mathrm{i}\Big[\hat{H}_S, \rho_S(t)\Big]}_{\text{free dynamics}} \underbrace{- \mathrm{i}\eta \Big[\hat{x}, \{\hat{p}, \rho_S(t)\}\Big]}_{\text{dissipative term}} \underbrace{- 2\eta k_B T \Big[\hat{x}, \big[\hat{x}, \rho_S(t)\big]\Big]}_{\text{thermal fluctuations}} \ . \tag{4.37}$$

The damping constant η enters the calculation through the parametrization of the spectral density function of the reservoir. The first term in the Caldeira-Leggett master equation describes the free dynamics of the system and resembles the form of the *von-Neumann equation*. The second term is the dissipative part proportional to the damping constant η. The thermal fluctuations of the reservoir are captured in the third term proportional to the temperature T. The state of the reservoir $\overline{\rho}_B$ follows the *Bose-Einstein distribution* and determines T.

Thermalization

Investigating the position space representation of Eq. (4.37) shows that its stationary solution is found to be the position space density matrix

$$\hat{\rho}_S(x,x') = \frac{1}{Z} e^{-\beta V((x+x')/2)} e^{-\frac{1}{2\beta}(x-x')^2} \tag{4.38}$$

with the normalization

$$Z = \int_{-\infty}^{\infty} \mathrm{d}x\, e^{-\beta V(x)} \ . \tag{4.39}$$

The inverse temperature is again denoted by $\beta = 1/k_B T$. The diagonal terms of Eq. (4.38) are identified with the canonical distribution of statistical mechanics. The off-diagonals decay exponentially and vanish for large temperatures. Thus, systems described by Eq. (4.37) thermalize in the sense that their steady state solution is analogue to the canonical distribution.

4.2.2 Equations of Motion

From Eq. (4.37) one can derive equations of motion for arbitrary observables via

$$\frac{\mathrm{d}}{\mathrm{d}t}\left\langle \hat{A} \right\rangle = \mathrm{tr}\left\{ \hat{A} \frac{\mathrm{d}}{\mathrm{d}t} \hat{\rho}_S(t) \right\} \ , \tag{4.40}$$

using the invariance of the trace under cyclic permutations. Comparing the results of Eq. (4.40) for $\hat{x}, \hat{p}$ and $\hat{p}^2$ to the equations of Brownian motion of subsection 4.1.2

$$\begin{aligned}
\frac{\mathrm{d}}{\mathrm{d}t}\langle \hat{x} \rangle &= \frac{1}{m}\langle \hat{p} \rangle \ , \\
\frac{\mathrm{d}}{\mathrm{d}t}\langle \hat{p} \rangle &= -\left\langle \frac{\partial V(\hat{x})}{\partial \hat{x}} \right\rangle - \eta \langle \hat{p} \rangle \ , \\
\frac{\mathrm{d}}{\mathrm{d}t}\langle \hat{p}^2 \rangle &= -\left\langle \hat{p}\frac{\partial V(\hat{x})}{\partial \hat{x}} + \frac{\partial V(\hat{x})}{\partial \hat{x}}\hat{p} \right\rangle \\
&\quad - 2\eta \langle \hat{p}^2 \rangle + 2\eta k_B T \ ,
\end{aligned}
\qquad
\begin{aligned}
\frac{\mathrm{d}}{\mathrm{d}t}\langle x(t) \rangle &= \frac{1}{m}\langle p(t) \rangle \ , \\
\frac{\mathrm{d}}{\mathrm{d}t}\langle p(t) \rangle &= -\left\langle \frac{\partial V(x)}{\partial x} \right\rangle - \eta \langle p(t) \rangle \ , \\
\frac{\mathrm{d}}{\mathrm{d}t}\langle p^2(t) \rangle &= -\left\langle 2p(t)\frac{\partial V(x)}{\partial x} \right\rangle \\
&\quad - 2\eta \langle p^2(t) \rangle + 2\eta k_B T \ ,
\end{aligned}$$

shows that the two equation sets share the same structure. The last term in the equations for

$\langle \hat{p}^2 \rangle$ is especially interesting. This is the diffusion constant in the case of Brownian motion and it matches the quantum mechanical term. Hence, it is possible to derive the diffusion constant from microscopic considerations. We conclude that the classical equations of motion Eqs. (4.21) and (4.22) are the classical correspondence to the equations of $\langle \hat{x} \rangle$ and $\langle \hat{p} \rangle$. In the following, the classical equations of motion are used to describe the silicon surface. Since the silicon dimers interact, the potential $V(x) = V(x, x_i)$ is a function of the coordinates x_i of the other dimers, leading to a *coupling* between the differential equations. Additionally, $V(x, x_i)$ is *nonlinear* in x, eventually yielding a coupled set of nonlinear stochastic differential equations. An analytic solution is impossible and, therefore, we turn to numerical solutions in the next section.

4.3 Numerical Methods and Molecular Dynamics

The update-form Eq. (4.2) of the Langevin equation is very useful for its numerical solution. A simple method of solution is the straight implementation of Eq. (4.2), which is called the *Euler-Maruyama method* [55]. Practically, a system of first-order stochastic differential equations

$$x(t + \mathrm{d}t) = x(t) + \frac{1}{m} p(t) \mathrm{d}t \ , \tag{4.41}$$

$$p(t + \mathrm{d}t) = p(t) - \frac{\eta}{m} p(t) \mathrm{d}t - \frac{\partial V(x(t))}{\partial x} \mathrm{d}t + \sqrt{2 k_B T \eta}\ n(t) \sqrt{\mathrm{d}t} \ , \tag{4.42}$$

is solved. The Euler-Maruyama method is straightforward to implement and computationally inexpensive, but shows discretization artifacts even for small step sizes $\mathrm{d}t$. The integration of the equations of motion usually takes much less time than the evaluation of $V(x(t))$ [56]. Hence, many efforts have been made to improve the weak convergence, i.e. the convergence of expectation values rather than accurate approximate of sample paths [55], of integration schemes.

The topic of simulating microscopical systems by numerically solving Newton's equations of motion is called *molecular dynamics*. Molecular dynamics is widely used in biophysics, chemical physics but also material sciences. When Langevin equations are employed to simulate thermally open systems, one also talks about *Langevin dynamics*. Larini et al. [57] compare some of the common numerical integration schemes for Langevin equations. They show that in general, the popular Brunger-Brooks-Karplus (BBK) [58] scheme is a robust method with good accuracy and numerical efficiency.

It integrates in three steps [59], half a kick

$$p\left(t+\tfrac{1}{2}\mathrm{d}t\right) = \left(1-\tfrac{1}{2}\eta\mathrm{d}t\right)p(t) - \tfrac{1}{2}\mathrm{d}t\tfrac{\partial V(x(t))}{\partial x} + \tfrac{1}{2}\sqrt{2\eta k_B T}n(t)\sqrt{\mathrm{d}t}\ , \tag{4.43}$$

drift

$$x(t+\mathrm{d}t) = x(t) + p\left(t+\tfrac{1}{2}\mathrm{d}t\right)\mathrm{d}t\ , \tag{4.44}$$

and half a kick

$$p\left(t\right) = \left(1+\tfrac{\mathrm{d}t}{2}\eta\right)^{-1}\left(p\left(t+\tfrac{\mathrm{d}t}{2}\right) - \tfrac{1}{2}\mathrm{d}t\tfrac{\partial V(x(t+\mathrm{d}t))}{\partial x} + \tfrac{1}{2}\sqrt{2\eta k_B T}n(t+\mathrm{d}t)\sqrt{\mathrm{d}t}\right)\ . \tag{4.45}$$

Compared to higher-order schemes, like the fourth-order Hamiltonian Runge-Kutta scheme [60], that require multiple potential evaluations, the BBK method is faster with limited loss of accuracy [57]. The BBK integration step is slightly slower than the one of Euler-Maruyama, but it makes up through its much greater stability regarding larger step sizes. This ultimately results in significantly faster simulation speeds. The stability of the schemes is briefly compared in Section A.2.

The theoretical foundation for the simulation of the Si(001) surface using Langevin equations is now established. The following section will deal with the modeling of the several times mentioned potential.

4.4 The Model

4.4.1 The Ising Model

Since the Ising model has discrete states, it is not suitable for continuous modeling with equations of motion. However, the Ising model is well known and has been used several times [28, 8, 29, 11] to study the Si(001) surface and can serve as a limiting case. Brand et al. [12] found good agreement between the Si(001) phase transition and the Ising critical exponents. Their results are relevant for the following investigations and therefore the Ising model is shortly discussed below.

The two dimensional Ising model describes spins $\sigma_{i,j} = \pm 1$ on a lattice. Consider the anisotropic case without external field. Its nearest-neighbor Hamiltonian is given by

$$H = -\sum_{i,j}\left(J_{\parallel}\sigma_{i,j}\sigma_{i,j+1} + J_{\perp}\sigma_{i,j}\sigma_{i+1,j}\right)\ , \tag{4.46}$$

with J_δ, $\delta \in \{\parallel, \perp\}$, being the effective nearest-neighbor coupling strengths for parallel and perpendicular interaction. The two dimensional anisotropic Ising model is analytically solvable [61] and exhibits a continuous phase transition at

$$\sinh\left(\frac{2|J_\parallel|}{k_B T_c}\right)\sinh\left(\frac{2|J_\perp|}{k_B T_c}\right) = 1. \tag{4.47}$$

The equilibrium correlation lengths for $T > T_c$ can be determined from the couplings [62] by

$$\frac{\xi_\delta(T)}{a_\delta} = \left(\ln\left[\coth\left(\frac{|J_\delta|}{k_B T}\right)\right] - \frac{2|J_{\overline{\delta}}|}{k_B T}\right)^{-1}, \tag{4.48}$$

with a_δ being the lattice spacing in δ direction and $\overline{\delta}$ marking the direction perpendicular to δ.

To describe the silicon surface with the Ising model, the equilibrium positions of the silicon dimers in Fig. 2.2 (b) are mapped to the Ising spin values $\sigma_{i,j} = \pm 1$. In theoretical works, *density functional theory* (DFT) calculations are often employed to calculate configuration energies. Equation (4.46) can then be used to fit effective J_δ to the DFT results. In experiments, the correlation lengths ξ_δ can be measured and used to extract J_δ through Eq. (4.48). Calculating quantitative values for J_δ can reveal important information about the nature of the microscopic interactions between the dimers, especially if Eq. (4.46) is extended to next-nearest neighbor couplings. Additionally, theoretical results of the Ising model can be used to further analyze the surface. For example, Eq. (4.47) may be used to estimate the transition temperature. Eventually, a simple theoretical model of the Si(001) system is obtained, which also may be used in computer simulations.

The Ising model gives name to its universality class. It is characterized by a continuous phase transition with a scalar order parameter and $\mathbb{Z}_2$ symmetry. The static critical exponents of the Ising universality class can be calculated analytically [67]. For ν the exact value

$$\nu = 1 \tag{4.49}$$

is obtained. As noted in Section 3.4, the anisotropic Ising model is part of Model A of critical dynamics [42]. The constant c of Eq. (3.48) has been estimated by numerous methods. Some recent results for z are shown in Table 4.1.

Table 4.1: Recent results for the dynamic critical exponent z are summarized. The estimates are obtained by Monte-Carlo methods (MC) [63], renormalization group calculations (RG) [64, 65] and high-temperature expansion (HT) [66].

Source	Method	Result
[63]	MC	2.167
[64]	RG	2.14 ± 0.02
[65]	RG	2.183 ± 0.005
[66]	HT	2.15
z_{Ising}	Average	2.16

4.4.2 The Classical XY Model

The classical XY model and the Ising model can be viewed as two special cases of the Potts model [68]. It generalizes the Ising model to allow q, instead of two, states. The states are uniformly distributed on a circle as shown in Fig. 4.3 (a). In the limit $q \to \infty$ the XY model is obtained. It allows continuous states on the unit circle and is thus suitable to be described by Langevin equations.

The two dimensional XY Hamiltonian with nearest-neighbor interactions is given by

$$\begin{aligned} H &= -\sum_{i,j} \left(J_{\parallel} \vec{s}_{i,j} \vec{s}_{i,j+1} + J_{\perp} \vec{s}_{i,j} \vec{s}_{i+1,j} \right) \\ &= -\sum_{i,j} \left(J_{\parallel} \cos\left(\vartheta_{i,j} - \vartheta_{i,j+1}\right) + J_{\perp} \cos\left(\vartheta_{i,j} - \vartheta_{i+1,j}\right) \right) \ , \end{aligned} \tag{4.50}$$

with unit-length vectors

$$\vec{s}_{i,j} = \begin{pmatrix} \cos\vartheta_{i,j} \\ \sin\vartheta_{i,j} \end{pmatrix} \ , \tag{4.51}$$

characterizing the state of the lattice site. These rotors are defined by a continuous angle ϑ on the interval $[0, 2\pi)$. Although the exact solution of the two dimensional XY model is intractable, Mattis [69] used a transfer matrix approach to approximate an analogue to Eq. (4.47). He arrived at

$$\frac{2k_B T_c}{|J_{\parallel}|} \ln\left(\frac{2k_B T_c}{|J_{\perp}|}\right) = 1 \ , \tag{4.52}$$

with $J_{\parallel} \geq J_{\perp}$. The relation between the coupling constants and the equilibrium correlation lengths is not known at the moment. For low temperatures, the XY model undergoes a transition to a quasi ordered phase of bound vortex-antivortex pairs. A comparison between the phase diagram resulting from this equation and Eq. (4.47) is shown in Fig. 4.2.

The two dimensional XY model does not exhibit a phase transition in the conventional sense. The *Mermin-Wagner theorem* [70] prohibits the breaking of its continuous O(2) symmetry through short-range interactions. Instead, the system shows the *Kosterlitz-Thouless transition* (KT transition) [71, 72]. The usual power laws are not applicable to this transition because the correlation length diverges exponentially at the critical point. Hence, the two dimensional XY model does not belong to any universality class.

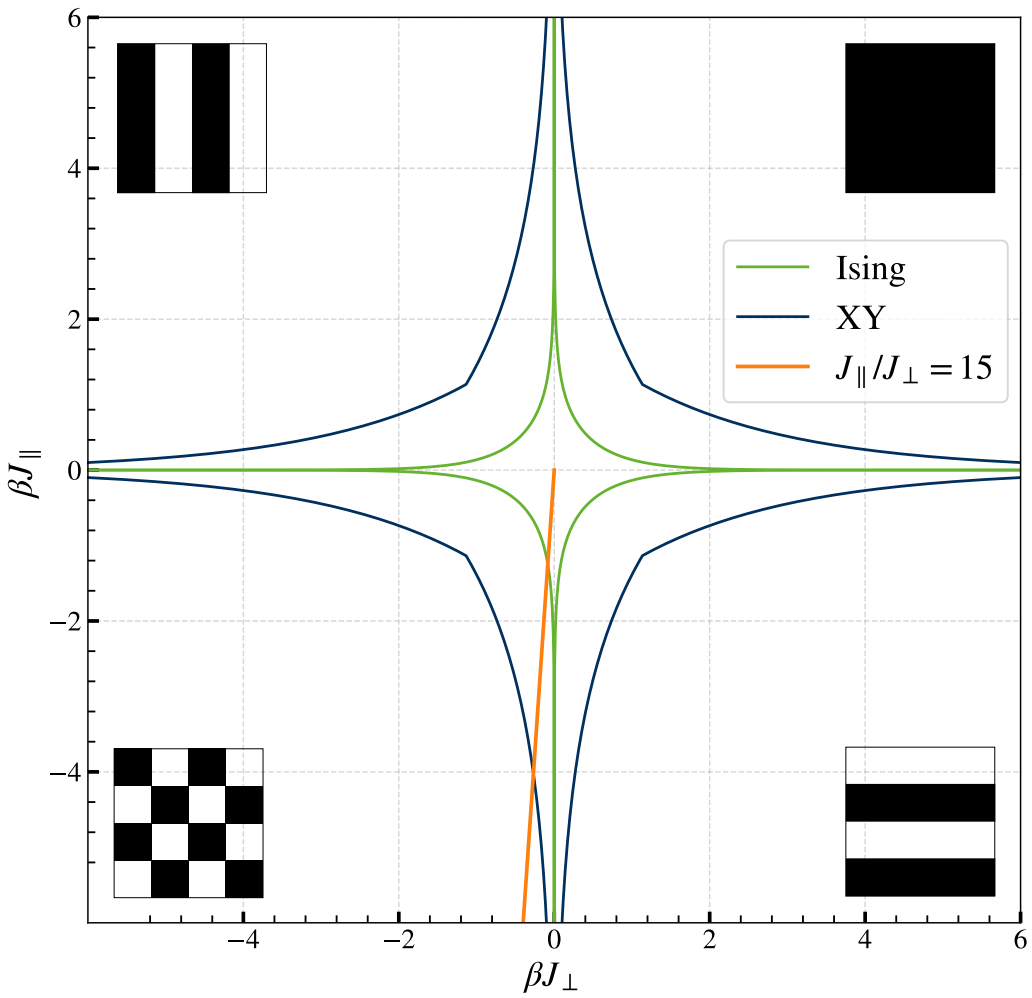

Figure 4.2: The phase diagram of the Ising model and the isotropic XY model is shown in the $\beta J_\parallel - \beta J_\perp$−plane. The green and blue lines determine the phase boundary between the unordered and ordered state of the Ising and the XY model respectively. The unordered high-temperature phase is found in the center for $\beta J_\delta \to 0$. Depictions of the Ising model ordering are shown in the corners of the diagram. They visualize whether neighbors are correlated or anti-correlated. The ordered state in the XY case is a quasi ordered phase of bound vortex-antivortex pairs with a somewhat different appearance. However, the neighbor correlations are the same as in the Ising case. The area of the high-temperature phase of the XY model is larger than in the Ising model, indicating that greater coupling constants are needed to introduce ordering. The orange line shows an equipotential line with $J_\parallel/J_\perp = 15$ for both coupling constants smaller than zero. A system that is quenched according as described in subsection 3.4.2 for a fixed $J_\parallel/J_\perp$ follows this line from the center outwards.

We can add a p-fold symmetry-breaking field of strength h to the XY Hamiltonian

$$H = -\sum_{i,j} \left(J_{\parallel} \cos\left(\vartheta_{i,j} - \vartheta_{i,j+1}\right) + J_{\perp} \cos\left(\vartheta_{i,j} - \vartheta_{i+1,j}\right)\right) + h \sum_{i,j} \cos(p\vartheta_{i,j}) \ , \tag{4.53}$$

explicitly breaking the O(2) symmetry. Such fields may very well be experimentally realized by crystalline anisotropies. In the following, we will differentiate between the Hamiltonians (4.50) and (4.53) by calling the former *isotropic* XY model and the latter *symmetry-broken* or *anisotropic* XY model. Note that, in this context, (an-)isotropic references the plane of the spin rotor and it is not to be confused with the lattice anisotropy of the interactions.

The Migdal lattice recursion scheme [73] implies that for $T \to 0$, the field h is a relevant variable in the sense of Section 3.1. The perturbations caused by h will grow as T shrinks, eventually forcing the system into a state of broken symmetry in which one of the directions $\vartheta = 2\pi n/p, n \in [0, p-1]$ is preferred. Hence, any h will lead to deviations in critical behavior from the KT transition. José and Kadanoff [74] found that this symmetry-broken XY model exhibits a continuous phase transition with the critical exponents of a p-state Potts model. This results in Ising critical behavior, which is in good agreement with the critical behavior of Si(001) [12], in the case of $p = 2$. Hence, the two dimensional XY model with twofold symmetry-breaking field is well suited to explore the dynamics of the Si(001) surface.

4.4.3 Adaptation to the Si(001) Surface

In the following, the XY model will be adapted to optimally resemble the silicon surface.

Like done with the Ising model, the aim is to map the position of the dimer to a model state. The natural choice is to identify the dimer buckling angle with the rotor angle ϑ of the XY model. Since the silicon atoms are indistinguishable, a rotation by π translates into the same state. Hence, only $\vartheta \in [0, \pi)$ define unique states, restricting the state space of the XY model. The resulting half circle is shown in the rightmost picture of Fig. 4.3 (a). For computational reasons, ϑ will be shifted by $-\frac{\pi}{2}$, eventually yielding $\vartheta \in \left[-\frac{\pi}{2}, \frac{\pi}{2}\right)$. The restriction is achieved by adding a factor $m = 2$ into the interaction terms

$$J_{\delta} \cos\left(m\Delta\vartheta_{i,j}\right) \ . \tag{4.54}$$

The equilibrium position of the dimers is majorly influenced by the location of the minima of the symmetry-breaking field. The experimental system shows two stable buckling angles of about $\pm 20°$. Therefore, the symmetry-breaking field will be constructed to have two minima

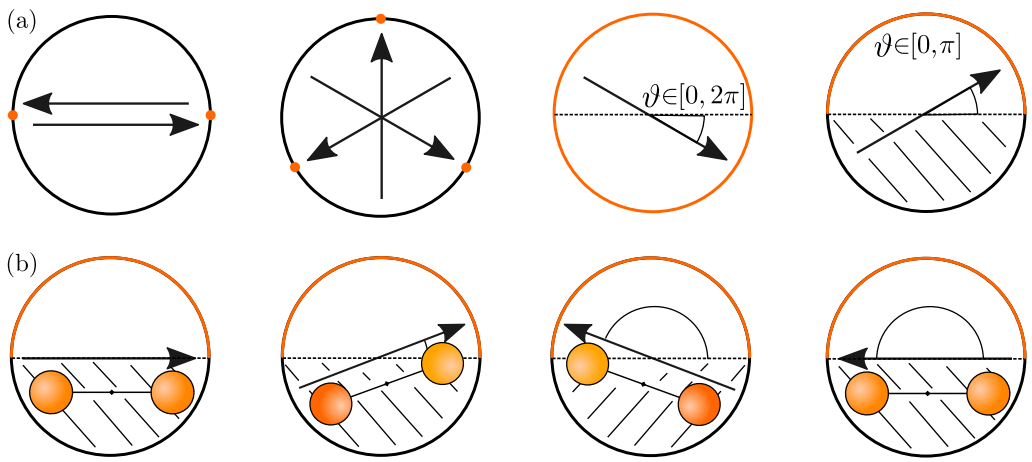

Figure 4.3: Unit circles are shown as visualizations of the state space. The orange parts are the allowed states. The states are depicted as arrows inside the unit circle. Figure **(a)** shows the q-state Potts model. From left to right: The two-state Potts model, or the Ising model, allows only two points on the unit circle. The three-state Potts model allows three different spin directions, visualized by the arrows. In the limit $q \to \infty$ the XY model is obtained. The state is characterized by a continuous angle ϑ. The rightmost circle visualizes the adaptation of the XY model to the silicon surface. Here, only half the circle is allowed. In panel **(b)** the buckling angles of the silicon dimers are mapped to the rotors of the XY model. Since the silicon atoms are indistinguishable, a rotation by π maps to the same state. Hence, the state space is only half the unit circle. Note that the left and right vectors are the same state and strictly speaking one of them can be excluded by defining $\vartheta \in [0, \pi)$.

on the interval $\left[-\frac{\pi}{2}, \frac{\pi}{2}\right)$ at the desired angles. The minima satisfy

$$\cos\left(p\vartheta^{\pm}\right) = -1 \ , \tag{4.55}$$

implying that roughly $p \approx 2.5$. The final resting position of the dimer is shifted by the repulsive interaction of the dimers. This is covered in Section A.5. The movement of the dimers can be approximated to take place in a double well potential [22]. This is realized by the symmetry-breaking field shown in Fig. 4.4. The question arises if the system still belongs to the Ising universality class if p is a rational number and the allowed states are restricted. This will be subject of subsection 5.3.3.

A suitable order parameter for this model is

$$M_L = \frac{1}{L^2} \sum_{i,j} m(\vartheta_{i,j}) \qquad \text{with} \qquad m(\vartheta) = \sin\left(\tfrac{p}{2}\vartheta\right) \ , \tag{4.56}$$

as the $m(\vartheta)$ have maxima at ϑ^+ and minima at ϑ^-, satisfying $m(\vartheta^+) = -m(\vartheta^-)$.

The XY model's natural conjugated coordinate is the angle ϑ, so, Eqs. (4.21) and (4.22) have to be adapted to rotary motion. The velocity is replaced by the angular velocity ω in this case.

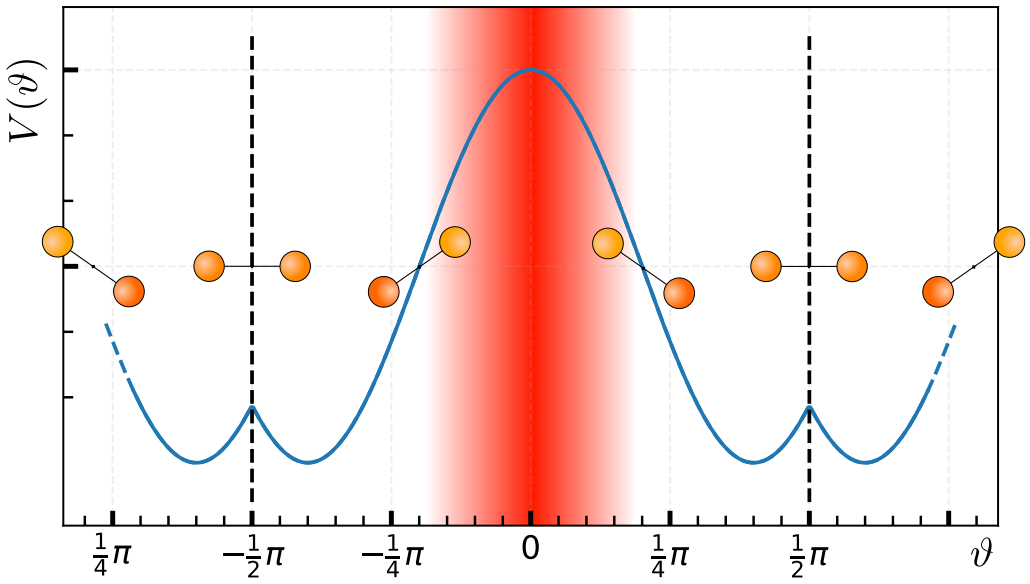

Figure 4.4: The symmetry-breaking field h is shown in blue on the dimer angle. The dimer states are defined on $\vartheta \in [-\frac{\pi}{2}, \frac{\pi}{2})$, therefore h repeats after a period of π. The locations of the potential minima are chosen to correspond to the according positions of the experimental dimers. The red area around $\vartheta = 0$, corresponding to vertical dimers, is strongly suppressed for large h. The dynamics take place in the double well potential shown on the left and right side of the plot. Note that the two double well potentials are actually located at the same position since the state space is periodic. Some dimer states are depicted at their according angle.

Eq. (4.53) yields the force

$$\begin{aligned}\frac{\partial V(\{\vartheta\})}{\partial \vartheta_{i,j}} = \quad & J_{\parallel} m \Big(\sin\left(\vartheta_{i,j} - \vartheta_{i+1,j}\right) + \sin\left(\vartheta_{i,j} - \vartheta_{i-1,j}\right) \Big) \\ & + J_{\perp} m \Big(\sin\left(\vartheta_{i,j} - \vartheta_{i,j+1}\right) + \sin\left(\vartheta_{i,j} - \vartheta_{i,j-1}\right) \Big) \\ & + hp \sin(p\vartheta_i) \ .\end{aligned} \tag{4.57}$$

Eventually, the Langevin equations become

$$\frac{\mathrm{d}}{\mathrm{d}t}\vartheta_{i,j}(t) = \omega_{i,j}(t) \ , \tag{4.58}$$

$$\frac{\mathrm{d}}{\mathrm{d}t}\omega_{i,j}(t) = -\frac{\eta}{I}\omega_{i,j}(t) - \frac{1}{I}\frac{\partial V(\{\vartheta\})}{\partial \vartheta_{i,j}} + \sqrt{\frac{2k_B T \eta}{I^2}}\Gamma(t) \ , \tag{4.59}$$

with the moment of inertia I replacing the mass m. The implementation of the integration of this coupled set of stochastic differential equations will be the subject of the next section.

5 Implementation and Results

To reduce finite-size corrections, it is preferable to consider systems as large as possible. Combined with the critical slowing down described in Section 3.4, the task at hand requires significant computational effort. Moreover, the stochastic nature of the system demands the simulation of many realizations to calculate ensemble averages. Additionally, minimizing discretization errors and ensuring convergence when integrating Eq. (4.59) forces the choice of a small step size $\mathrm{d}t$. This makes an efficient and fast implementation a crucial part of our investigations.

5.1 GPU Programming

Apart from the difficulties just described, there is an advantage that can be leveraged. The Langevin equations for the different lattice sites may be coupled, but the integration step to $t + \mathrm{d}t$ only depends on the $\vartheta_{i,j}(t)$ of the previous step. Hence, the integrations can be performed simultaneously in real time. That allows parallelization of the computation, making the problem ideal for a graphical processing unit (GPU) implementation.

The main difference between a conventional single core implementation on a central processing unit (CPU) and one on GPU is the number of processing cores involved. One core can execute one instruction at a time. While CPUs only have few (~ 10) powerful processing cores, GPUs are made having up to 10^4 cores. The CPU traditionally solves problems in a sequential matter, doing calculation after calculation. That makes them suitable for use in cases in which one step directly depends on the previous one. In contrast, the GPU capable of performing many independent calculations real time simultaneously on its different cores. In situations in which this is applicable, GPU implementations yield a significant speedup of up to a factor of 100 [75]. A concept of the different solution approaches is shown in Fig. 5.1.

The simulation is implemented in CUDA C++ [76] using Thrust [77] as high level interface. Inspired by Ahnert et al.'s work [78], the architecture has been extended to accommodate stochastic differential equations. The random numbers are generated using CUDA's built in library cuRAND. Refer to Table A.1 for details on the hardware and software employed.

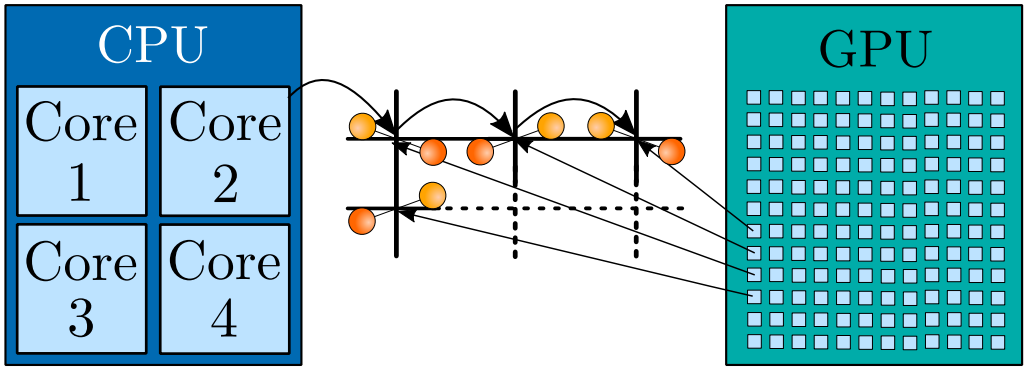

Figure 5.1: The conceptual structures of CPUs and GPUs are shown. A CPU typically consists of less than 10 cores while a current GPU is made up of more than 10^3 cores. The center depicts a lattice. A CPU using single core processing would integrate the Langevin equation for lattice site i and move on to site $i+1$. The use of multi-core processing would allow the shown CPU to integrate four sites simultaneously. In contrast, using GPU programming enables to evaluate the Langevin equation at about 10^3 to 10^4 sites at the same time.

5.2 Dimensional Analysis

The following section serves to relate the simulation to the experiment and to estimate initial parameters for the simulation. Quantitative experimental and theoretical results from DFT calculations are used for this purpose.

Units in the simulation

The numerical implementation of Eqs. (4.58) and (4.59) naturally uses dimensionless numbers. To assign physical meaning to the numbers, all quantities are expressed in multiples of a shared scale. Selecting the moment of inertia I as (inverse) energy scale eliminates its three appearances in Eq. (4.59). Natural units with $\hbar = c = 1$ are used in the following.

The dimensionless angular velocity Ω in units of I is

$$\Omega(t) = I\omega(t) \ . \tag{5.1}$$

The dimensionless version of Eq. (4.59) becomes

$$\begin{aligned} \Omega_{i,j}(t+\mathrm{d}t) &= \Omega_{i,j}(t) - \eta\Omega_{i,j}(t)\frac{\mathrm{d}t}{I} - I\frac{\partial V(\{\vartheta\})}{\partial\vartheta_{i,j}}\frac{\mathrm{d}t}{I} + \sqrt{\frac{2T\eta}{I^2}}n(t)I\sqrt{\mathrm{d}t} \\ &= \Omega_{i,j}(t) - \eta\Omega_{i,j}(t)\mathrm{d}\sigma - \frac{\partial v(\{\vartheta\})}{\partial\vartheta_{i,j}}\mathrm{d}\sigma + \sqrt{2\kappa\eta}n(t)\sqrt{\mathrm{d}\sigma} \ , \end{aligned} \tag{5.2}$$

with the dimensionless time, potential and temperature

$$\sigma = t/I, \tag{5.3}$$
$$v(\vartheta) = IV(\vartheta), \qquad \text{and} \tag{5.4}$$
$$\kappa = IT. \tag{5.5}$$

The dimensionless coupling constants are denoted by

$$j_\delta = IJ_\delta \qquad \text{and} \qquad \rho = Ih\ . \tag{5.6}$$

The second line of Eq. (5.2) is simulated by the numerics. The Eq. of motion (4.58) of the dimensionless buckling angle ϑ

$$\begin{aligned} \vartheta(t + \mathrm{d}t) &= \vartheta(t) + \Omega(t)\mathrm{d}\sigma = \vartheta(t) + I\omega(t)\frac{\mathrm{d}t}{I} \\ &= \vartheta(t) + \omega(t)\mathrm{d}t \end{aligned} \tag{5.7}$$

is invariant of the chosen energy scale. The moment of inertia of a silicon dimer is approximated as two point masses $m_{Si} \approx 28\,\mathrm{u} = 26\,\mathrm{GeV}$ with a distance of $2r \approx 2\,\text{Å} \approx 10\,\mathrm{keV}^{-1}$ [7], yielding

$$I \approx 2m_{Si}r^2 \approx 2\,(26\,\mathrm{GeV})\left(5\,\mathrm{keV}^{-1}\right)^2 = 1300\,\mathrm{meV}^{-1}\ . \tag{5.8}$$

In a high-temperature state, the dimers flip between the two potential minima about once per 10 ps [22]. The used step size should be much smaller than this. For $\mathrm{d}t = 1\,\mathrm{ps}$, a dimensionless step size of

$$\mathrm{d}\sigma = \mathrm{d}t/I \approx \frac{1.5\,\mathrm{meV}^{-1}}{1300\,\mathrm{meV}^{-1}} \approx 0.001 \tag{5.9}$$

would be required. However, we base the actual step size on the observed discretization error in Section A.2.

Quantitative experimental values

Brand et al. [28] determine the experimental critical temperature to 190.6 K, or

$$T_c = 16.43\,\mathrm{meV}. \tag{5.10}$$

Furthermore, they extract the correlation lengths and use Eq. (4.48) to fit the Ising model coupling constants J_δ^{Ising} to the experiment. They obtain

$$J_\parallel^{\text{Ising}} = -24.9\,\text{meV} \qquad \text{and} \qquad J_\perp^{\text{Ising}} = -0.8\,\text{meV}, \tag{5.11}$$

and a ratio of $J_\parallel^{\text{Ising}}/J_\perp^{\text{Ising}} \approx 31$. Assuming this ratio for the XY model, Eq. (4.52) can be employed to estimate J_δ^{XY}. The obtained couplings

$$J_\parallel^{\text{XY}} = 82.46\ \text{meV} \qquad \text{and} \qquad J_\perp^{\text{XY}} = 2.66\ \text{meV}\ , \tag{5.12}$$

are larger than the Ising values, which is expected [79]. The effective critical temperature is

$$T_c/J_\parallel^{\text{XY}} = 0.19899\ . \tag{5.13}$$

The effective critical temperature $T_c^{\text{XY}}/J_\parallel$ of the isotropic XY solely depends on the ratio $J_\parallel/J_\perp$. An expression can be derived by rewriting Eq. (4.52) as

$$\frac{2T_c^{\text{XY}}}{|J_\perp|} \ln\left(\frac{2T_c^{\text{XY}}}{|J_\perp|}\right) = \frac{|J_\parallel|}{|J_\perp|}\ . \tag{5.14}$$

This equation has the structure of

$$x \ln(x) = a, \tag{5.15}$$

which is solved by

$$x = e^{W_0(a)}\ , \tag{5.16}$$

with the principal branch W_0 of the Lambert W function. Resubstituting x and using the identity

$$e^{W_0(x)} = \frac{x}{W_0(x)}\ , \tag{5.17}$$

yields

$$T_c^{\text{XY}}/|J_\parallel| = \frac{1}{2W_0\left(\frac{J_\parallel}{J_\perp}\right)}\ . \tag{5.18}$$

José et al. [74] determine the qualitative relation between h and T_c by RG calculation for the anisotropic XY model with integer p. The symmetry-breaking field h is expected to increase the critical temperature of the system. Therefore, it is anticipated that the couplings of the symmetry-broken model are located between the Ising and isotropic XY values.

Fitting the coupling constants to DFT calculations

Numerous investigations calculate configuration energies of the Si(001) surface [80, 7] by density functional theory methods and fit the Ising model parameters accordingly [8, 23, 29, 81]. Their calculations will be used in the following to obtain approximate values for the symmetry-broken XY model.

The model in use has four parameters that influence the configuration energy. These are the interaction couplings $J_\parallel$ and $J_\perp$, as well as the field parameters h and p. Previous DFT calculations come to the result that the equilibrium buckling angle does not change significantly in the different surface configurations. We will approximate [8, 12]

$$\vartheta \approx 72^\circ, \tag{5.19}$$

for all reconstructions. DFT calculations determine energy differences, so that n configurations can be used to determine $n-1$ variables. Additionally, diagonal interactions $J_\times$ will be added to correctly describe the surface energies. Considering the geometries of Fig. 5.2, we can formulate the the total surface energy per dimer. The surface energy consists of the inter-dimer interaction as well as their potential energy. Periodic boundary conditions are used. The energies of

$$\begin{aligned}
c(4\times 2) \quad & \cos(4\vartheta) \quad J_\parallel + \quad \cos(4\vartheta) J_\perp + \quad 2J_\times + \cos(\vartheta p)\, h &&= E_0, \\
p(2\times 2) \quad & \cos(4\vartheta) \quad J_\parallel + \quad J_\perp + \quad 2\cos(4\vartheta) J_\times + \cos(\vartheta p)\, h &&= E_0 + E_{p(2\times 2)}, \\
p(2\times 1) \quad & \quad J_\parallel + \quad J_\perp + \quad 2J_\times + \cos(\vartheta p)\, h &&= E_0 + E_{p(2\times 1)}, \\
p(4\times 1) \quad & \quad J_\parallel + \quad \cos(4\vartheta) J_\perp + \quad 2\cos(4\vartheta) J_\times + \cos(\vartheta p)\, h &&= E_0 + E_{p(4\times 1)},
\end{aligned} \tag{5.20}$$

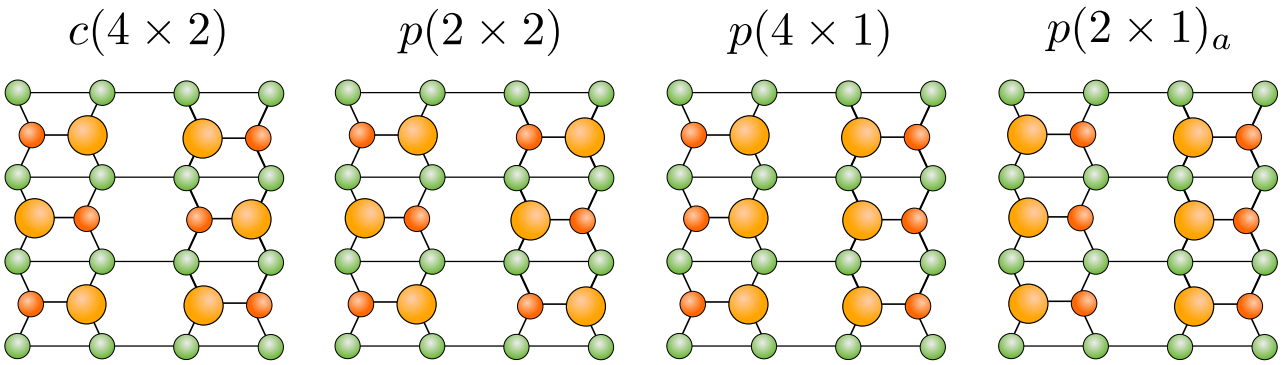

Figure 5.2: Slabs of the relevant Si(001) reconstructions are shown from a top down perspective. The upwards buckled dimers are colored in light orange and the downwards buckled dimers in dark orange. The subscript a at the $p(2\times 1)$ reconstruction denotes that the dimers are asymmetrically buckled.

are obtained from Eq. (4.53). Subtracting E_0 yields

$$\begin{aligned} 0 \cdot J_{\parallel} + \quad & (1-\cos(4\vartheta))\, J_{\perp} + \quad 2(\cos(4\vartheta)-1) J_{\times} + \quad 0 \cdot h = E_{p(2\times 2)}, \\ (1-\cos(4\vartheta))\, J_{\parallel} + \quad & 0 \cdot J_{\perp} + \quad 2(\cos(4\vartheta)-1) J_{\times} + \quad 0 \cdot h = E_{p(4\times 1)}, \\ (1-\cos(4\vartheta))\, J_{\parallel} + \quad & (1-\cos(4\vartheta))\, J_{\perp} + \quad 0 \cdot J_{\times} + \quad 0 \cdot h = E_{p(2\times 1)}. \end{aligned} \tag{5.21}$$

In the $\vartheta = \text{const.}$ approximation, these equations are independent of h. Additional configurations will be used shortly to approximate h. Solving with the values of [12], calculated by the DFT method PBEsol [82], yields

$$J_{\parallel} = 115.6 \text{ meV}, \qquad J_{\perp} = -17.3 \text{ meV} \qquad \text{and} \qquad J_{\times} = -9.5 \text{ meV} . \tag{5.22}$$

Because of the strong anisotropy, it is possible to calculate an effective $J_{\perp}$ across the dimer rows from $J_{\perp}$ and $J_{\times}$ [28]. The new $J_{\perp}$ becomes

$$J_{\perp} - 2J_{\times} \qquad \rightarrow \qquad J_{\perp} = 1.7 \text{ meV} . \tag{5.23}$$

The XY critical temperature obtained from these coupling constants

$$T_c^{\mathrm{XY}} = 18.87 \text{ meV} \tag{5.24}$$

is in proximity of the experimental critical temperature in Eq. (5.10). However, the ratio $J_{\parallel}/J_{\perp} = 68$ is much larger.

Dabrowski and Scheffler [22] describe the movement of the dimer to be in a double well potential with a barrier height of $E_B = 100$ meV. The same argumentation can be applied to [23], leading to $E_B = 170$ meV. Recent calculations from Kratzer [83] model a dimer row consisting of five dimers. The dimers are buckled antisymmetrically except for a domain boundary. The simulations describe the advance of the defect by flipping the dimer at the boundary. During the process, the dimer takes on a horizontal position. The total energy difference of the dimer rows between the domain boundary state E_{DB} and the horizontal state E_{H} is calculated to be

$$\begin{aligned} E_{\mathrm{H}} - E_{\mathrm{DB}} = J_{\parallel} \left(2\cos(2(\vartheta - \pi/2)) - 1 - \cos(4\vartheta)\right) + 2J_{\times} \left(\cos(\pi + 2\vartheta) - 1 - \cos(4\vartheta)\right) \\ + h \left(\cos(\pi p/2) - \cos(\vartheta p)\right), \end{aligned} \tag{5.25}$$

with $E_{\mathrm{H}} - E_{\mathrm{DB}} = 74\,\mathrm{meV}$. Using Eqs. (5.25) and (A.67) as well as the above values for the coupling constants to fit h and p yields

$$h = 1282 \text{ meV} \qquad \text{and} \qquad p = 2.28 . \tag{5.26}$$

Hence, the symmetry-breaking field in the experimental system is much stronger than the dimer interactions

$$h \approx 10 J_{\parallel} \ . \tag{5.27}$$

Note that the preceding considerations serve for qualitative assessment of the considered model and have no claim to be quantitatively correct.

5.3 Static Scaling

The results of the laid out simulation are presented below. First, the static properties of the adapted anisotropic XY model are examined.

The coupling constants of Eq. (5.11) are used as a starting point. The external field is initially chosen small compared to $J_{\parallel}$ to ensure approximate validity of Eq. (4.52). The dimensionless parameters given by Eq. (5.6) are set to

$$j_{\perp} = -3\,500 \ , \qquad j_{\parallel} = -110\,000 \qquad \text{and} \qquad \rho = 10\,000. \tag{5.28}$$

The dampening is fixed to $\eta = 1$ and $p = 2.5$ for now.

The correlation length extraction, as laid out in Section A.3, works best if $\xi_\delta \ll L_\delta$. Since the Si(001) surface exhibits a large correlation length anisotropy $(\xi_{\parallel}^{+}/a_{\parallel})/(\xi_{\perp}^{+}/a_{\perp}) \approx 10$ [12], it is useful to ensure that the system dimensions share a similar ratio. Accordingly, the computational effort is optimized in order to analyze correlation lengths as long as possible. The following systems have a ratio of $L_{\parallel}/L_{\perp} = 8$ if not stated otherwise. The used step size of

$$\mathrm{d}\sigma = 10^{-5} \tag{5.29}$$

is validated in Section A.2.

5.3.1 Measurement of Observables

All observables we are trying to measure are subject to fluctuations due to the thermal interaction. Usually of interest are the *ensemble averages* of systems in **thermal equilibrium**.

The ensemble average is calculated by computing the desired observable for many different realizations of the same system. The *ergodic hypothesis* assumes that the average of many realizations and the average over one long-term simulation are the same. We assume that our

system is ergodic. Since GPU accelerated programming is employed, we want to harness the full potential of the graphical processing unit. Systems of sufficient scale should be simulated to optimize GPU usage. Depending on the GPU, good performance is usually acquired by using systems with about $N = 5 \cdot 10^5 ... 1 \cdot 10^6$ lattice sites. For many use cases, e.g. calculating the Binder cumulant U_L, systems of this size are not required. Therefore, always a number $n \approx N/(L_\parallel L_\perp)$ of independent subsystems is simulated. Those systems are used in combination with the ergodic hypothesis to get the best ensemble averages available. For a simulation of n subsystems over a time t, the ensemble average of a quantity f is calculated via

$$\langle f \rangle = \frac{1}{n \cdot t} \sum_i^n \int_0^t \mathrm{d}s f_i(s) \ . \tag{5.30}$$

When making use of the ergodic hypothesis to calculate equilibrium quantities, it is important to make sure that the system is actually equilibrated. Usually, a lower time bound t_0 is introduced to account for the relaxation time. Again, the relaxation time is not known and, therefore, t_0 is set to a fraction of t to eliminate strong fluctuations in the equilibration phase of the simulation. To eventually judge the relaxation of the system, the error of Eq. (5.30) is considered. The approach is that the equilibration introduces a large statistical deviation on the average $\langle f \rangle$. So by calculating the error $\Delta\langle f \rangle$, we can extract information about the state of equilibration of the system. The $f(s)$ are correlated for different points in time. The strength of the correlation depends on how quickly the system relaxes. To get reasonable estimates on the error of $\langle f \rangle$, we have to judge how many effectively independent measurements of f are taken by the $\mathrm{d}s$ integration in Eq. (5.30). The error calculation for a time series $f_i(s)$ is done in Section A.4. Analyzing $f_i(s)$ as time series helps to avoid terminating the simulation too early for slowly relaxing systems. Additionally, it gives an estimate for how many measurements should be recorded in order not to overflow with data.

On the run, $f_i(s)$ is calculated and saved for discrete time steps $\mathrm{d}s$. The measurement time step $\mathrm{d}s$ is usually much larger than the integration step size $\mathrm{d}\sigma$

$$\mathrm{d}s \gtrsim 100 \cdot \mathrm{d}\sigma, \tag{5.31}$$

to limit the amount of data generation. The exact value depends on the integrated autocorrelation time τ_C (A.61) and is adapted during the simulation

$$\mathrm{d}s \approx \frac{1}{10}\tau_C \ . \tag{5.32}$$

5.3.2 The Critical Temperature

As mentioned, the critical temperature of the used model is not analytically calculable. To numerically determine the critical temperature, the Binder cumulant, which was introduced in subsection 3.3.2, is applied. As a reminder, the Binder cumulants for two different system sizes L_1 and L_2 intersect at the critical point $\varepsilon = 0$, satisfying

$$U_{L_1}(0) = U_{L_2}(0) = U^* \ . \tag{5.33}$$

Computing $U_L(\varepsilon)$ and determining the intersection directly yields the critical temperature. The Binder cumulant is calculated from the ensemble averages of the second and fourth moment of the lattice average in Eq. (3.43). Hence, $M_L(s)$, defined as in Eq. (4.56), is recorded during the run. The termination condition for the simulation is the error on U_L, which is given by standard error propagation and the errors on $\langle M_L^2 \rangle$ and $\langle M_L^4 \rangle$ as in Section A.4.

Eq. (4.52) is used to initially guess the critical temperature. It is expected that the parameter h increases T_c in a manner that has been shown by José et al. [74]. The critical strength of the symmetry-breaking field h_c according to them behaves as

$$h_c \propto e^{-AT^2 e^{B/T}} \ , \tag{5.34}$$

with positive constants A and B . This equation is valid for small h_c.

Results for the measurement of $L_1 = 64$ and $L_2 = 128$ with periodic boundary conditions are shown in Fig. 5.3. Note that the value of U^* depends on the boundary condition and the shape of the system, but the critical temperature does not. The systems are started from a totally ordered state. The determined effective critical temperature is

$$T_c/J_\parallel = 0.2743 \pm 0.0012 \tag{5.35}$$

at

$$\beta_c h = 0.3314 \pm 0.0030. \tag{5.36}$$

Comparing with Eq. (5.13) confirms that the critical temperature is significantly influenced by the the symmetry-breaking field. The uncertainty on the critical temperature is conservatively estimated to be half of the interval step size $\Delta T_c = \frac{1}{2}\mathrm{d}T$.

Computations with the actual experimental parameters from Section 5.2 have proven to be difficult to simulate. The same is the case with the ratio $J_\parallel/h$ of Eq. (5.27). The height of

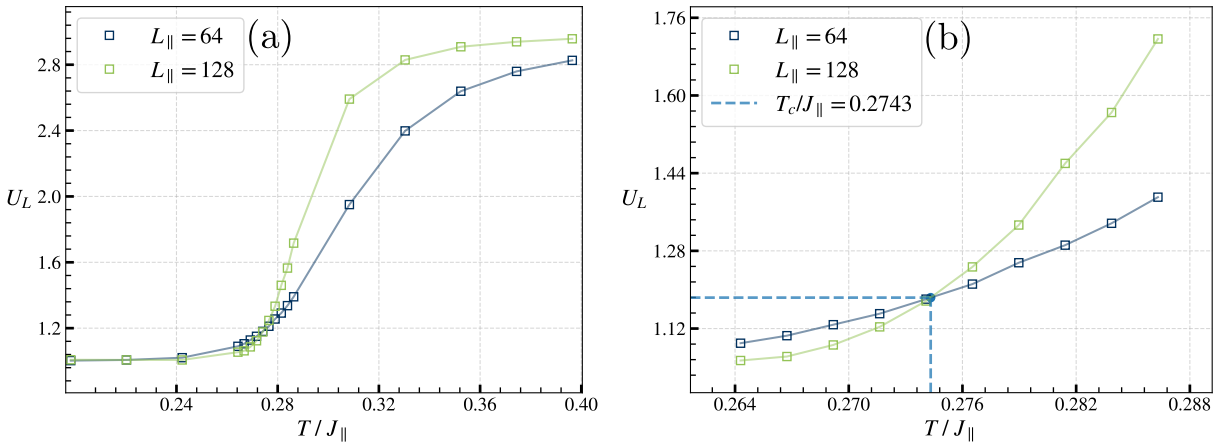

Figure 5.3: The Binder cumulant U_L is shown in dependence of the temperature for the system sizes $L_1 = 64$ and $L_2 = 2L_1 = 128$. The measured data points are squares connected by linear interpolations to guide the eye. The system parameters are defined in Eq. (5.28). **(a)** A coarse measurement for ten temperatures with $T_{\text{min}} = T_c^{\text{XY}}$ and $T_{\text{max}} = 2T_c^{\text{XY}}$ yields an approximation of T_c. **(b)** In the interval of the intersection, ten more measurements are performed to get a precise estimate of the critical temperature. The intersection at $T_c/J_\parallel = 0.2743 \pm 0.0012$ is marked with a dashed line.

the potential barrier slows down the dynamics of the system significantly as can be seen by the transition rates in [11]. For the Langevin dynamics simulation at hand, this leads to an enormous increase in computational effort. At the moment, their simulation is not feasible. However, scale invariant and universal properties will still be valid, so we will proceed with $j_\delta \approx 1$ and $h \simeq j_\delta$. The following dimensionless couplings

$$j_\parallel = 3.110, \qquad j_\perp = 0.100 \qquad \text{and} \qquad \rho = 0.283\ , \tag{5.37}$$

will be used according to Eqs. (5.35) and (5.36). The step size is increased to $\mathrm{d}\sigma = 0.01$ (see Section A.2). It will be shown that they, as expected, reproduce the same critical point. At the moment it is not sorted out why the coupling constants around $j_\delta \approx 1$ are better behaved. Physically, they should just describe a completely analogous system that is simply weaker coupled.

Finite-size effects on T_c

Due to corrections to FSS, the location of the intersection can scatter for small (L_1, L_2) pairs. In Fig. 5.4, the computed T_c is shown in dependence of the system size L_1. Again, the data points show the intersection of two curves $U_{L_1}(T)$ and $U_{L_2}(T)$ with $L_2 = 2L_1$. The simulations were performed using the parameters of Eq. (5.37). The difference in $T_c(L_1)$ is negligible between $T_c(40)$ and $T_c(64)$. So we conclude that the corrections to FSS for the critical temperature determination vanish on these length scales.

Note that calculations like shown in Fig. 5.4 are computationally expensive. The cumulant $U_L(\varepsilon)$ has to be measured for about ten different system sizes at about ten different temperatures to get a reasonable T_c estimation. Each simulation is additionally subject to thermal fluctuations and critical slowing down. Depending on L and the desired precision, the runtime for a single data point approaches or even exceeds one hour. Roughly estimated, the computation time for Fig. 5.4. comes close to 100 hours. Efficient algorithms are therefore vital (see subsubsection 5.3.4).

5.3.3 The Critical Exponent ν

Since the phase transition of the Si(001) surface shows good agreement with the Ising universality class [12], the adapted XY model should reproduce this. The XY model with a p-fold symmetry-breaking field belongs to the Ising universality class for $p = 2$ [74]. The question remains if this is still true for our adaptation with rational $p \approx 2.5$ and a reduced phase space.

Therefore, the finite-size techniques of Section 3.3 and the Binder cumulant are employed to extract the critical exponent. The measurements of Fig. 5.4 can be reused to calculate the derivative $\frac{\partial U_L}{\partial \varepsilon}$ in dependence of the system size. In Fig. 5.5 (a) the results for selected $L \in [16, 128]$ are shown for temperatures very close to T_c. Small temperature differences between the data points require precise measurement to resolve the differences in U_L. The derivative $\frac{\partial U_L}{\partial \varepsilon}$ is calculated through a central difference. Afterwards, Eq. (3.45) is fitted to $\frac{\partial U_L}{\partial \varepsilon}(L)$. The result

$$\nu = 1.003 \pm 0.026 \tag{5.38}$$

is in excellent agreement with the Ising exponent $\nu = 1$. The matching of the static critical exponent corroborates the assumption that the modified XY model still belongs to its expected universality class.

5.3.4 Phase Diagram

The result of $\nu = 1$ is strong evidence that Eq. (5.34) is also valid. In order to confirm this assumption, a phase diagram in the h-T-plane is recorded. This is a computationally intensive task as it requires the measurement of many critical temperatures. An efficient and mostly autonomous algorithm for the T_c estimation is therefore important.

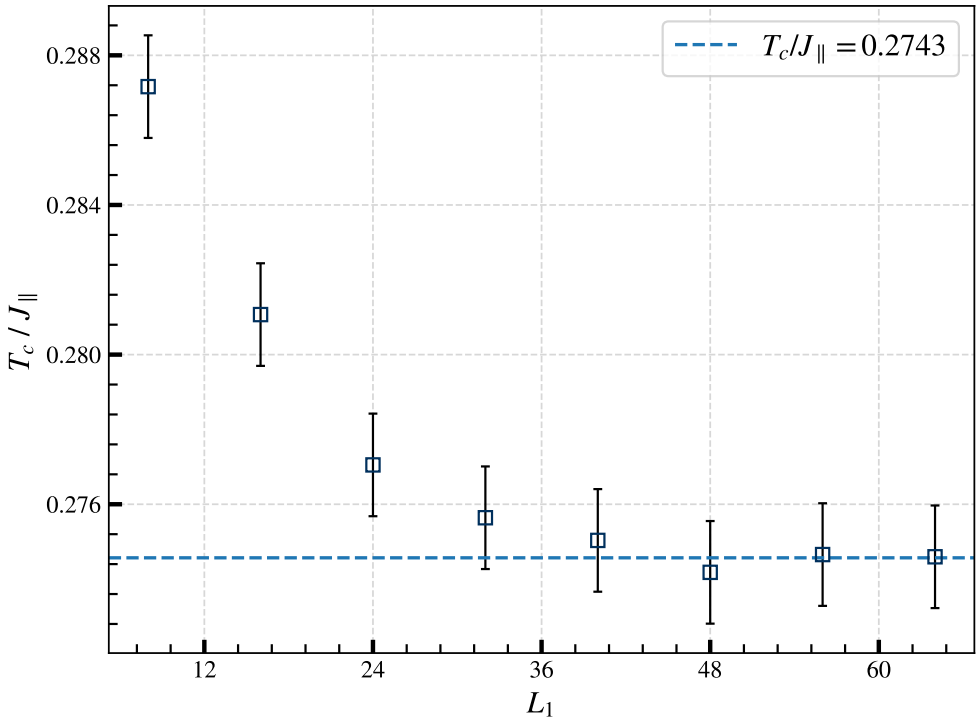

Figure 5.4: The dependence of the critical temperature $T_c(L_1)$ on the system size is shown. The Binder cumulant intersection is calculated between L_1 and $L_2 = 2L_1$. The uncertainties are estimated to be half of the temperature step size $\mathrm{d}T/J_\parallel = 0.0027$ that has been used to determine the intersection. The difference of $\Delta T_c/J_\parallel \approx 10^{-4}$ between the largest recorded system sizes is negligible and much smaller than the uncertainties. The simulations were performed using the parameters of Eq. (5.37). The result $T_c(64)/J_\parallel = 0.2743$ of Fig. 5.3 is shown as a dashed line. The effective critical temperature is indeed invariant between the parameter sets of Eqs. (5.37) and (5.28).

Efficient T_c determination

For the computation of T_c and ν, only the U_L values in close proximity of T_c are relevant. Of course, T_c is not known beforehand but it is nonetheless desired to spend as little time as possible calculating U_L far away from the phase transition. The relation in Eq. (4.52) is very useful for an initial T_c guess. Eq. (5.34) states that the critical temperature of the symmetry-broken XY model is larger than the one of isotropic XY model, so $T_{\mathrm{min}} = T_c^{\mathrm{XY}}$ can be chosen. Experience shows that the critical temperature rarely exceeds $T_{\mathrm{max}} = 2T_c^{\mathrm{XY}}$ for the investigated h-range. Hence, the first two temperatures recorded will always be T_c^{XY} and $2T_c^{\mathrm{XY}}$. The difference

$$\Delta U(L_1, L_2, \varepsilon) = |U_{L_1}(\varepsilon) - U_{L_2}(\varepsilon)|, \tag{5.39}$$

depends on the actual system sizes. To resolve the intersection even when subject to uncertainties, it is desirable to work with a ΔU that is a steep function in ε around $\varepsilon = 0$. The difference $\Delta U(L_1, L_2, \varepsilon \neq 0)$ should grow as fast as possible when the system moves away from

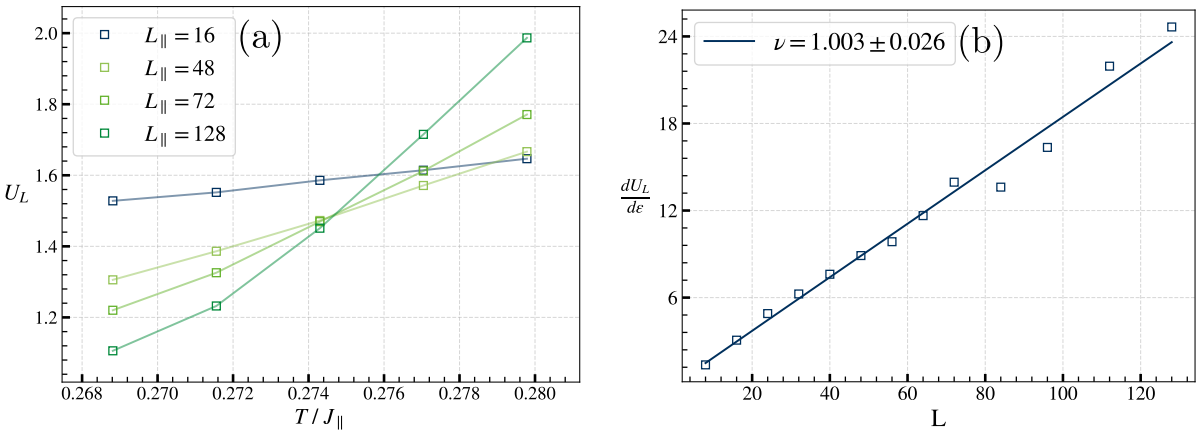

Figure 5.5: (a) The results of $U_L(\varepsilon)$ for selected sizes $L \in [16, 128]$ are measured close to the critical point. Ignoring finite-size corrections, all cumulants intersect approximately at the same point $(\beta_c J_\parallel)^{-1} = 0.2743$. **(b)** The derivatives $\frac{\partial U_L}{\partial \varepsilon} \propto L^\nu$ are shown in dependence of the system size. They are calculated using a standard central difference method with the data points of (a). The fitting yields $\nu = 1.003 \pm 0.026$ which is in good accordance with the Ising model. The error is estimated from the fit uncertainty [84].

the critical point. Therefore, the difference in system size should be maximized while keeping the finite-size effects and computation time to a minimum. This helps to avoid artificial intersections where $U_{L_1}(\varepsilon) \approx U_{L_2}(\varepsilon)$ that occur through thermal fluctuations.

After the initial four measurements, which typically show that $T_c^{\mathrm{XY}} < T_c < 2T_c^{\mathrm{XY}}$, four new simulations will be started. The best guess is to select temperatures equally spaced between the just determined boundaries of T_c. The two added temperatures divide the initial interval in three subintervals, one of which will contain the critical temperature. The corresponding subinterval is selected as the new bounds and the procedure repeats. As soon as the determined boundaries fall below the specified precision, the algorithm is terminated.

The equilibration time of systems strongly depends on the initial condition. For example, it takes a long time for a totally unordered, high-temperature system to relax if it is coupled to a low-temperature reservoir. Hence, it is useful to initialize systems in states that are already close to their equilibrium. Of course, there is again no way of knowing the equilibrium distribution beforehand. But already performed simulations can be used as initial conditions for new runs. Hence, excluding the initial measurements at T_c^{XY} and $2T_c^{\mathrm{XY}}$, the previous simulation with temperature closest to the updated T will be used as initial state.

The phase diagram

As mentioned in subsection 5.3.2, the symmetry-breaking field has a strong influence on the dynamics of the system. The dynamics and the relaxation significantly slow down at $h/J_\parallel \approx 1$. Systems with larger h are not feasible to simulate and are omitted in the phase diagram.

The measured phase diagram for the parameters of Eqs. (5.28) and (5.37) is shown in Fig. 5.6. It roughly follows the behavior predicted by José et al. [74]. The constants of Eq. (5.34), or in other words, the shape of the phase boundary, is only dependent on the ratio $J_\parallel/J_\perp$. The $\beta h_c(T)$ curves collapse for different absolute values of the dimensionless coupling j_δ if plotted as a function of the effective critical temperature $T/J_\parallel$. The prediction by Eq. (5.34) seems to overestimate the slope of $h_c(T)$. However, this could also be an effect of the strong anisotropy of the coupling constants.

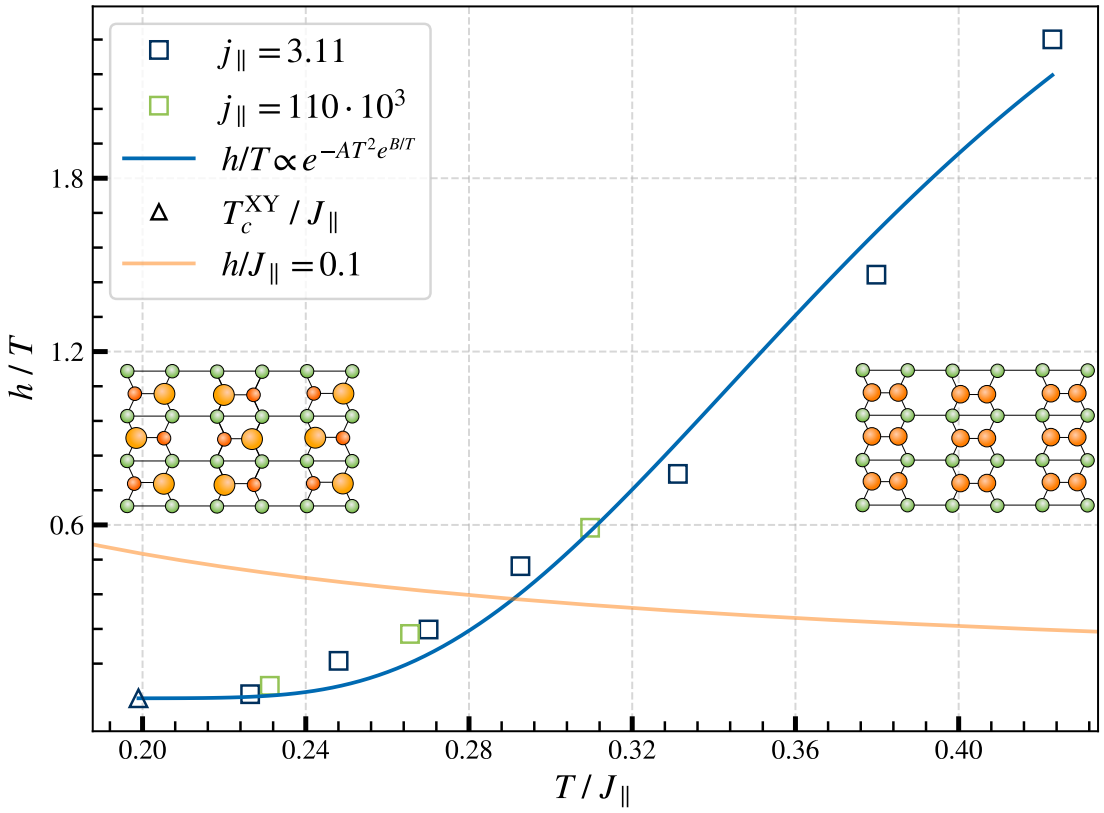

Figure 5.6: A Phase diagram in the $(T/J_\parallel)$-(h/T)-plane is shown for $J_\parallel/J_\perp = 31$. Curves for different absolute values of j_δ collapse when normalized as shown. **(a)** The critical symmetry-breaking field βh_c is plotted as a function of the effective temperature. The phase boundary follows the expected behavior from [74]. To the left of the phase boundary lies the ordered $c(4\times2)$ reconstruction. The unordered high-temperature phase, observed as $p(2\times1)$ geometry due to fast dimer flipping, is found on the right. A fit of $h/T \propto e^{-AT^2 \exp(B/T)}$ is shown in blue. We extract $A = 0.91$ and $B = 1.18$. The orange line shows an equipotential line with constant $h/J_\parallel = 0.1$. A cooled down system follows this line from right to left and crosses the phase boundary at a certain angle.

5.3.5 The Correlation Length Amplitudes ξ_δ^+

The static scaling law of the correlation length ξ_δ above but close to the critical temperature ($\varepsilon \gtrsim 0$), given by Eq. (3.29), can be rewritten as

$$\xi_\delta(\varepsilon) = \xi_\delta^+ \varepsilon^{-\nu} \ , \tag{5.40}$$

for anisotropic systems. The proportionality factors ξ_δ^+ are called the correlation length amplitudes. The correlation lengths in the Ising model can be analytically expressed in terms of the temperature and the coupling constants J_δ. Their relation above the critical temperature is given by Eq. (4.48). An expansion of Eq. (4.48) around T_c leads to the expression

$$\sinh\left(\frac{2|J_\delta|}{k_B T_c}\right) = \frac{\xi_\delta^+/a_\delta}{\xi_{\bar{\delta}}^+/a_{\bar{\delta}}} \ . \tag{5.41}$$

This relation is exceptionally useful, as it can be used to determine the coupling energies J_δ from the measured correlation lengths and critical temperature. The experimental amplitude ratio obtained by Brand et al. [28, 12] is $(\xi_\parallel^+/a_\parallel)/(\xi_\perp^+/a_\perp) = 10.3$. The coupling constants subsequently calculated from Eq. (5.41) are given in Eq. (5.11).

An expression like Eq. (5.41) for the anisotropic XY model is not known at the moment. Hence, an analytic relation of the correlation length ratio to the model couplings J_δ and h is not possible. However, since the symmetry-broken XY model and the Ising model have shown to behave quite similar in the previous investigations, it is reasonable to examine the correlation length amplitude ratio for the Ising coupling constant ratio $J_\parallel/J_\perp \approx 30$. To extract ξ_δ^+, the scaling of ξ_δ^{-1} is considered, which is given by

$$\xi_\delta^{-1}(T) = \frac{1}{\xi_\delta^+}\left(\frac{T-T_c}{T_c}\right) = -\frac{1}{\xi_\delta^+} + (T_c\xi_\delta^+)^{-1} T \ , \tag{5.42}$$

using the result $\nu = 1$. Therefore, ξ^{-1} behaves linearly in T around the critical point.

The amplitude ratio is investigated by preparing the system in a random state and letting it relax at a fixed temperature $T \gtrsim T_c$. To judge whether the system is relaxed and at the same time obtain a precise value for the equilibrium correlation length, ξ_δ is monitored on the run like described in subsection 5.3.1. The correlation length extraction is described in Section A.3. The chosen system sizes are large to minimize finite-size effects. They increase from $L_\parallel = 1024$ to $L_\parallel = 4096$ as T_c is approached.

The results are shown in Fig. 5.7. Figures 5.7 (a) and (d) display the correlation length and its inverse for $J_\parallel/J_\perp = 30$ and $\beta_c h \approx 0.5$. The correlation length ratio of $\xi_\parallel^+/\xi_\perp^+ = 5.3$ in units

of $a_\delta = 1$ is smaller than expected for the Ising model. Reasons for this could be influences of the symmetry-breaking field or simply structural differences in the relationship of the coupling constants and the correlation lengths. To investigate the influence of h on $\xi_\parallel^+/\xi_\perp^+$, the measurement is repeated with $\beta_c h \approx 0.1$. Figures 5.7 (c) and (f) show that the quantitative values of the amplitudes change, but the ratio $\xi_\parallel^+/\xi_\perp^+ = 5.0$ stays virtually the same. More measurements are needed to exclude a dependence of $\xi_\parallel^+/\xi_\perp^+$ on $\beta_c h$. However, a strong dependency is improbable.

To approach the experimental ratio of $\xi_\parallel^+/\xi_\perp^+ \approx 10.3$, a simulation with $J_\parallel/J_\perp = 100$ at $\beta_c h \approx 0.5$ is performed. The results, displayed in Figs. 5.7 (c) and (d) have an amplitude ratio of $\xi_\parallel^+/\xi_\perp^+ \approx 10.3$. The chosen coupling constant ratio happens to precisely match the experimental ratio, so no further measurements are needed.

Note that when changing the ratio of $J_\parallel/J_\perp$, we effectively move in the four-dimensional phase space of the anisotropic XY model. Figure 5.6 is solely a cross section of the phase volume. Therefore, it cannot be used to estimate the transition temperatures of different coupling constant ratios. We can, however, guess the qualitative behavior. The effective critical temperature of the isotropic XY model for $J_\parallel/J_\perp = 100$ is

$$T_c^{\mathrm{XY}}/J_\parallel = 0.148 \; . \tag{5.43}$$

So the triangle in Fig. 5.6 is shifted to the left. We expect that the qualitative behavior is essentially the same, so one can get a rough picture of the new phase diagram by shifting the whole boundary to lower effective critical temperatures.

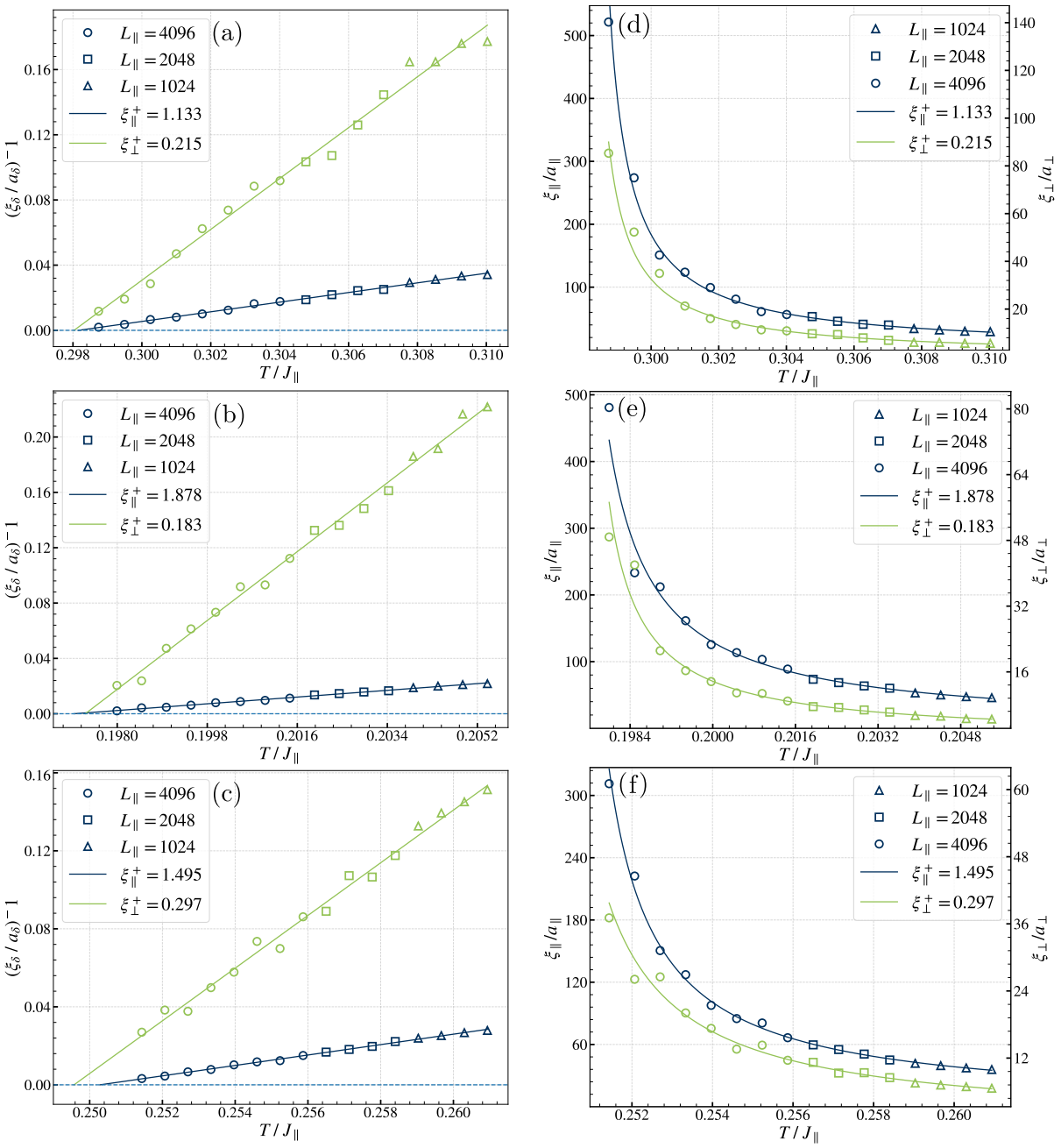

Figure 5.7: The correlation length is measured for $T \gtrsim T_c$. Panels **(a) - (c)** show the inverse correlation length $(\xi_\delta/a_\delta)^{-1}$. The system size increases from $L_\parallel = 1024$ to $L_\parallel = 4096$ as the critical point is approached. Linear fits with ξ_δ^+ as in Eq. (5.42) are shown for both lattice directions. The system undergoes the phase transition roughly where the lines intersect the zero axis marked by a dashed line. The ratio of the interaction couplings in (a) is $J_\parallel/J_\perp = 30$, leading to an amplitude ratio of $\xi_\parallel^+/\xi_\perp^+ \approx 5.3$ at $\beta_c h \approx 0.5$. This amplitude ratio is significantly smaller than the Ising value $\xi_\parallel^+/\xi_\perp^+ = 10.3$ given by Eq. (5.41). The interaction strength ratio is increased to $J_\parallel/J_\perp = 100$, keeping $\beta_c h = 0.5$, in (b), resulting in $\xi_\parallel^+/\xi_\perp^+ \approx 10.3$. This happens to match the experimental ratio precisely. Plot (c) has the same parameters as (a), but with a smaller symmetry-breaking field $\beta_c h \approx 0.1$. Small symmetry-breaking fields increase the absolute value of ξ_δ^+, but their ratio $\xi_\parallel^+/\xi_\perp^+ \approx 5.0$ stays essentially the same. In **(d) - (f)**, the divergence of the correlation length is shown together with the fit from corresponding inverse considerations on the left.

5.4 Dynamic Scaling

The dynamic universality classes are subgroups of the static ones [42] and the adapted anisotropic XY model could be in a different dynamic universality class than the two dimensional Ising model. In the following, quench dynamics are investigated and the dynamic critical exponent z is extracted.

The dynamics are studied for the system of Figs. 5.7 (c) and (d), so for a system with

$$J_{\parallel}/J_{\perp} = 100 \qquad \text{and} \qquad \beta_c h = 0.5070 \pm 0.0006 \approx 0.5 \; . \tag{5.44}$$

The critical temperature

$$T_c/J_{\parallel} = 0.19725 \pm 0.00023 \tag{5.45}$$

is extracted from the intersection with the x-axis in Fig. 5.7 (c). The uncertainty is estimated as the difference between the intersection points in the two lattice directions. The used dimensionless parameters are conveniently chosen

$$j_{\parallel} = 10, \qquad j_{\perp} = 0.1 \qquad \text{and} \qquad \rho = 1. \tag{5.46}$$

If large h would have been feasible to simulate, the determined ratio of $J_{\parallel}/J_{\perp}$ could have been used together with the phase diagram and the experimental value of h to determine quantitative values for the coupling constants J_δ of the anisotropic XY model fitted to the silicon surface. This approach was not successful, but the qualitative and universal results of the dynamic should still be valid.

5.4.1 The Kibble-Zurek Mechanism

First, Eq. (3.54) and the Kibble-Zurek mechanism will be investigated. Since ν is already known, fitting the exponent $\nu/(1+\nu z)$ to quenched correlation lengths determines the dynamic exponent z.

The used quench protocol, i.e. the manner in which the system is cooled down, is an isotropic, linear quench following Eq. (3.49). The starting temperature $\varepsilon(t_{start}) < \varepsilon(\hat{t})$ is chosen to be sufficiently far away to observe adiabatic system evolution before crossing the freeze-out point. The end temperature $\varepsilon(t_{end})$ is chosen in symmetric distance from the transition point $|\varepsilon(t_{start})| = |\varepsilon(t_{end})|$. Before the quench, the system is randomly initialized and equilibrated with a bath of the starting temperature. Fig. 5.8 shows the concept of the quenching process. Color meshs are constructed to illustrate the dimer buckling angle and connected domains.

A checkerboard transformation is applied to the lattice values in order to visualize connected domains.

Figures 5.9 (a) and (b) show the current system correlation length as a function of the quench time. Measured equilibrium values are displayed to reference adiabatic evolution. A fit of the frozen correlation lengths $\hat{\xi}$ to Eq. (3.54) is performed in Figs. 5.9 (c) and (d). It was made sure that $\hat{\xi}_\delta \ll L_\delta$ so that the correlation length extraction method of Section A.3 is still applicable. Therefore, the system size is doubled if $\hat{\xi}_\delta$ exceeds $0.1L_\delta$. For rapid quenches, the system behaves initially already non-adiabatic and the correlation length plateaus. The linear scaling starts after a short transition phase. The extracted KZM exponents of $\nu/(1+\nu z) = 0.471$ and $\nu/(1+\nu z) = 0.458$ in the parallel and perpendicular lattice direction are unusually large compared to the expected exponent of 0.33. Calculating the dynamic critical exponent yields $z \approx 1.5$. This is significantly smaller than the expectation $z_{\text{Ising}} = 2.16$ from previous research on the Ising model shown in Table 4.1.

Except for small deviations for systems where $\hat{\xi}_\delta \lesssim L_\delta$, the scaling region behaves mostly linear in the logarithmic plot. Hence, there is no initial reason to suspect that the scaling region has not been reached yet. Another reason for the deviation could be that the simulated model belongs to a different dynamic universality class than the Ising model. Hence, a KZM-independent z extraction method is applied to further investigate the dynamic critical exponent.

5.4.2 The Critical Exponent z

One way to examine the dynamic critical exponent is to consider the relaxation of the Binder cumulant including finite-size scaling. This method was introduced by Li et al. [85] and will be used in the following to extract z.

The basis is the time-resolved FSS of the (n)-th moment of the magnetization [85]

$$M^{(n)}(t, \varepsilon, L_1) = b^{-n\beta/\nu} M^{(n)}(b^{-z}t, b^{1/\nu}\tau, b^{-1}L_1) \ , \tag{5.47}$$

with $b = \frac{L_1}{L_2}$ being the spatial rescaling factor of two systems with dimension L_1 and L_2. Note that the subscript of Eq. (3.43) has been moved into the parenthesis. Janssen et al. [86] emphasized that the initial correlation length must be very short for Eq. (5.47) to be valid. Therefore, the investigated systems will be prepared in a high-temperature, low-order state. Following the definition of the Binder cumulant in Eq. (3.42), one can relate the Binder

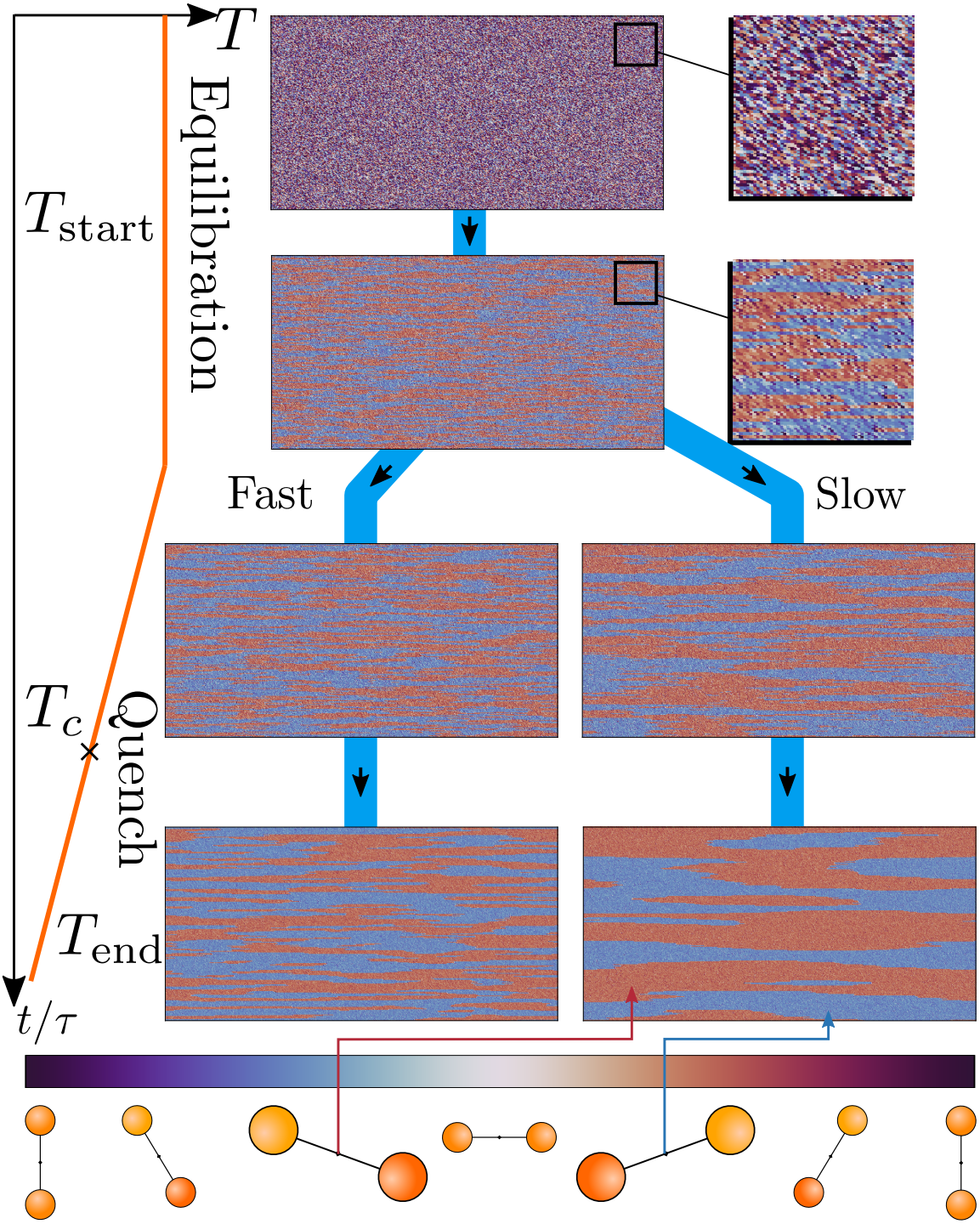

Figure 5.8: Color meshs of the simulations are shown. The coloring of the squares maps into the dimer buckling angle. The cyclic color bar on the bottom assigns the color to the dimer position. For large h, the black vertical dimer state is only realized at high temperatures. The temperature diagram on the left shows the temperature $T(t)$ of the reservoir coupled to the surface. The quench process is as follows: First, a totally unordered system on the top is coupled to a reservoir with the starting temperature T_{start}. The equilibration phase yields the system below. The zoom windows show a visual difference in order. After the equilibration, the cooling down is started. Depending on how fast or slow the quench is done, following the left or right path, smaller or larger domains of order establish. The domains of order can be made out midway during the quench at T_c, but eventually manifest on the way to T_{end}. Note that a checkerboard transformation is applied to visualize connected domains.

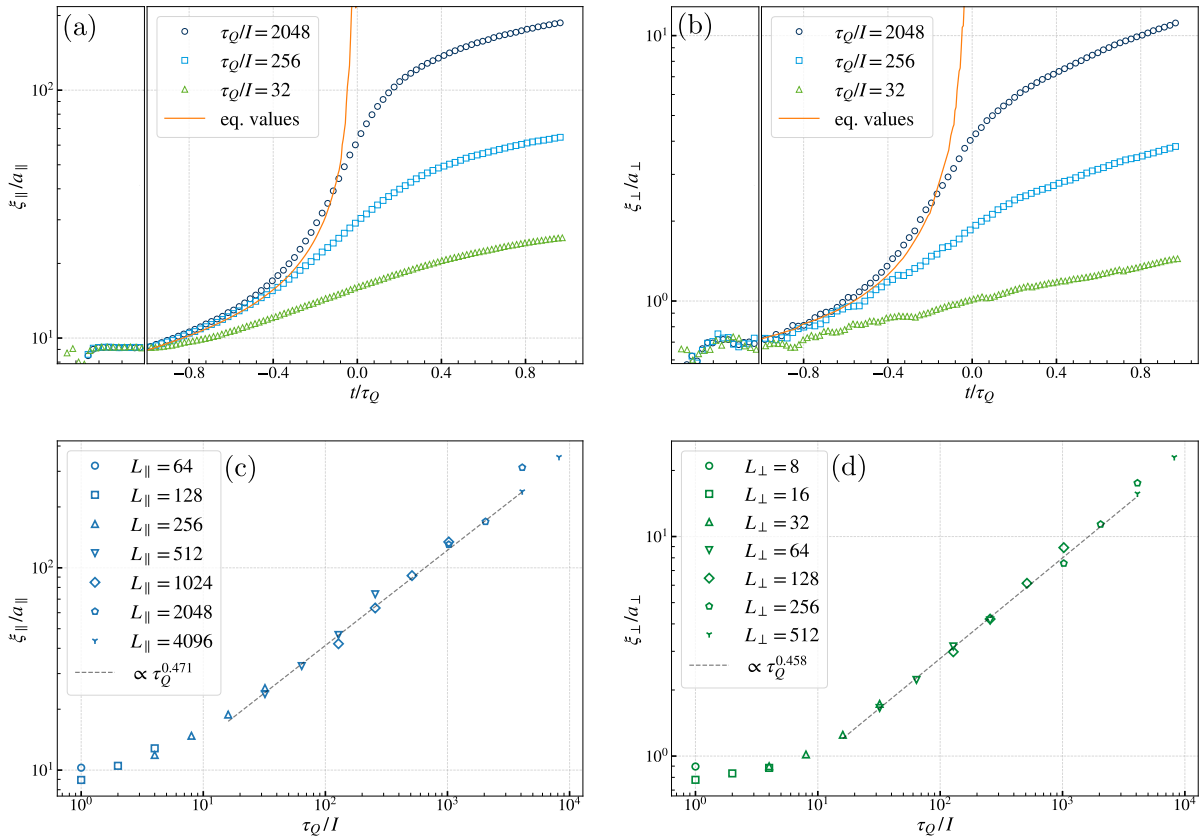

Figure 5.9: Quenches are examined for the system described at the beginning of Section 3.4. The system sizes are chosen so that the frozen correlation length is smaller than $L_\delta/10$. Figures **(a)** and **(b)** show the time resolved quench process, meaning the current system correlation lengths $\xi_\parallel$ and $\xi_\perp$ versus the scaled quench time t/τ_Q. The reservoir passes the critical temperature at $t/\tau_Q = 0$. The left part of the plots shows the equilibration phase. Measured equilibrium correlation lengths with $\xi_\delta < 0.1 L_\delta$ are shown in orange. The slowly quenched systems follow the equilibrium correlation length nicely until close to the phase transition. The fact that the quenched system with $\tau_Q/I = 2048$ lies slightly above the equilibrium values is most likely a finite-size effect, as the quenched system was simulated with a larger system size. It is interesting that the correlation lengths continue to grow even after the phase transition is passed. This could be due to a retardation effect between the reservoir temperature and the actual system temperature. The fully modeled inertia of the dimers and the damping of the system might reinforce this. Plots **(c)** and **(d)** show the quench scaling, i.e., the frozen correlation length after the quench versus the quench timescale. For rapid quench rates the system is unable to evolve adiabatically from the outset. The resulting frozen correlation length corresponds approximately to the equilibrium correlation length at the initial temperature, and no scaling behavior is observed. Hence, the scaling is calculated in the linear area. The extracted quench exponents of $\nu/(1+\nu z) = 0.471$ of and $\nu/(1+\nu z) = 0.458$ are larger than expected for the Ising model.

cumulant of systems with different sizes at the critical point $\varepsilon = 0$ by

$$U(t, 0, L_1) = U(b^{-z}t, 0, L_2) \ . \tag{5.48}$$

The exponent z is obtained by finding a time rescaling factor b^{-z} such that the recorded curves for U_{L_1} and U_{L_2} collapse. Since the sample systems are prepared in a high temperature state where $U_L \approx 3$, a relaxation from this value to the equilibrium U^* is expected. The results for the rescalings for sizes up to $L_2 = 144$ are shown in Fig. 5.10. The rescaling $144 \to 112$ is more reliable than $112 \to 80$ since it minimizes the finite-size corrections to the scaling law in Eq. (5.47). The rescaling $80 \to 48$ serves as reference and typically shows large finite-size corrections. The result $z = 2.18$ is close to the Ising value $z_{\text{Ising}} = 2.16$. The theoretical KZM exponent for $z = 2.18$ of $\nu/(1 + z\nu) = 0.33$ stands in contradiction to the exponents obtained directly from the quench $\nu/(1 + z\nu) \approx 0.46$. Based on the symmetry, it is expected that the adapted anisotropic XY model would show the Ising dynamical exponent. Hence, the deviation might stem from the Kibble-Zurek scaling. Since the system sizes used in the quenches are already very large, strong finite-size corrections to the Kibble-Zurek scaling can be ruled out as cause of the deviation. The most sensible explanation for the large quench exponent is that the cause has to be a systematic difference in the expected qualitative Kibble-Zurek description. An idea could be the existence of subleading scalings, like reported in [87], caused by other scaling fields than the temperature. In our case, h could be such a scaling field. Another cause might be that the KZM scaling regime has not been reached for the fast quenches simulated. Because of the contradiction between ν, z and $\nu/(1 + \nu z)$, the quench exponent will be denoted with μ_Q in the following. The scaling of the frozen correlation length becomes

$$\hat{\xi} \propto (\tau_Q)^{\mu_Q} \ . \tag{5.49}$$

If the subleading scalings described in [87] are the cause for the found deviation, then the manner in which the phase boundary is crossed influences μ_Q. For a fixed h and starting temperature T_{start}, the system traces a certain path in the phase diagram in Fig. 5.6 when cooled down. This path crosses the phase boundary at a defined angle, which in the following is called the quench angle. The quench angle is expected to open up scaling regimes, in which the quench exponent does not follow the Kibble-Zurek scaling, but is influenced by other critical exponents. The KZM exponent is obtained by quenching orthogonally to the phase boundary or for very long quenches not accessible at the moment. By varying h, the angle of the crossing should change, although it has not yet been further investigated to what extent. Also, it has been observed that h has a strong influence on the dynamics. Therefore, in the following we examine the effect of h on z as well as on the quench exponent. Additionally, the damping is varied as it is expected to have a significant influence on the dynamics.

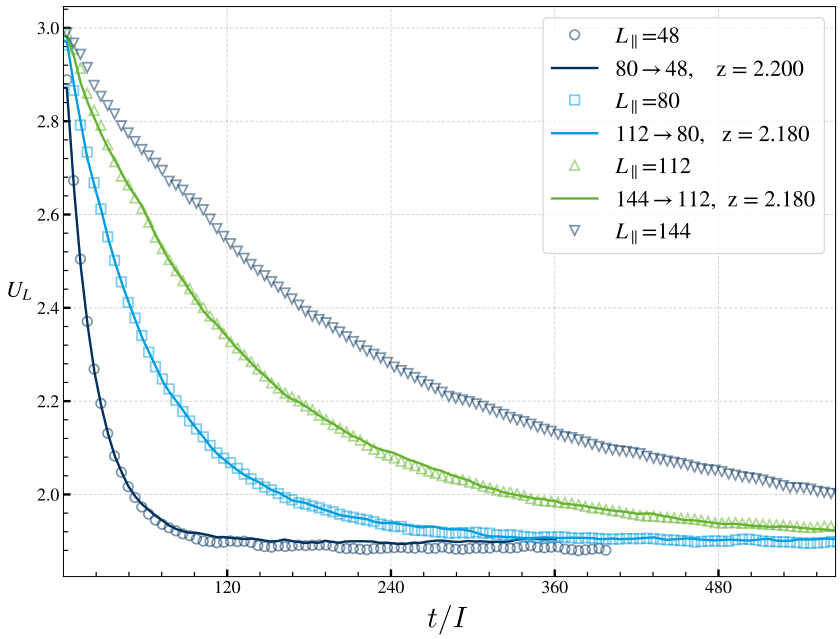

Figure 5.10: The relaxation of the Binder cumulant is shown versus the dimensionless time for the sizes $L \in \{48, 80, 112, 144\}$. The dynamic critical exponent z can be extracted by finding a time rescaling factor $(L_1/L_2)^z$ such that U_{L_1} and U_{L_2} collapse. The best rescaling of $U_{L_1} \to U_{L_2}$ is selected by rasterizing z in 0.01 steps and minimizing the squared error between the interpolated curves. The rescalings $144 \to 112$ and $112 \to 80$ both yield the dynamic critical exponent $z = 2.18$, which is very close to the Ising universality class $z = 2.16$ (see Table 4.1).

5.4.3 Influences on the Dynamics

The deviation from the KZM is very interesting, especially since the scaling arguments by Kibble and Zurek have been validated over the years in numerous theoretical and experimental investigations [43, 44, 45, 11]. As the KZM exponent is related to universal exponents that do not depend on the microscopic details of the system, it is expected not to change either if microscopic parameters are varied.

More specifically, the influence of the parameters h and η on the dynamics of the system is examined. These two parameters are especially interesting. On the one hand, a distinctive feature of Langevin dynamics simulation is the existence of η, and, on the other hand, the usage of the experimental h is not possible at the moment so its qualitative influence is highly relevant. In addition, some information about the existence of subleading scalings [87] might be obtained.

The quench results for varied effective fields $\beta_c h$ are shown in Figs. 5.11 (a) - (d). Apart from $\beta_c h$, the parameters are the same as in Eq. (5.46). The linear scaling region starts at larger timescales for strong symmetry-breaking fields. This is a clear indication that the dynamics of the system slow down with increasing h. Aside from that, the symmetry-breaking field

does not seem to have any influence on the scaling exponent. However, this does not directly disprove the hypothesis that the subleading scalings are the reason for the observed exponent. Further investigations that track the quench angle are necessary here. In Figs. 5.11 (e) and (f), the cumulant relaxation method is repeated for small and large h. The cumulant takes substantially longer to relax for large h. Between the compared field strengths of $\beta_c h = 0.3$ and $\beta_c h = 3.0$, the relaxation period extends by a factor of roughly 20. The extracted z stays comfortably above 2 and still does not agree with the corresponding quenches. Note that the cumulant relaxation method shows a strong dependence of a precise estimation of T_c. Hence, the calculated values serve as a qualitative assessment.

The results for varied η are plotted in Figs. 5.12 (a) - (d). Large dampings shift the linear scaling region to larger τ_Q. Small η reveal the existence of a hump in the scaling region. The question arises whether this hump exists for all other measurements and was not observed because of too fast quenches. For small η, the quench exponent at the run-off of the hump is $\mu_Q \approx 0.7$ in both lattice directions. With the current simulation, the hump could not be passed entirely. It is not clear whether the otherwise observed quench exponent of $\mu_Q = 0.45$ arises at larger timescales, or if small dampings increase the quench exponent also for long quenches. The dynamic exponent z is extracted in dependence of η in Figs. 5.12 (e) and (f). Large dampings slow down the relaxation of the Binder cumulant. Considering the small damping, η could not be set as small as in the corresponding quench. The finite-size corrections seemed to have a stronger influence here. In other words, the exponent z grows with the system size used and it was not feasible to reach a converged value. The rescaling $80 \rightarrow 48$ in Fig. 5.12 (e) also shows stronger finite-size dependence than Fig. 5.12 (f). Apart from that, no indications for the influence of η on z are found.

The investigations of η and h gave some insights on their influences on the dynamics, but the nonuniversal behavior of the quench exponent remains unclear for now. Further investigations are needed that determine the influence h and η more clearly. In addition, examinations of the quench angle could be worthwhile.

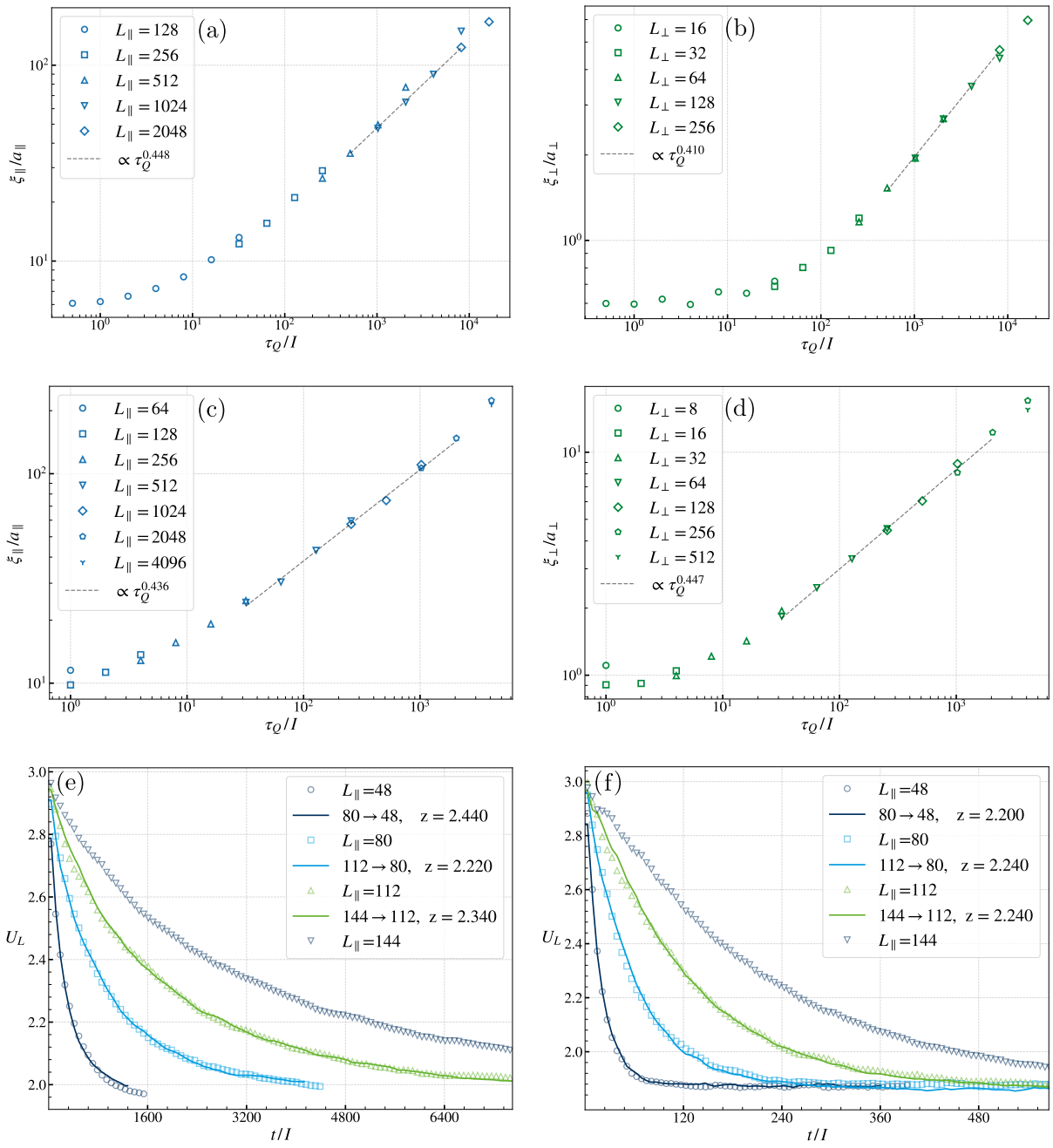

Figure 5.11: Quenches are examined for the different strengths of the symmetry-breaking field. Panels **(a)** and **(b)** show the results for a large symmetry-breaking field of $\beta_c h \approx 3.0$ for the two lattice directions. Figures **(c)** and **(d)** represent a small symmetry-breaking field of $\beta_c h \approx 0.3$. Like in Fig. 5.7, a larger h reduces the quantitative value of the correlation length. Also, as mentioned in subsection 5.3.3, the responsiveness of the systems decreases substantially. The linear scaling region starts earlier for small h and the extent of the plateau decreases. This further has the effect that smaller systems can be used up to larger cooling times, as their correlation length is shorter. The quench exponent does not show a dependence on $\beta_c h$. Panels **(e)** and **(f)** show the relaxation of the Binder cumulant for systems with $\beta_c h \approx 3.0$ and $\beta_c h \approx 0.3$. The large symmetry-breaking field drastically slows down the dynamics, but has no influence on the dynamic exponent, which remains greater than two.

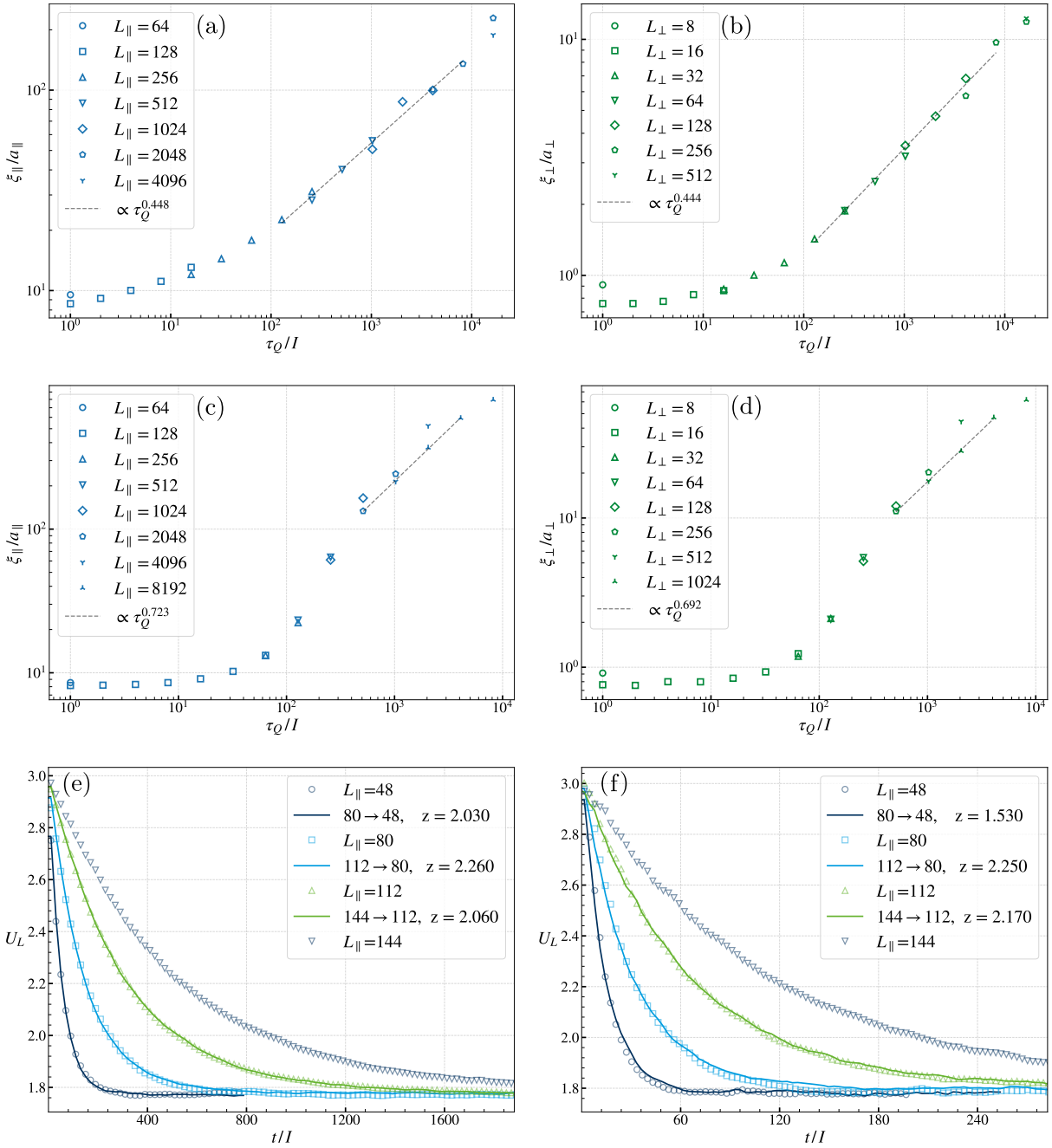

Figure 5.12: Quenches are examined for different η. Panels **(a)** and **(b)** show the results for a large dampening of $\eta = 10$. Figures **(c)** and **(d)** display the results for a small damping of $\eta = 0.01$. Compared to Figs. 5.9 (c) and (d), the quench scaling region starts later for large damping. The quench exponent is approximately identical. For small dampings, a hump in the scaling becomes visible. This is very interesting and might be related to [87]. The question arises as to whether this hump also exists on all other curves and was not observed by quenching too quickly. This might be an explanation for the systematically larger quench exponent that we observe. At the right end of the hump, the quench exponent $\mu_Q \approx 0.7$ is significantly larger than in the overdamped case. Figures **(e)** and **(f)** show the relaxation of the Binder cumulant for systems with $\eta = 0.5$ and $\eta = 5$. The large damping slows down the dynamics significantly. Small dampings seem to be more strongly influenced by finite-size corrections as the rescaling of $80 \to 48$ indicates. The calculated dynamic critical exponent stays above two.

5.5 Discussion

The adapted XY model, developed to describe the Si(001) surface, is largely in line with the theory. This includes the phase diagram, the static critical exponent ν and the dynamic critical exponent z. It is interesting to note here that the renormalization group calculations by José et al. [74], which were originally performed for integer p, appear to be valid for rational p as well. Also, cutting the phase space in half by introducing a parameter m in Eq. (4.54) does not seem to have an effect whatsoever. The assumption is that the universal behavior of the treated model solely depends on the continuity of the state parameter and the number of minima of the symmetry-breaking field. José et al.'s predictions have previously been studied by Monte Carlo methods [40, 46] for $p = 4$. Both find a continuous phase transition with nonuniversal critical behavior, as is expected for $p = 4$. Rastelli et al. [46] find the Ising critical exponent in the limit of large h. The presented investigations join them in confirming José et al. and expand the argument to rational p and the dynamic universality class.

The description of the silicon surface using the anisotropic XY model differs from previous Ising model descriptions by the fact that much larger interaction strength ratios of $J_{\parallel}^{\mathrm{XY}}/J_{\perp}^{\mathrm{XY}} \approx 100$ are needed to reproduce the experimental correlation length ratio of $\xi_{\parallel}^{+}/\xi_{\perp}^{+} \approx 10$. the theoretical result of the Ising model from Eq. (5.41) yields $J_{\parallel}^{\mathrm{Ising}}/J_{\perp}^{\mathrm{Ising}} \approx 30$. Also, roughly a factor of two larger coupling constants are required to reproduce the experimental transition temperature. This is expected since $J \cos \Delta\vartheta < J$ [79].

An advantage of the Langevin dynamics modeling of the silicon surface is that, in principle, the dynamics on the surface can be examined in a more realistic manner. A large disadvantage is the significantly higher computational expense. The effect of strong symmetry-breaking fields proves to slow down the dynamics on the surface drastically. Neither equilibration nor significant dynamic phenomena can be simulated with current methods. The slowdown of the dynamics has been observed in both the quenches and the relaxation of the Binder cumulant in Fig. 5.11. Other than the slowdown, the strength of h does not seem to influence the KZM scaling. Large dampings slow down the dynamics but the quench exponent remains invariant. Small dampings reveal a hump in the scaling region which shows a significantly larger exponent. Also, the scaling does not show a systematic dependence on the lattice direction. Our simulations predict a value of

$$\mu_Q = 0.445 \pm 0.006 \tag{5.50}$$

for the nonuniversal quench exponent μ_Q. The value is obtained by averaging over all performed quenches with the exception of the strongly underdamped case $\eta = 0.01$. The uncertainty is the standard deviation of the mean. This constitutes a significant divergence from

the Ising scaling. The nature of this deviation is not clear at the moment and the explanations could range from simply to rapid quenches to something more fundamental. Schaller et al. [11] use kinetic Monte Carlo methods to simulate an Ising model with the values of Eq. (5.11). They extract a KZM exponent of $\mu_{\text{quench}} \approx 0.35$, which is in good accordance with the theoretical Ising value. The quench angle in the $\beta J_{\parallel}$-$\beta J_{\perp}$-plane of the phase space is quite similar between the Ising and the XY model (see Fig. 4.2). Hence, the quench angle in this cross section may be ruled out as the source of the quench exponent deviation. However, other than in the antiferromagnetic symmetry-broken XY model, the barrier height of the on-site potential has no influence on the critical point in the Ising model. The quench angle in the h-dimension of the anisotropic XY model may therefore still be the cause of the untypically large μ_Q.

Schaller et al. further observe that the frozen correlation length ratio $\hat{\xi}_{\parallel}/\hat{\xi}_{\perp}$ in the linear scaling region is twice the equilibrium ratio $\xi_{\parallel}/\xi_{\perp}$. They explain this phenomenon with the argument that the weakly coupled direction diverges earlier from the equilibrium behavior than the strongly coupled direction. This results in the fact that the linear KZM scaling regime starts at larger cooling times for the weakly coupled direction, which is also visible in these investigations. The effect is strongest for the large symmetry-breaking field in Fig. 5.11. In the anisotropic XY model, the ratio $\hat{\xi}_{\parallel}/\hat{\xi}_{\perp}$ is heavily influenced by h. Table 5.1 shows the frozen correlation length ratio in comparison with the amplitude ratio $\xi_{\parallel}^{+}/\xi_{\perp}^{+}$. Their ratio seems to saturate for large h but exceeds the Ising value.

Table 5.1: The ratio of final correlation lengths $\left(\hat{\xi}_{\parallel}/\hat{\xi}_{\perp}\right)$ increases with $\beta_c h$. It is compared to the correlation length amplitude ratio $\xi_{\parallel}^{+}/\xi_{\perp}^{+}$.

$\beta_c h$	0.3	0.5	3.0
$\left(\hat{\xi}_{\parallel}/\hat{\xi}_{\perp}\right) \Big/ \left(\xi_{\parallel}^{+}/\xi_{\perp}^{+}\right)$	1.3	1.5	2.6

6 Summary and Outlook

6.1 Summary

During this work, Langevin dynamics methods have been employed to investigate the phase transition on the Si(001) surface. The main point has been the step from discrete descriptions using the Ising model to a continuous formulation with an adapted XY model. The purpose of the continuous description is a more realistic modeling of dynamic non-equilibrium behavior. The used Langevin equations have been motivated from a standpoint of open quantum systems. Subsequently, they were numerically implemented using parallel processing techniques on GPUs. The well-established BBK method has been used as integration scheme for the stochastic differential equations.

Finite-size techniques like the Binder cumulant were applied to determine the critical temperature of the adapted XY model in dependence of the model parameters $J_\parallel$, $J_\perp$ and h. A phase diagram of the T-h-plane was then recorded for $J_\parallel/J_\perp = 31$. The approximate validity of José al.'s work [74] has been shown for rational $2 < p < 3$. For the constants A and B of Eq. (5.34) we roughly estimate

$$A = 0.91, \qquad B = 1.18 \qquad \text{at} \qquad J_\parallel/J_\perp = 31. \tag{6.1}$$

The static critical exponent ν of the symmetry-broken XY model has been determined to

$$\nu = 1.003 \pm 0.026 \tag{6.2}$$

in excellent agreement with the expected Ising value $\nu = 1$. The correlation length amplitude ratio in dependence of the coupling constant ratio has been shown to differ significantly between the Ising and the symmetry-broken XY model. Measurements for the symmetry-broken XY model yield

$$\frac{\xi_\parallel^+}{\xi_\perp^+} = 5.2 \qquad \text{at} \qquad \frac{J_\parallel}{J_\perp} = 30, \tag{6.3}$$

and

$$\frac{\xi_{\parallel}^{+}}{\xi_{\perp}^{+}} = 10.3 \qquad \text{at} \qquad \frac{J_{\parallel}}{J_{\perp}} = 100. \tag{6.4}$$

Subsequently, the dynamics on the silicon surface have been studied for $J_{\parallel}/J_{\perp} = 100$. The quench exponent has been extracted to

$$\mu_{\text{quench}} = 0.445 \pm 0.006 \ , \tag{6.5}$$

which is significantly larger than the expected Ising value. Following this, the relaxation of the Binder cumulant has been considered to extract the dynamic critical exponent. The measured exponent of

$$z = 2.18 \tag{6.6}$$

is again in very good agreement with the Ising universality class. The influences of the amplitude of the symmetry-breaking field as well as damping η on dynamic and quench exponent have been investigated. No connection could be established.

The contradiction of ν, z and μ_{quench} is surprising, but also very intriguing. The investigated symmetry-broken XY model reproduces theoretical predictions for the most part. This includes the static exponent ν, the critical temperature and the phase diagram, as well as the dynamic exponent z. Nevertheless, the quench exponent differs. The research of Ladewig et al. [87] could be a resolution to this. This argument explains the deviation with the angle between the quench path and the phase boundary in Fig. 5.6. The KZM exponent would then show up for longer quench times, which are not accessible at the moment.

6.2 Outlook

The analyses carried out by no means exhaust the scope of simulation. Besides additional quantities to extract, useful extensions could be built into the simulation. Further measurements could include the determination of supplementary static critical exponents. Although the result of ν and z strongly suggest the Ising universality class, there might be a small possibility that the model belongs to another static universality class after all. The determination of further critical exponents of Table 3.1 would reduce this probability to a miniscule one. The deviation from KZM scaling should definitely be investigated further. The measurement of as-slow-as-possible quenches might be a starting point, although from the current point of view, more than ten times longer quenches will not be realizable. This corresponds to about three data points in Fig. 5.9, which are not expected to change the scaling significantly. A

possible performance improvement could be to adapt the step size dσ of Section A.2 to the current reservoir temperature. This way simulations at low temperatures should become more manageable.

If the deviation from the KZM exponent is caused by the subleading scalings described in [87], another approach could be to quench orthogonal to the phase boundary. The expected KZM scaling should then be observed. Also, the extraction of z could be confirmed and refined. This could be done by employing another dynamic critical exponent extraction method [88].

An interesting avenue of further research is the investigation of the parameter p. Its principal role is described in Section A.5. As long as $p \in [2, 3]$, so that the number of minima of the symmetry-breaking field stays the same, it is not expected that the parameter changes the critical behavior. However, descriptions including βh might have to be reformulated in terms of the height of the potential barrier. Nevertheless, the study of the influence of p on the dynamics might be worthwhile, since the parameter also changes the shape of the symmetry-breaking field.

The simulation could also be extended to incorporate next-nearest-neighbor interactions. They are not expected to change the universal behavior, but nevertheless an implementation could be useful for confirmation and might give some insights on the microscopic dynamics. However, they are only expected to influence the quantitative values, which were not accessible at the moment anyway. A simulation including next-nearest-neighbor interactions is even more costly and therefore not feasible at the moment. On shorter timescales, the flip dynamics of the dimers could be investigated and it could be checked whether the results for the dimer flip frequencies of Fu et al. [80] can be reproduced with this simplified method. A further extension would be to allow nonlinear and anisotropic quenches. In the experimental system, the cooling down is not an exactly linear quench and the temperature of the bath and the surface is not perfectly isotropic.

To conclude, the investigation of the anisotropic XY model with rational p by Langevin dynamics simulations was novel research and gives a first confirmation of the Ising-like dynamic critical exponent z. The investigation of cooling quenches showed nonuniversal behavior, possibly related to the damping or the quench angle. There are still many aspects of the simulation that need to be analyzed, especially since the amount of analytic and theoretical descriptions is rather limited. A quantitative description of the Si(001) surface seems to be out of reach at the moment, but other systems might be better suited. Furthermore, it remains the question, whether the quantitative results from the simulation can be mapped onto the experimental system.

A Appendix

A.1 Caldeira-Legget Master Equation Calculations

Markov Approximation

Consider the trace in the third term of Eq. (4.31)

$$\mathrm{tr}_B\left\{\left[\hat{\boldsymbol{H}}_I(t),\left[\hat{\boldsymbol{H}}_I(t'),\hat{\boldsymbol{\rho}}_S(t')\otimes\overline{\rho}_B\right]\right]\right\}=\mathrm{tr}_B\left\{\left[\hat{\boldsymbol{x}}(t)\otimes\hat{\boldsymbol{B}}(t),\left[\hat{\boldsymbol{x}}(t')\otimes\hat{\boldsymbol{B}}(t'),\hat{\rho}_S(t')\otimes\overline{\boldsymbol{\rho}}_B\right]\right]\right\}. \tag{A.1}$$

Multiplying out the commutator yields

$$\begin{aligned}\text{(A.1)}\ =\mathrm{tr}_B\Big\{&+\hat{\boldsymbol{x}}(t)\hat{\boldsymbol{x}}(t')\hat{\boldsymbol{\rho}}_S(t)\otimes\hat{\boldsymbol{B}}(t)\hat{\boldsymbol{B}}(t')\overline{\rho}_B-\hat{\boldsymbol{x}}(t)\hat{\boldsymbol{\rho}}_S(t)\hat{\boldsymbol{x}}(t')\otimes\hat{\boldsymbol{B}}(t)\ \overline{\rho}_B\hat{\boldsymbol{B}}(t')\\&-\hat{\boldsymbol{x}}(t')\hat{\boldsymbol{\rho}}_S(t)\hat{\boldsymbol{x}}(t)\otimes\hat{\boldsymbol{B}}(t')\overline{\rho}_B\hat{\boldsymbol{B}}(t)+\hat{\boldsymbol{\rho}}_S(t)\hat{\boldsymbol{x}}(t)\hat{\boldsymbol{x}}(-\tau)\otimes\overline{\rho}_B\hat{\boldsymbol{B}}(t')\hat{\boldsymbol{B}}(t)\Big\}\ .\end{aligned} \tag{A.2}$$

The factors belonging to the Hilbert space of the system can be pulled out of the trace. Additionally we use the cyclic property of the trace to obtain

$$\begin{aligned}\text{(A.2)}=\ &\left(\hat{\boldsymbol{x}}(t)\hat{\boldsymbol{x}}(t')\hat{\boldsymbol{\rho}}_S(t')-\hat{\boldsymbol{x}}(t')\hat{\boldsymbol{\rho}}_S(t')\hat{\boldsymbol{x}}(t)\right)\ \mathrm{tr}_B\left\{\hat{\boldsymbol{B}}(t)\hat{\boldsymbol{B}}(t')\overline{\rho}_B\right\}\\&+\left(\hat{\boldsymbol{\rho}}_S(t')\hat{\boldsymbol{x}}(t')\hat{\boldsymbol{x}}(t)-\hat{\boldsymbol{x}}(t)\hat{\boldsymbol{\rho}}_S(t')\hat{\boldsymbol{x}}(t')\right)\ \mathrm{tr}_B\left\{\hat{\boldsymbol{B}}(t')\hat{\boldsymbol{B}}(t)\overline{\rho}_B\right\}\ .\end{aligned} \tag{A.3}$$

The average

$$\mathrm{tr}_B\left\{\hat{\boldsymbol{B}}(t')\hat{\boldsymbol{B}}(t)\overline{\rho}_B\right\}=\mathrm{tr}_B\left\{\hat{\boldsymbol{B}}(t'-t)\hat{B}\ \overline{\rho}_B\right\}=C(t'-t), \tag{A.4}$$

is called the *reservoir correlation function*. It only depends on the time difference since

$$\left[\overline{\rho}_B,e^{\mathrm{i}\left(\hat{H}_S+\hat{H}_B\right)t}\right]=0. \tag{A.5}$$

Using the reservoir correlation functions and grouping the system quantities in Eq. (A.3) to commutators yields

$$\frac{\partial}{\partial t}\hat{\boldsymbol{\rho}}_S(t)=-\int_0^t\mathrm{d}t'\ \left\{\left[\hat{\boldsymbol{x}}(t),\hat{\boldsymbol{x}}(t')\hat{\boldsymbol{\rho}}_S(t')\right]C(t-t')+\left[\hat{\boldsymbol{\rho}}_S(t')\hat{\boldsymbol{x}}(t'),\hat{\boldsymbol{x}}(t)\right]C(t'-t)\right\}. \tag{A.6}$$

The bath correlation function is related to the in Eq. (A.21) introduced spectral density function $J(\omega)$ and the occupation number of Bose-Einstein statistics $n_B(\omega)$ by

$$C(\tau) \propto \int_{-\infty}^{\infty} \tilde{J}(\omega)(1+n_B(\omega))e^{-\mathrm{i}\omega\tau}\mathrm{d}\omega, \tag{A.7}$$

with $\tilde{J}(\omega)$ being the analytic continuation of $J(\omega)$ to negative frequencies via

$$\tilde{J}(\omega<0) = -J(-\omega). \tag{A.8}$$

Typical reservoirs have a dense spectrum so that $J(\omega)$ is approximately flat over large frequency scales. The Fourier transform of $\tilde{J}(\omega)(1+n_B(\omega))$, corresponding to the reservoir correlation function, is hence a sharply peaked function of τ and decays rapidly. Therefore, the Markov approximation is applicable, replacing $\rho_S(t') \to \rho_S(t)$, substituting $\tau = t - t'$ and sending the upper limit of the integral to infinity.

The Noise and Dissipation Kernel

Consider the trace in the second term of Eq. (4.34). Performing analogue steps to the calculation above yields

$$\begin{aligned}\mathrm{tr}_B\left\{\left[\hat{H}_I,\left[\hat{\boldsymbol{H}}_I(-\tau),\hat{\rho}_S(t)\otimes\overline{\rho}_B\right]\right]\right\} = &\left(\hat{x}\hat{\boldsymbol{x}}(-\tau)\hat{\rho}_S(t) - \hat{\boldsymbol{x}}(-\tau)\hat{\rho}_S(t)\hat{x}\right)C(\tau)\\ &+\left(\hat{\rho}_S(t)\hat{\boldsymbol{x}}(-\tau)\hat{x} - \hat{x}\hat{\rho}_S(t)\hat{\boldsymbol{x}}(-\tau)\right)C(-\tau)\ .\end{aligned} \tag{A.9}$$

We can rewrite $C(\tau) = \frac{1}{2}\left\{\left[C(\tau)-C(-\tau)\right] + \left[C(\tau)+C(-\tau)\right]\right\}$ and likewise $C(-\tau)$, which yields

$$\begin{aligned}\text{(A.9)} =&\frac{1}{2}\Big[C(\tau)-C(-\tau)\Big]\Big(+\hat{x}\hat{\boldsymbol{x}}(-\tau)\hat{\rho}_S(t) + \hat{x}\hat{\rho}_S(t)\hat{\boldsymbol{x}}(-\tau) - \hat{\boldsymbol{x}}(-\tau)\hat{\rho}_S(t)\hat{x}\\ &\qquad - \hat{\rho}_S(t)\hat{\boldsymbol{x}}(-\tau)\hat{x}\Big)\\ &+\frac{1}{2}\Big[C(\tau)+C(-\tau)\Big]\Big(\hat{x}\hat{\boldsymbol{x}}(-\tau)\hat{\rho}_S(t) - \hat{x}\hat{\rho}_S(t)\hat{\boldsymbol{x}}(-\tau) - \hat{\boldsymbol{x}}(-\tau)\hat{\rho}_S(t)\hat{x}\\ &\qquad + \hat{\rho}_S(t)\hat{\boldsymbol{x}}(-\tau)\hat{x}\Big)\ .\end{aligned} \tag{A.10}$$

The functions

$$D(\tau) := \mathrm{i}\Big[C(\tau)-C(-\tau)\Big] = \Big\langle[\hat{B},\hat{\boldsymbol{B}}(-\tau)]\Big\rangle, \tag{A.11}$$

$$D_1(\tau) := \Big[C(\tau)+C(-\tau)\Big] = \Big\langle\Big\{\hat{B},\hat{\boldsymbol{B}}(-\tau)\Big\}\Big\rangle \tag{A.12}$$

are called the *dissipation and noise kernel*. The position operator terms in Eq. (A.10) can be combined to

$$[\hat{x}, \{\hat{\boldsymbol{x}}(-\tau), \hat{\rho}_S(t)\}] = \hat{x}\hat{\boldsymbol{x}}(-\tau)\hat{\rho}_S(t) + \hat{x}\hat{\rho}_S(t)\hat{\boldsymbol{x}}(-\tau) - \hat{\boldsymbol{x}}(-\tau)\hat{\rho}_S(t)\hat{x} - \hat{\rho}_S(t)\hat{\boldsymbol{x}}(-\tau)\hat{x} \tag{A.13}$$

$$[\hat{x}, [\hat{\boldsymbol{x}}(-\tau), \hat{\rho}_S(t)]] = \hat{x}\hat{\boldsymbol{x}}(-\tau)\hat{\rho}_S(t) - \hat{x}\hat{\rho}_S(t)\hat{\boldsymbol{x}}(-\tau) - \hat{\boldsymbol{x}}(-\tau)\hat{\rho}_S(t)\hat{x} + \hat{\rho}_S(t)\hat{\boldsymbol{x}}(-\tau)\hat{x} \ . \tag{A.14}$$

Plugging Eqs. (A.13) and (A.14) into Eq. (A.10) yields for the trace of Eq. (A.9)

$$\begin{aligned} \mathrm{tr}_B \left\{ \left[\hat{H}_I, \left[\hat{\boldsymbol{H}}_I(-\tau), \hat{\rho}_S(t) \otimes \overline{\rho}_B\right]\right]\right\} = & -\frac{\mathrm{i}}{2} D(\tau) \Big[\hat{x}, \big\{\hat{\boldsymbol{x}}(-\tau), \hat{\rho}_S(t)\big\}\Big] \\ & + \frac{1}{2} D_1(\tau) \Big[\hat{x}, \big[\hat{\boldsymbol{x}}(-\tau), \hat{\rho}_S(t)\big]\Big] \ . \end{aligned} \tag{A.15}$$

We will now calculate expressions for $D(\tau)$ and $D_1(\tau)$. The interaction picture operator $\hat{\boldsymbol{B}}(-\tau)$ can be calculated by its definition

$$\begin{aligned} \hat{\boldsymbol{B}}(-\tau) = e^{\mathrm{i}\hat{H}_B(-\tau)} \hat{B} e^{-\mathrm{i}\hat{H}_B(-\tau)} &= e^{\mathrm{i}\hat{H}_B(-\tau)} \sum_n \kappa_n \sqrt{\frac{\hbar}{2m_n\omega_n}} \left(\hat{b}_n + \hat{b}_n^\dagger\right) e^{-\mathrm{i}\hat{H}_B(-\tau)} \\ &= \sum_n \kappa_n \sqrt{\frac{\hbar}{2m_n\omega_n}} \left(\hat{\boldsymbol{b}}_n(-\tau) + \hat{\boldsymbol{b}}_n^\dagger(-\tau)\right) \ . \end{aligned} \tag{A.16}$$

For the transformation of the bosonic creation and annihilation operators one can derive a differential equation

$$\begin{aligned} \frac{\mathrm{d}}{\mathrm{d}t}\hat{\boldsymbol{b}}_n(-\tau) = \frac{\mathrm{d}}{\mathrm{d}t}\left(e^{-\mathrm{i}\hat{H}_B\tau}\ \hat{b}_n\ e^{\mathrm{i}\hat{H}_B\tau}\right) &= -\mathrm{i}\ e^{-\mathrm{i}\hat{H}_B\tau}\ \left[\hat{H}_B, \hat{b}_n\right]\ e^{\mathrm{i}\hat{H}_B\tau} \\ &= \mathrm{i}\ e^{-\mathrm{i}\hat{H}_B\tau}\ \hat{b}_n\ e^{\mathrm{i}\hat{H}_B\tau} = \mathrm{i}\omega_n\hat{\boldsymbol{b}}_n \ , \end{aligned} \tag{A.17}$$

and solve it under the initial condition $\hat{\boldsymbol{b}}_n(0) = \hat{b}_n$. The solution to Eq. (A.17) is

$$\hat{\boldsymbol{b}}_n(-\tau) = \hat{b}_n e^{\mathrm{i}\omega_n\tau} \qquad \text{and therefore} \qquad \hat{\boldsymbol{b}}_n^\dagger(-\tau) = \hat{b}_n^\dagger e^{\mathrm{i}\omega_n\tau}, \tag{A.18}$$

with the creation operator being the complex conjugate of the annihilation operator. For $\hat{\boldsymbol{B}}(-\tau)$ we obtain

$$\hat{\boldsymbol{B}}(-\tau) = \sum_n \kappa_n \sqrt{\frac{\hbar}{2m_n\omega_n}} \left(\hat{b}_n e^{\mathrm{i}\omega\tau} + \hat{b}_n^\dagger e^{-\mathrm{i}\omega_n\tau}\right) \ . \tag{A.19}$$

Now we can calculate the commutator $[\hat{B}, \hat{\boldsymbol{B}}(-\tau)]$ to

$$\begin{aligned}
\left[\hat{B}, \hat{\boldsymbol{B}}(-\tau)\right] &= \sum_{n,k} \frac{\kappa_n \kappa_k}{2\sqrt{\omega_n \omega_k}} \left[\hat{b}_n^\dagger + \hat{b}_n, \hat{b}_k e^{\mathrm{i}\omega_k \tau} + \hat{b}_k^\dagger e^{-\mathrm{i}\omega_k \tau}\right] \\
&= \sum_{n,k} \frac{\kappa_n \kappa_k}{2\sqrt{\omega_n \omega_k}} \left\{ \left[\hat{b}_n^\dagger, \hat{b}_k\right] e^{\mathrm{i}\omega_k \tau} + \left[\hat{b}_n, \hat{b}_k^\dagger\right] e^{-\mathrm{i}\omega_k \tau} \right\} \\
&= \sum_{n,k} \frac{\kappa_n \kappa_k}{2\sqrt{\omega_n \omega_k}} \left\{ \delta_{nk} e^{-\mathrm{i}\omega_k \tau} - \delta_{nk} e^{\mathrm{i}\omega_k \tau} \right\} \\
&= \sum_{n} \frac{\kappa_n^2}{2\omega_n^2} \left\{ e^{-\mathrm{i}\omega_k \tau} - e^{\mathrm{i}\omega_k \tau} \right\} \\
&= -2\mathrm{i} \sum_{n} \frac{\kappa_n^2}{2\omega_n^2} \sin \omega_n \tau \ .
\end{aligned} \tag{A.20}$$

Since this is a constant $\langle [\hat{B}, \hat{\boldsymbol{B}}(-\tau)] \rangle = [\hat{B}, \hat{\boldsymbol{B}}(-\tau)]$. By introducing the reservoir spectral density

$$J(\omega) = \sum_n \frac{\kappa_n^2}{2\omega_n} \delta(\omega - \omega_n) \ , \tag{A.21}$$

the dissipation kernel $D(\tau)$ may be written as an integral

$$D(\tau) = 2 \int_0^\infty \mathrm{d}\omega \, J(\omega) \sin \omega \tau \ . \tag{A.22}$$

For the anticommutator we get

$$\begin{aligned}
\left\{\hat{B}, \hat{\boldsymbol{B}}(-\tau)\right\} &= \sum_{n,k} \frac{\kappa_n \kappa_k}{2\sqrt{\omega_n \omega_k}} \left\{\hat{b}_n^\dagger + \hat{b}_n, \hat{b}_k e^{\mathrm{i}\omega_k \tau} + \hat{b}_k^\dagger e^{-\mathrm{i}\omega_k \tau}\right\} \\
&= \sum_{n,k} \frac{\kappa_n \kappa_k}{2\sqrt{\omega_n \omega_k}} \Big[\left(\hat{b}_n^\dagger + \hat{b}_n\right) \left(\hat{b}_k e^{\mathrm{i}\omega_k \tau} + \hat{b}_k^\dagger e^{-\mathrm{i}\omega_k \tau}\right) \\
&\qquad + \left(\hat{b}_k e^{\mathrm{i}\omega_k \tau} + \hat{b}_k^\dagger e^{-\mathrm{i}\omega_k \tau}\right) \left(\hat{b}_n^\dagger + \hat{b}_n\right) \Big] \ .
\end{aligned} \tag{A.23}$$

When averaging, only creation-annihilation operator pairs will survive. In the thermal state $\overline{\rho}_B$ their expectation value is

$$\left\langle \hat{b}_k^\dagger \hat{b}_n \right\rangle = \delta_{kn} \ n_B(\omega_k) \qquad \text{or} \qquad \left\langle \hat{b}_k \hat{b}_n^\dagger \right\rangle = \delta_{kn} \ (n_B(\omega_k) + 1), \tag{A.24}$$

respectively. The occupation number $n_B(\omega_k)$ of frequency ω_k is given by Bose-Einstein statistics

$$n_B(\omega_k) = \frac{1}{e^{\beta \omega_k} - 1} \ . \tag{A.25}$$

The average of Eq. (A.23) yields

$$\begin{aligned}\left\langle\left\{\hat{B},\hat{\boldsymbol{B}}(-\tau)\right\}\right\rangle &= \sum_k \frac{\kappa_k^2}{2\omega_k^2}\left(\left\langle\hat{b}_k^\dagger\hat{b}_k\right\rangle e^{-\mathrm{i}\omega_k\tau}+\left\langle\hat{b}_k\hat{b}_k^\dagger e^{\mathrm{i}\omega_k\tau}\right\rangle\right)\\ &= \sum_k \frac{\kappa_k^2}{2\omega_k^2}\left(n_B(\omega_k)e^{-\mathrm{i}\omega_k\tau}+(n_B(\omega_k)+1)e^{\mathrm{i}\omega_k\tau}\right)\\ &= \sum_k \frac{\kappa_k^2}{2\omega_k^2}\left(\frac{1}{e^{\beta\omega_k}-1}e^{-\mathrm{i}\omega_k\tau}+\left(\frac{1}{e^{\beta\omega_k}-1}+1\right)e^{\mathrm{i}\omega_k\tau}\right)\\ &= \sum_k \frac{\kappa_k^2}{\omega_k^2}\coth(2\beta\omega_k)\cos(\omega_k\tau)\ .\end{aligned} \tag{A.26}$$

The noise kernel eventually becomes

$$D_1(\tau) = 2\int_0^\infty \mathrm{d}\omega\, J(\omega)\coth\left(2\beta\omega\right)\cos\left(\omega\tau\right)\ . \tag{A.27}$$

dτ−Integration

The evaluation of the integrals in Eq. (4.35) becomes possible after approximating $\hat{\boldsymbol{x}}(-\tau)$ by its free dynamics

$$\hat{\boldsymbol{x}}(-\tau) = \hat{x} - \hat{p}\tau\ . \tag{A.28}$$

Plugging this into Eq. (4.35) yields

$$\begin{aligned}\frac{1}{2}\int_0^\infty \mathrm{d}\tau\Bigg(&\mathrm{i}D(\tau)\Big[\hat{x},\{\hat{x},\hat{\rho}_S(t)\}\Big]-D_1(\tau)\Big[\hat{x},[\hat{x},\hat{\rho}_S(t)]\Big]\\ &-\mathrm{i}\tau D(\tau)\Big[\hat{x},\{\hat{p},\hat{\rho}_S(t)\}\Big]+\tau D_1(\tau)\Big[\hat{x},[\hat{p},\hat{\rho}_S(t)]\Big]\Bigg)\end{aligned} \tag{A.29}$$

The commutators are now independent of τ we can focus on integrating the noise and dissipation kernel. For this, the Heitler function

$$\int_0^\infty \mathrm{d}\tau e^{-\mathrm{i}\omega\tau} = \pi\delta(\omega)-\mathrm{i}\mathcal{P}\left(\frac{1}{\omega}\right)\ , \tag{A.30}$$

will be used multiple times. $\mathcal{P}$ denotes the Cauchy principal value. Performing the integration of the first term of (A.29) yields

$$\begin{aligned}
\frac{\mathrm{i}}{2}\int_0^\infty \mathrm{d}\tau\, D(\tau) &= \mathrm{i}\int_0^\infty\int_0^\infty \mathrm{d}\tau\,\mathrm{d}\omega\, J(\omega)\sin\omega\tau = \frac{1}{2}\int_0^\infty\int_0^\infty \mathrm{d}\tau\,\mathrm{d}\omega\, J(\omega)\left(e^{\mathrm{i}\omega\tau}-e^{-\mathrm{i}\omega\tau}\right)\\
&= \frac{1}{2}\int_0^\infty \mathrm{d}\omega\, J(\omega)\left(\pi\delta(-\omega)-\mathrm{i}\mathcal{P}\left(\frac{1}{-\omega}\right)-\pi\delta(\omega)+\mathrm{i}\mathcal{P}\left(\frac{1}{\omega}\right)\right)\\
&= \mathrm{i}\int_0^\infty \mathrm{d}\omega\, J(\omega)\mathcal{P}\left(\frac{1}{\omega}\right)\\
&= \mathrm{i}\sum_n \frac{\kappa_n^2}{2\omega_n}\int_0^\infty \mathrm{d}\omega\mathcal{P}\left(\frac{1}{\omega}\right)\delta(\omega-\omega_n)\\
&= \mathrm{i}\sum_n \frac{\kappa_n^2}{2\omega_n^2}\ .
\end{aligned} \tag{A.31}$$

So that

$$\frac{\mathrm{i}}{2}\int_0^\infty \mathrm{d}\tau\, D(\tau)\Big[\hat{x},\{\hat{x},\hat{\rho}_S(t)\}\Big] = \mathrm{i}\left[\hat{H}_c,\hat{\rho}_S(t)\right], \tag{A.32}$$

with the counter term from Eq. (4.27). The second term becomes

$$\begin{aligned}
\frac{1}{2}\int_0^\infty \mathrm{d}\tau\, D_1(\tau) &= \int_0^\infty\int_0^\infty \mathrm{d}\tau\,\mathrm{d}\omega\, J(\omega)\coth(2\beta\omega)\cos(\omega\tau)\\
&= \frac{1}{2}\int_0^\infty\int_0^\infty \mathrm{d}\tau\,\mathrm{d}\omega\, J(\omega)\coth(2\beta\omega)\left(e^{\mathrm{i}\omega\tau}+e^{-\mathrm{i}\omega\tau}\right)\\
&= \pi\int_0^\infty \mathrm{d}\omega\,\delta(\omega)J(\omega)\coth(2\beta\omega)\\
&= \pi\lim_{\omega\to 0} J(\omega)\coth(2\beta\omega)\ .
\end{aligned} \tag{A.33}$$

Now, the spectral density function is approximated by a smooth function of ω. The precise form of $J(\omega)$ depends on the bath. We will use an Ohmic spectral density with a cutoff function

$$J(\omega) = \frac{2\eta}{\pi}\frac{\Omega^2}{\Omega^2+\omega^2}\,\omega, \tag{A.34}$$

that suppresses frequencies that are larger than Ω. With this representation the limit in (A.33) can be performed so that the second integration eventually yields

$$-\frac{1}{2}\int_0^\infty \mathrm{d}\tau\, D_1(\tau)\Big[\hat{x},[\hat{x},\hat{\rho}_S(t)]\Big] = -2\eta k_B T\Big[\hat{x},[\hat{x},\hat{\rho}_S(t)]\Big]\ . \tag{A.35}$$

Moving on to the third term, the integration gives

$$\begin{aligned}\frac{\mathrm{i}}{2}\int_0^\infty \mathrm{d}\tau\,\tau D(\tau) &= \mathrm{i}\int_0^\infty\int_0^\infty \mathrm{d}\tau\,\mathrm{d}\omega\,J(\omega)\tau\sin\omega\tau \\ &= -\mathrm{i}\int_0^\infty \mathrm{d}\omega\,J(\omega)\frac{\partial}{\partial\omega}\int_0^\infty \mathrm{d}\tau\cos(\omega\tau) \\ &= -\mathrm{i}\pi\int_0^\infty \mathrm{d}\omega\,J(\omega)\frac{\partial}{\partial\omega}\delta(\omega) = -\mathrm{i}\pi\frac{\partial J(\omega)}{\partial\omega}\bigg|_{\omega=0}.\end{aligned} \tag{A.36}$$

Taking the derivative of Eq. (A.34), we find for the third term

$$-\frac{\mathrm{i}}{2}\int_0^\infty \mathrm{d}\tau\,\tau D(\tau)\Big[\hat{x},\{\hat{p},\hat{\rho}_S(t)\}\Big] = -\mathrm{i}\eta\Big[\hat{x},\{\hat{p},\hat{\rho}_S(t)\}\Big]\,. \tag{A.37}$$

The fourth term turns out to be small in comparison with Eq. (A.35) and its calculation is omitted here. Plugging the derived expressions back into Eq. (A.29) yields

$$\mathrm{i}\Big[\hat{H}_c,\hat{\rho}_S(t)\Big] - \mathrm{i}\eta\Big[\hat{x},\{\hat{p},\hat{\rho}_S(t)\}\Big] - 2\eta k_B T\Big[\hat{x},[\hat{x},\hat{\rho}_S(t)]\Big]\,. \tag{A.38}$$

Replacing the integral in Eq. (4.34) with this expression leads to the Caldeira-Legget master equation of Eq. (4.37). Note that the system Hamiltonian in Eq. (4.37) is again the pure system Hamiltonian without the counter term as it cancels out.

A.2 Benchmarks

Since an analytic solution of our model is intractable, proper benchmarks are vital to ensure the correctness of our simulation. Furthermore, the step size used to integrate the Langevin equations has to be analyzed to ensure convergence as well as avoiding discretization errors while being efficient. The Benchmarks that were conducted are the dynamics of independent harmonic oscillators coupled to a thermal reservoir, and the equilibrium distribution of particle pairs described by an Hamiltonian analogous to Eq. (4.53).

The equation that describes the time evolution of probability densities of Brownian motion is the *Fokker-Planck equation*. When talking about the probability density $p(x,v,t)$ in terms of particle velocity v and position x, it is often referred to as the *Klein-Kramers-* or *Smoluchowski* equation and written as

$$\frac{\partial}{\partial t}p(x,v,t) = \left(-\frac{\partial}{\partial x}v + \frac{\partial}{\partial v}\left(\eta v - \frac{1}{m}\frac{\partial}{\partial x}V(x)\right) + \frac{\eta k_B T}{m}\frac{\partial}{\partial v^2}\right)p(x,v,t)\,. \tag{A.39}$$

The Fokker-Planck equation and the Langevin Eqs. (4.21) and (4.22) are identical and can be converted into each other. The distribution of paths following Langevin equations result

in the probability distribution satisfying Eq. (A.39). The steady state distribution of the Fokker-Planck equation is the canonical distribution

$$p(x,v) \propto e^{\beta\left(\frac{1}{2}mv^2+V(x)\right)}, \tag{A.40}$$

allowing for an easy way to verify long term behavior.

A.2.1 Thermal Harmonic Oscillators

For a quadratic potential

$$V(x) = \tfrac{1}{2}\omega^2 x^2, \tag{A.41}$$

the Fokker-Planck equation is analytically solvable [89]. This makes it suitable to check correct dynamics of the simulation. The analytic solution for the second moment of $x(t)$ reads

$$\begin{aligned}\left\langle x^2\right\rangle(t) = \frac{\eta k_B T}{m(\lambda_+-\lambda_-)^2}\Bigg[&\frac{\lambda_++\lambda_-}{\lambda_+\lambda_-} + \frac{4}{\lambda_++\lambda_-}\left(e^{-(\lambda_++\lambda_-)t}-1\right)\\ &-\frac{1}{\lambda_+}e^{-2\lambda_+t}-\frac{1}{\lambda_-}e^{-2\lambda_-t}\Bigg],\end{aligned} \tag{A.42}$$

with

$$\lambda_\pm = \frac{1}{2}\left(\eta \pm \sqrt{\eta^2-4\omega^2}\right)\ . \tag{A.43}$$

In Fig. A.1 we compare $\langle x^2\rangle(t)$ calculated from 10^5 paths, simulated by either the Euler-Maruyama or the BBK method, with the theoretical result. The popular BBK algorithm with $\mathrm{d}\sigma = 0.05$ and the Euler-Maruyama method with $\mathrm{d}\sigma = 0.0005$ yield similar small deviations from the theoretical curve. This implies that the BBK method can be used up to much larger step sizes. Besides, the validity of both methods for thermal harmonic oscillators is given for small enough step sizes.

A.2.2 Two Interacting Particles in a Cosine Potential

The second benchmark has the purpose of verifying the correct behavior of the interaction as well as correct equilibration. We consider the one-dimensional version of Eq. (4.53) for two sites, so particle pairs in a cosine potential interacting via an XY interaction. The equilibrium distribution becomes a four-dimensional function $p(\vartheta_1,\vartheta_2,\omega_1,\omega_2)$. We expect that this distribution relaxes to the equilibrium distribution of the Fokker-Planck equation, so the canonical distribution. A suitable representation is achieved by integrating out the angular velocities and considering a cross section of a fixed interval $\left[\vartheta_2-\frac{1}{2}\mathrm{d}\vartheta_2, \vartheta_2+\frac{1}{2}\mathrm{d}\vartheta_2\right]$.

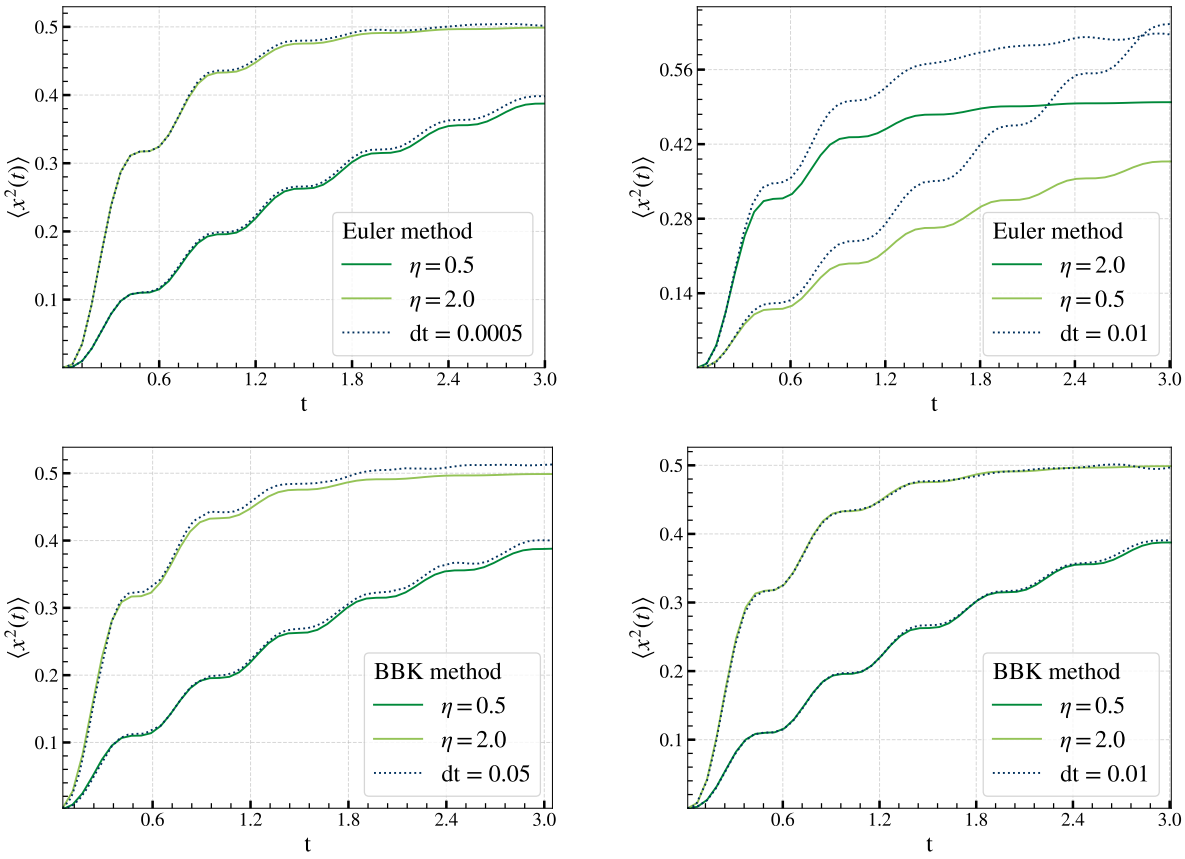

Figure A.1: The calculated $\langle x^2(t)\rangle$ of thermal harmonic oscillators are shown for different methods and step sizes. The green curves are the theoretical paths calculated from Eq. (A.42) for $\omega^2 = 20$, $T = 20$ and $m = 1$. The damping is denoted in the legend. The dotted lines are paths calculated from 10^5 simulated realizations. The top plots are calculated using the Euler-Maruyama method and the bottom plots using the BBK method. The Euler-Maruyama method with $\mathrm{d}t = 0.0005$ shows comparable discretization errors as the BBK method with $\mathrm{d}t = 0.05$, which is a difference of two orders of magnitude. For a step size of $\mathrm{d}t = 0.01$, the BBK method shows virtually no discretization errors, while the Euler-Maruyama method strongly deviates from the theoretical curve.

In Fig. A.2 we show cuts of the integrated probability density

$$p(\vartheta_1, \vartheta_2)\mathrm{d}\vartheta_2 = \int \mathrm{d}\omega_1\, \mathrm{d}\omega_2\, p(\vartheta_1, \vartheta_2, \omega_1, \omega_2)\mathrm{d}\vartheta_2, \tag{A.44}$$

with constant ϑ_2. It is verified that simple interacting systems are driven to their equilibrium. The statistical and discretization errors vanish for many samples and small step sizes $\mathrm{d}\sigma$.

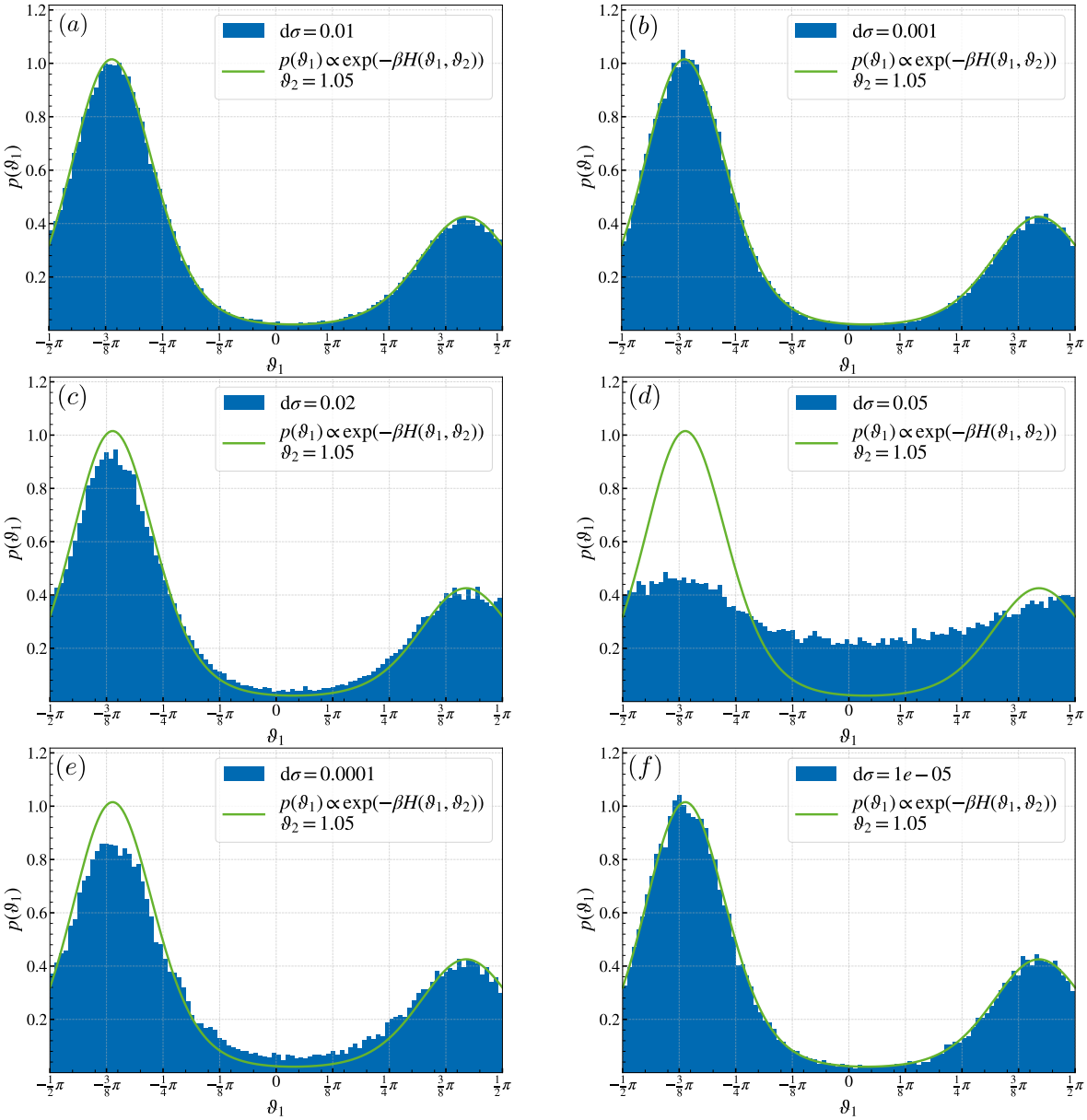

Figure A.2: The integrated probability distribution $p(\vartheta_1, \vartheta_2)\mathrm{d}\vartheta_2$ of particle pairs described by Eq. (4.53) around constant ϑ_2 is shown. The used parameters for (a) - (d) were $j = 40$, $\rho = 100$, $p = 2.5$, $\eta = 1$ and $\kappa = 100$. The interactions and temperatures are chosen to be larger than in the actual simulation on purpose. The green curve is the canonical distribution. The blue bins are calculated from $5 \cdot 10^5$ simulated pair paths by counting particles in $\left[\vartheta_2 - \frac{1}{2}\mathrm{d}\vartheta_2, \vartheta_2 + \frac{1}{2}\mathrm{d}\vartheta_2\right]$ and binning them into 100 sections. It was made sure that the systems were completely relaxed, meaning that the effects of the starting position vanished and the shape of the probability distribution did not change anymore. The integrations were performed using the BBK method. The BBK method again shows no discretization errors for $\mathrm{d}\sigma = 0.01$. Slightly larger step sizes of $\mathrm{d}t = 0.02$ already produce visually recognizable deviations. Simulations with $\mathrm{d}\sigma = 0.05$ deviate strongly. Almost no improvement is achieved by reducing the step size to $\mathrm{d}t = 0.001$. How small the step size has to be naturally depends on the system at hand, therefore the benchmark is repeated for parameters in the dimensions of the experimental coupling constants in (e) and (f). The coupling constants of the previous computations are multiplied with 10^4. For parameters in this order of magnitude, step sizes should not be larger than $\mathrm{d}\sigma = 10^{-5}$.

A.3 Correlation Length Calculation

The two-point equal time correlation function of the XY model in two dimensions is defined as

$$C(x,y) = \langle \vec{s}_{0,0}\vec{s}_{x,y} \rangle \ . \tag{A.45}$$

The brackets $\langle \cdot \rangle$ denote the ensemble average

$$\langle \vec{s}_{0,0}\vec{s}_{x,y} \rangle = \frac{1}{Z} \int \prod_i d\vartheta_i \vec{s}_{0,0}\vec{s}_{x,y} e^{-\beta H(\{\vartheta\})} \tag{A.46}$$

The correlation function decays exponentially for large distances above the critical temperature [90, 91], following

$$C(x,y) \sim e^{-r(x,y)/\xi(x,y)} \qquad \text{with} \qquad r(x,y) = \sqrt{x^2+y^2}. \tag{A.47}$$

This is the definition of the correlation length ξ. The correlation length is a measure for the length scale over which perturbations of a system relax in space. We are mainly interested in the correlation lengths in the directions along and across the dimer row and therefore define the correlation functions in these directions as

$$C_\perp(x) = \langle \vec{s}_{0,0}\vec{s}_{x,0} \rangle \sim e^{-x/\xi_\perp} \qquad \text{and} \qquad C_\parallel(y) = \langle \vec{s}_{0,0}\vec{s}_{0,y} \rangle \sim e^{-y/\xi_\parallel}. \tag{A.48}$$

Consider the Fourier transforms of $C_\delta(r)$

$$S_\delta(k) = \sum_r^{N_\delta - 1} C_\delta(r) e^{-2\pi \mathrm{i} \frac{kr}{N_\delta}} \ , \tag{A.49}$$

with N_δ being the number of lattice sites in the direction of δ. Set in the following $\delta = \perp$. The Fourier transform becomes

$$\begin{aligned} S_\perp(k) = \sum_x^{N_\perp - 1} C_\perp(x) e^{-2\pi \mathrm{i} \frac{kx}{N_\perp}} = \sum_x^{N_\perp - 1} \langle \vec{s}_{0,0}\vec{s}_{x,0} \rangle e^{-2\pi \mathrm{i} \frac{kx}{N_\perp}} = \sum_x^{N_\perp - 1} \langle s^0_{0,0} s^0_{x,0} \rangle e^{-2\pi \mathrm{i} \frac{kx}{N_\perp}} \\ + \sum_x^{N_\perp - 1} \langle s^1_{0,0} \ s^1_{x,0} \rangle e^{-2\pi \mathrm{i} \frac{kx}{N_\perp}}. \end{aligned} \tag{A.50}$$

The ensemble average can be computed by a sum over an infinite lattice

$$\langle s^\kappa_{0,0} s^\kappa_{x,0} \rangle = \lim_{N_\perp \to \infty} \lim_{N_\parallel \to \infty} \frac{1}{N_\perp N_\parallel} \sum_{i=0}^{N_\perp} \sum_{j=0}^{N_\parallel} s^\kappa_{i,j} s^\kappa_{i+x,j} \ , \tag{A.51}$$

where κ denotes the spin component. An approximation is possible by using a finite lattice with large dimensions N_δ. Inserting Eq. (A.51) into Eq. (A.50) and replacing the sum $\sum_x$ with a sum over $q = i + x$ yields

$$S_\perp(k) = \frac{1}{N_\perp N_\parallel} \sum_{\kappa,q,i,j} s^\kappa_{i,j} s^\kappa_{q,j} e^{-2\pi \mathrm{i} \frac{k(q-i)}{N_\perp}} = \frac{1}{N_\perp N_\parallel} \sum_{\kappa,q,i,j} \left(\sum_{p=0}^{N_\parallel} \delta_{p,j} \right) s^\kappa_{i,j} s^\kappa_{q,p} e^{-2\pi \mathrm{i} \frac{k(q-i)}{N_\perp}} \ . \quad \text{(A.52)}$$

In the second step we have inserted a productive one in the form of a sum over a Kronecker delta. The Kronecker delta can be written as a sum over complex exponentials

$$\delta_{p,j} = \frac{1}{N_\parallel} \sum_{l=1}^{N_\parallel} e^{2\pi \mathrm{i} \frac{l(j-p)}{N_\parallel}} \ . \quad \text{(A.53)}$$

Inserting this representation into Eq. (A.52) gives

$$\begin{aligned} S_\perp(k) &= \frac{1}{N_\perp N_\parallel^2} \sum_l \sum_\kappa \sum_{q,p,i,j} s^\kappa_{i,j} s^\kappa_{q,p} e^{-2\pi \mathrm{i} \frac{k(q-i)}{N_\perp}} e^{2\pi \mathrm{i} \frac{l(p-j)}{N_\parallel}} \\ &= \frac{1}{N_\perp N_\parallel^2} \sum_l \sum_\kappa \left(\sum_{i,j} s^\kappa_{i,j} e^{2\pi \mathrm{i} \left(\frac{ki}{N_\perp} + \frac{lj}{N_\parallel} \right)} \right) \left(\sum_{q,p} s^\kappa_{q,p} e^{-2\pi \mathrm{i} \left(\frac{kq}{N_\perp} + \frac{lp}{N_\parallel} \right)} \right) \ . \end{aligned} \quad \text{(A.54)}$$

The expressions in the parentheses are the Fourier transforms $\tilde{s}^\kappa_{k,l}$, or respectively the conjugated Fourier transform, of the $s^\kappa_{i,j}$ lattice:

$$\begin{aligned} S_\perp(k) &= \frac{1}{N_\perp N_\parallel^2} \sum_l \sum_\kappa \left(\tilde{s}^\kappa_{k,l} \right)^* \tilde{s}^\kappa_{k,l} \\ &= \frac{1}{N_\perp N_\parallel^2} \left(\sum_l |\tilde{s}^0_{k,l}|^2 + \sum_l |\tilde{s}^1_{k,l}|^2 \right) \ . \end{aligned} \quad \text{(A.55)}$$

This way we can calculate $S_\perp(k)$ by calculating the two dimensional Fourier transforms of the lattices $s^0_{i,j} = \cos \vartheta_{i,j}$ and $s^1_{i,j} = \sin \vartheta_{i,j}$. The analogue result is valid for $S_\parallel(k)$.

To eventually extract the correlation length, we consider again Eq. (A.52) and insert the asymptotic behavior of $C_\delta(r)$ Eq. (A.48) to obtain

$$S_\delta(k) \sim \sum_r^{N_\delta - 1} e^{-|r|/\xi_\delta} e^{-2\pi \mathrm{i} \frac{kr}{N_\delta}} = \frac{2\xi_\delta}{1 + 4\pi^2 \xi_\delta^2 k^2} \ , \quad \text{(A.56)}$$

showing that $S_\delta(k)$ behaves like a Lorentzian function around $k = 0$. Calculating $S_\delta(k)$ by means of Eq. (A.55) and fitting to the Lorentzian Eq. (A.56) yields ξ_δ as fitting parameter. Since Eq. (A.47) is valid for large r, it is important to only fit the peak of $S_\delta(k)$ around $k = 0$.

Correlations below the critical temperature in the Ising universality class can be shown [62] to decay like

$$C(x,y) \sim c + e^{-r(x,y)/\xi(x,y)}, \tag{A.57}$$

with a positive constant c. When performing the Fourier transform, this constant contributes to a delta peak at $k = 0$. To correctly extract correlation lengths below T_c, the $S_\delta(k = 0)$ value has to be cut.

A.4 Error Calculation on Moving Averages

An average $\overline{f}$ that is calculated by the means of Eq. (5.30) has a non-trivial relationship with its variance $\sigma_{\overline{f}}$ [92]. The reason for this is that $f(t)$ and $f(t + m\mathrm{d}t)$ might be, and most probably are, correlated. Observables at different points in time are dependent on each other and have to be treated accordingly.

The average $\overline{f}$ of a time series $f(s)$ is calculated as

$$f_\tau := \overline{f} = \frac{1}{\tau}\int_0^\tau \mathrm{d}s f(s) \ , \tag{A.58}$$

with τ being the duration of the observation. To estimate the error on f_τ we consider the variance of the average f_τ [56, 93]

$$\begin{aligned} \sigma_{\overline{f}}^2 &= \left\langle f_\tau^2 \right\rangle - \left\langle f_\tau \right\rangle^2 \\ &\approx \frac{1}{\tau}\int_{-\infty}^{\infty} \mathrm{d}t \ C_f(t), \end{aligned} \tag{A.59}$$

with $C_f(t)$ being the autocorrelation or time correlation function

$$C_f(t) = \langle f(s) f(s+t) \rangle - \langle f(s) \rangle^2 \ . \tag{A.60}$$

The step performed in Eq. (A.59) is valid in the limit that the sampling time is much larger than the characteristic decay time of the autocorrelation function τ_C. The so called *integrated autocorrelation time* τ_C is defined as

$$\tau_C = \frac{1}{2}\int_{-\infty}^{\infty} \mathrm{d}t \ C_f(t)/C_f(0) \ . \tag{A.61}$$

The variance $\sigma_{\overline{f}}^2$ is expressed in terms of τ_C as

$$\sigma_{\overline{f}}^2 = \frac{2\tau_C}{\tau} C_f(0) \ . \tag{A.62}$$

Considering Eq. (A.60) shows that $C_f(0)$ reduces to the variance of f

$$C_f(0) = \sigma_f^2 \ . \tag{A.63}$$

Rewriting $\tau = n_s \tau_s$ with n_s being the number of measured samples and τ_s being the time between the samples, the variance of the mean $\overline{f}$ can be expressed as

$$\sigma_{\overline{f}}^2 = \frac{2\tau_C}{\tau_s} \frac{\sigma_f^2}{n_s} \ , \tag{A.64}$$

revealing that the variance of $\overline{f}$ is by a factor of $2\tau_c/\tau_s$ larger than the naive approach of uncorrelated measurements. Since it is practically not possible to integrate Eq. (A.61) from $-\infty$ to ∞, we approximate τ_c by

$$\tau_C \approx \frac{1}{2} \int_{-\tau/2}^{\tau/2} \mathrm{d}t \ C_f(t)/C_f(0) \ . \tag{A.65}$$

A.5 The Role of p

The role of the parameter p of Eq. (4.53) fell a bit short in previous discussion and represents an interesting topic for further research. Put simply, p determines the location of the minimum of the symmetry-breaking field, but also influences the height of the potential barrier as can be seen in Fig. 4.4. It has been tested that variation of p does not change the critical behavior of the system. Results like the phase diagram might have to be reformulated in terms of the potential barrier

$$E_B = h \left(1 + \cos\left(\frac{\pi}{2} p\right)\right) , \tag{A.66}$$

if p is varied.

For the antiferromagnetic, symmetry-broken XY model, the equilibrium position of the dimers is determined by the strength of repulsion $J_\parallel$ and $J_\perp$, the amplitude of the symmetry-breaking field h and the location of its minima determined by p. In the case of ferromagnetic interaction, the equilibrium position is solely determined by p. We require that $p > 2$ as $p = 2$ reduces the number of minima to one. In addition, DFT calculations show that even the asymmetric $p(2 \times 1)$ lowers the energy, implying the existence of at least two minima. The repulsion between the dimers increases the buckling angle with respect to the minima of the symmetry-breaking field. To ensure that the buckling angle is not inherently larger than the experimental value, p should be chosen accordingly. In case of the approximated equilibrium angle of Eq. (5.19), the two constrains conclude to $p \in (2, 2.5]$.

Consider now a specific lattice site of a system in $c(4\times2)$ configuration, i.e, the site's buckling angle is $\vartheta = \vartheta^* = 72°$ and the buckling angle of all its neighbors is $\vartheta_{NN} = -\vartheta^*$. The condition that in equilibrium $\frac{\partial V(\vartheta)}{\partial \vartheta}\Big|_{\vartheta=\vartheta^*} = 0$ with potential derivative as in Eq. (4.57) yields

$$-4\sin(4\vartheta^*)\left(\frac{J_\parallel + J_\perp}{h}\right) = p\sin\left(\vartheta^* p\right) \ . \tag{A.67}$$

This transcendental equation for p in dependence of the coupling parameters and the desired equilibrium angle is not guaranteed to have a solution. The left-hand side is unbound but the right hand-side is bound by p. For the experimental values we find

$$\frac{J_\parallel + J_\perp}{h} < \frac{1}{3} \ , \tag{A.68}$$

so that it is even possible to find a p that reproduces the experimental equilibrium position.

A.6 Soft- and Hardware

Table A.1: The details and version numbers to the used soft- and hardware are listed.

Tool	version / model number
Cuda	
cuRAND	11.2
cuFFT	
GCC	10.2.0
C++	C++17
Boost	1.78.0
OS	CentOS Linux 7.9.2009
CPU	Intel(R) Xeon(R) Gold 6148
GPU	Nvidia P100, V100, A100

B Bibliography

[1] Jarek Dabrowski et al. *Silicon surfaces and formation of interfaces: basic science in the industrial world*. World Scientific, 2000.

[2] Paul Siffert and Eberhard Krimmel. *Silicon: evolution and future of a technology*. Springer Science & Business Media, 2013.

[3] Haissam El-Aawar. Increasing the transistor count by constructing a two-layer crystal square on a single chip. *AIRCC's International Journal of Computer Science and Information Technology*, pages 97–105, 2015.

[4] Seung-Yoon Kim, Sung-Yool Choi, Wan Sik Hwang, and Byung Jin Cho. Valley-engineered ultra-thin silicon for high-performance junctionless transistors. *Scientific Reports*, 6(1):29354, 2016.

[5] SS Barsanov. A systematic presentation of atomic radii. *Journal of structural chemistry*, 3(5):590–603, 1962.

[6] Eite Tiesinga, Peter J Mohr, David B Newell, and Barry N Taylor. CODATA recommended values of the fundamental physical constants: 2018. *Journal of Physical and Chemical Reference Data*, 50(3), 2021.

[7] A Ramstad, G Brocks, and PJ Kelly. Theoretical study of the Si(100) surface reconstruction. *Physical Review B*, 51(20):14504, 1995.

[8] Devina Pillay, Brett Stewart, Chee Burm Shin, and Gyeong S Hwang. Revisit to the Ising model for order–disorder phase transition on Si(001). *Surface science*, 554(2-3):150–158, 2004.

[9] M Matsumoto, K Fukutani, and T Okano. Low-energy electron diffraction study of the phase transition of Si(001) surface below 40 K. *Physical review letters*, 90(10):106103, 2003.

[10] Hiroshi Tochihara, Takaaki Amakusa, and Masashi Iwatsuki. Low-temperature scanning-tunneling-microscopy observations of the Si(001) surface with a low surface-defect density. *Physical Review B*, 50(16):12262, 1994.

[11] Gernot Schaller, Friedemann Queisser, Seyedeh Parya Katoorani, Christian Brand, Christian Kohlfürst, Mark R Freeman, Alfred Hucht, Peter Kratzer, Björn Sothmann, Michael Horn-von Hoegen, et al. Sequential Kibble-Zurek dynamics in the anisotropic Ising model of the Si (001) surface. *arXiv preprint arXiv:2310.18216*, 2023.

[12] Christian Brand, Alfred Hucht, Hamid Mehdipour, Giriraj Jnawali, Jonas D Fortmann, Mohammad Tajik, Rüdiger Hild Björn Sothmann, Peter Kratzer, Ralf Schützhold, and Michael Horn-von Hoegen. Critical behavior of the dimerized Si(001) surface: A continuous order-disorder phase transition in the 2D Ising universality class. *arXiv preprint arXiv:2310.10488*, 2023.

[13] Takeshi Tabata, Tetsuya Aruga, and Yoshitada Murata. Order-disorder transition on Si(001): c (4×2) to (2×1). *Surface Science Letters*, 179(1):L63–L70, 1987.

[14] Thomas W. B. Kibble. Topology of cosmic domains and strings. *Journal of Physics A: Mathematical and General*, 9(8):1387, 1976.

[15] Wojciech H. Zurek. Cosmological experiments in superfluid helium? *Nature*, 317(6037):505–508, 1985.

[16] Wojciech H. Zurek. Cosmological experiments in condensed matter systems. *Physics Reports*, 276(4):177–221, 1996.

[17] F. J. Himpsel and D. E. Eastman. Photoemission studies of intrinsic surface states on Si(100). *Journal of Vacuum Science and Technology*, 16(5):1297–1299, 1979.

[18] R. I. G. Uhrberg, G. V. Hansson, J. M. Nicholls, and S. A. Flodström. Experimental studies of the dangling-and dimer-bond-related surface electron bands on Si(100)(2×1). *Physical Review B*, 24(8):4684, 1981.

[19] Koichi Handa, Suminori Kono, Keijiro Saku, Jun Sasaki, Tomoki Kawano, Yasushi Sasaki, Tadayuki Hiroki, and Kikuo Arakawa. Plasma fibrinogen levels as an independent indicator of severity of coronary atherosclerosis. *Atherosclerosis*, 77(2-3):209–213, 1989.

[20] D. J. Chadi. Atomic and electronic structures of reconstructed Si(100) surfaces. *Physical Review Letters*, 43(1):43, 1979.

[21] Inder P. Batra. Atomic structure of the Si(001)-(2×1) surface. *Physical Review B*, 41(8):5048, 1990.

[22] Jaroslaw Dabrowski and Matthias Scheffler. Self-consistent study of the electronic and structural properties of the clean Si(001)(2×1) surface. *Applied Surface Science*, 56:15–19, 1992.

[23] Kouichirou Inoue, Y. Morikawa, K. Terakura, and M. Nakayama. Order-disorder phase transition on the Si(001) surface: Critical role of dimer defects. *Physical Review B*, 49(20):14774, 1994.

[24] Erik Landemark, C. J. Karlsson, Y.-C. Chao, and R. I. G. Uhrberg. Core-level spectroscopy of the clean Si(001) surface: Charge transfer within asymmetric dimers of the 2×1 and c(4×2) reconstructions. *Physical review letters*, 69(10):1588, 1992.

[25] Ben Mills. Wikipedia. 2024. "silicon". the silicon atoms are replaced by own color gradients. dimerization arrows, coordinate system and lattice constant added. Retrieved from `https://en.wikipedia.org/wiki/Silicon`, 2024.

[26] Masakazu Kubota and Yoshitada Murata. Streak patterns in low-energy electron diffraction on Si(001). *Physical Review B*, 49(7):4810, 1994.

[27] Robert A Wolkow. Direct observation of an increase in buckled dimers on Si(001) at low temperature. *Physical review letters*, 68(17):2636, 1992.

[28] Christian Brand, Alfred Hucht, Giriraj Jnawali, Jonas D Fortmann, Björn Sothmann, Hamid Mehdipour, Peter Kratzer, Ralf Schützhold, and Michael Horn-von Hoegen. Dimer Coupling Energies of the Si(001) Surface. *Physical Review Letters*, 130(12):126203, 2023.

[29] J. Ihm, D. H. Lee, J. D. Joannopoulos, and J. J. Xiong. Structural phase diagrams for the surface of a solid: a total-energy, renormalization-group approach. *Physical review letters*, 51(20):1872, 1983.

[30] Alfred B. Bortz, Malvin H. Kalos, and Joel L. Lebowitz. A new algorithm for Monte Carlo simulation of Ising spin systems. *Journal of Computational Physics*, 17(1):10–18, 1975.

[31] Nigel Goldenfeld. *Lectures on phase transitions and the renormalization group*. CRC Press, 2018.

[32] Leo P. Kadanoff. Scaling laws for Ising models near T_c. *Physics Physique Fizika*, 2(6):263, 1966.

[33] Andrea Pelissetto and Ettore Vicari. Critical phenomena and renormalization-group theory. *Physics Reports*, 368(6):549–727, 2002.

[34] Franz J Wegner. Corrections to scaling laws. *Physical Review B*, 5(11):4529, 1972.

[35] C. Domb M. S. Green J. L. Lebowitz. *Phase Transitions and Critical Phenomena. Vol. 8*. 1983.

[36] H. W. J. Blote, Erik Luijten, and Jouke R. Heringa. Ising universality in three dimensions: a Monte Carlo study. *Journal of Physics A: Mathematical and General*, 28(22):6289, 1995.

[37] Kurt Binder. Finite size scaling analysis of Ising model block distribution functions. *Zeitschrift für Physik B Condensed Matter*, 43:119–140, 1981.

[38] Massimo Campostrini, Martin Hasenbusch, Andrea Pelissetto, Paolo Rossi, and Ettore Vicari. Critical behavior of the three-dimensional XY universality class. *Physical Review B*, 63(21):214503, 2001.

[39] Kurt Binder. Critical properties from Monte Carlo coarse graining and renormalization. *Physical Review Letters*, 47(9):693, 1981.

[40] D. P. Landau. Non-universal critical behavior in the planar XY-model with fourth order anisotropy. *Journal of Magnetism and Magnetic Materials*, 31:1115–1116, 1983.

[41] W. Bernreuther and M. Göckeler. An investigation of the phase structure of the two-dimensional O(2) and O(4) symmetric nonlinear sigma-models. *Physics Letters B*, 214(1):109–114, 1988.

[42] Pierre C. Hohenberg and Bertrand. I. Halperin. Theory of dynamic critical phenomena. *Reviews of Modern Physics*, 49(3):435, 1977.

[43] V. M. H. Ruutu, V. B. Eltsov, A. J. Gill, T. W. B. Kibble, M. Krusius, Yu G. Makhlin, B. Placais, G. E. Volovik, and Wen Xu. Vortex formation in neutron-irradiated superfluid ^{3}He as an analogue of cosmological defect formation. *Nature*, 382(6589):334–336, 1996.

[44] S. Ulm, J. Roßnagel, G. Jacob, C. Degünther, S. T. Dawkins, U. G. Poschinger, R. Nigmatullin, A. Retzker, M. B. Plenio, F. Schmidt-Kaler, et al. Observation of the Kibble–Zurek scaling law for defect formation in ion crystals. *Nature communications*, 4(1):2290, 2013.

[45] K Pyka, J Keller, HL Partner, R Nigmatullin, T Burgermeister, DM Meier, K Kuhlmann, A Retzker, Martin B Plenio, WH Zurek, et al. Topological defect formation and spontaneous symmetry breaking in ion Coulomb crystals. *Nature communications*, 4(1):2291, 2013.

[46] E Rastelli, S Regina, and A Tassi. Monte Carlo simulation of a planar rotator model with symmetry-breaking fields. *Physical Review B*, 69(17):174407, 2004.

[47] Alan M. Ferrenberg and D. P. Landau. three-dimensional Ising model: A high-resolution Monte Carlo study. *Physical Review B*, 44(10):5081, 1991.

[48] Martin Hasenbusch. The two-dimensional XY model at the transition temperature: a high-precision Monte Carlo study. *Journal of Physics A: Mathematical and General*, 38(26):5869, 2005.

[49] Pablo Laguna and Wojciech Hubert Zurek. Density of kinks after a quench: When symmetry breaks, how big are the pieces? *Physical Review Letters*, 78(13):2519, 1997.

[50] Daniel T Gillespie. The mathematics of Brownian motion and Johnson noise. *American Journal of Physics*, 64(3):225–240, 1996.

[51] Albert Einstein. Über die von der molekularkinetischen Theorie der Wärme geforderte Bewegung von in ruhenden Flüssigkeiten suspendierten Teilchen. *Annalen der physik*, 4, 1905.

[52] Paul Langevin. Sur la théorie du mouvement brownien. *Compt. Rendus*, 146:530–533, 1908.

[53] Amir O. Caldeira and Anthony J. Leggett. Influence of dissipation on quantum tunneling in macroscopic systems. *Physical Review Letters*, 46(4):211, 1981.

[54] Gabriel T. Landi, Dario Poletti, and Gernot Schaller. Nonequilibrium boundary-driven quantum systems: Models, methods, and properties. *Reviews of Modern Physics*, 94(4):045006, 2022.

[55] Peter E. Kloeden and Eckhard Platen. *Stochastic differential equations*. Springer, 1992.

[56] Daan Frenkel and Berend Smit. *Understanding molecular simulation: from algorithms to applications*. Elsevier, 2023.

[57] L. Larini, Riccardo Mannella, and Dino Leporini. Langevin stabilization of molecular-dynamics simulations of polymers by means of quasisymplectic algorithms. *The Journal of Chemical Physics*, 126(10), 2007.

[58] Axel Brünger, Charles L. Brooks III, and Martin Karplus. Stochastic boundary conditions for molecular dynamics simulations of ST2 water. *Chemical physics letters*, 105(5):495–500, 1984.

[59] Jesús A. Izaguirre, Daniel P. Catarello, Justin M. Wozniak, and Robert D. Skeel. Langevin stabilization of molecular dynamics. *The Journal of chemical physics*, 114(5):2090–2098, 2001.

[60] W. H. Press, S. A. Teukolsky, W. T. Vetterling, and B. P. Flannery. Numerical recipes in C++. *The Art of Scientific Computing, second ed., Cambridge University Press, Cambridge*, 2002.

[61] Lars Onsager. Crystal statistics. I. A two-dimensional model with an order-disorder transition. *Physical Review*, 65(3-4):117, 1944.

[62] Barry M. McCoy and Tai Tsun Wu. *The two-dimensional Ising model*. Harvard University Press, 1973.

[63] M. P. Nightingale and H. W. J. Blöte. Monte Carlo computation of correlation times of independent relaxation modes at criticality. *Physical Review B*, 62(2):1089, 2000.

[64] L. Ts. Adzhemyan, D. A. Evdokimov, M. Hnatič, E. V. Ivanova, M. V. Kompaniets, A. Kudlis, and D. V. Zakharov. The dynamic critical exponent z for 2d and 3d Ising models from five-loop ε expansion. *Physics Letters A*, 425:127870, 2022.

[65] Charlie Duclut and Bertrand Delamotte. Frequency regulators for the nonperturbative renormalization group: A general study and the model A as a benchmark. *Physical Review E*, 95(1):012107, 2017.

[66] B. Dammann and J. D. Reger. Dynamical critical exponent of the two-dimensional Ising model. *Europhysics Letters*, 21(2):157, 1993.

[67] John Cardy. *Scaling and renormalization in statistical physics*, volume 5. Cambridge university press, 1996.

[68] Renfrey Burnard Potts. Some generalized order-disorder transformations. In *Mathematical proceedings of the cambridge philosophical society*, volume 48, pages 106–109. Cambridge University Press, 1952.

[69] Daniel C. Mattis. Transfer matrix in plane-rotator model. *Physics Letters A*, 104(6-7):357–360, 1984.

[70] N. David Mermin and Herbert Wagner. Absence of ferromagnetism or antiferromagnetism in one-or two-dimensional isotropic Heisenberg models. *Physical Review Letters*, 17(22):1133, 1966.

[71] J. M. Kosterlitz and D. J. Thouless. Ordering, metastability and phase transitions in two-dimensional systems. *Journal of Physics C: Solid State Physics*, 6(7):1181, apr 1973.

[72] V. L. Berezinskii. Destruction of long-range order in one-dimensional and two-dimensional systems having a continuous symmetry group I. Classical systems. *Sov. Phys. JETP*, 32(3):493–500, 1971.

[73] A. A. Migdal. Phase transitions in gauge and spin-lattice systems. *Zh. Eksp. Teor. Fiz*, 69:1457, 1975.

[74] Jorge V. José, Leo P. Kadanoff, Scott Kirkpatrick, and David R. Nelson. Renormalization, vortices, and symmetry-breaking perturbations in the two-dimensional planar model. *Physical Review B*, 16(3):1217, 1977.

[75] Shuai Che, Michael Boyer, Jiayuan Meng, David Tarjan, Jeremy W. Sheaffer, and Kevin Skadron. A performance study of general-purpose applications on graphics processors using CUDA. *Journal of parallel and distributed computing*, 68(10):1370–1380, 2008.

[76] NVIDIA, Péter Vingelmann, and Frank H. P. Fitzek. CUDA, release: 10.2.89, 2020.

[77] Thrust Development Team. Thrust: The C++ parallel algorithms library, 2023.

[78] Karsten Ahnert, Denis Demidov, and Mario Mulansky. Solving ordinary differential equations on GPUs. In *Numerical Computations with GPUs*, pages 125–157. Springer, 2014.

[79] M. Aizenman and B. Simon. A comparison of plane rotor and Ising models. *Physics Letters A*, 76(3-4):281–282, 1980.

[80] Chu-Chun Fu, Mariana Weissmann, and Andrés Saúl. Molecular dynamics study of dimer flipping on perfect and defective Si(001) surfaces. *Surface science*, 494(2):119–130, 2001.

[81] Chengcheng Xiao, Xinwei Wang, Xiaodong Pi, Shengyuan A. Yang, Yuanping Feng, Yunhao Lu, and Shengbai Zhang. Spontaneous symmetry lowering of Si(001) towards two-dimensional ferro/antiferroelectric behavior. *Physical Review Materials*, 3(4):044410, 2019.

[82] John P. Perdew, Adrienn Ruzsinszky, Gábor I Csonka, Oleg A Vydrov, Gustavo E Scuseria, Lucian A Constantin, Xiaolan Zhou, and Kieron Burke. Restoring the density-gradient expansion for exchange in solids and surfaces. *Physical review letters*, 100(13):136406, 2008.

[83] P. Kratzer. private communication.

[84] Kay White Vugrin, Laura Painton Swiler, Randall M. Roberts, Nicholas J. Stucky-Mack, and Sean P. Sullivan. Confidence region estimation techniques for nonlinear regression in groundwater flow: Three case studies. *Water Resources Research*, 43(3), 2007.

[85] Z. B. Li, L. Schülke, and B. Zheng. Dynamic monte carlo measurement of critical exponents. *Physical review letters*, 74(17):3396, 1995.

[86] H. K. Janssen, B. Schaub, and B. Schmittmann. New universal short-time scaling behaviour of critical relaxation processes. *Zeitschrift für Physik B Condensed Matter*, 73:539–549, 1989.

[87] Björn Ladewig, Steven Mathey, and Sebastian Diehl. Kibble-Zurek mechanism from different angles: The transverse XY model and subleading scalings. *Physical Review B*, 102(10):104306, 2020.

[88] Yukiyasu Ozeki and Nobuyasu Ito. Nonequilibrium relaxation method. *Journal of Physics A: Mathematical and Theoretical*, 40(31):R149, 2007.

[89] Hannes Risken. *Fokker-planck equation*. Springer, 1996.

[90] J. M. Kosterlitz. The critical properties of the two-dimensional XY model. *Journal of Physics C: Solid State Physics*, 7(6):1046, 1974.

[91] S. Grinstein. Renormalisation group analysis of the phase transition in the 2D Coulomb gas, Sine-Gordon theory and XY-model. *Journal of Physics A: Mathematical and General*, 13(2):585, 1980.

[92] Neal Madras and Alan D. Sokal. The pivot algorithm: A highly efficient Monte Carlo method for the self-avoiding walk. *Journal of Statistical Physics*, 50:109–186, 1988.

[93] Theodore W. Anderson. The statistical analysis of time series. pages 438–450, 2011.

Acknowledgement

I would like to thank Prof. Ralf Schützhold for providing me with the opportunity to write this thesis at the Helmholtz-Zentrum Dresden-Rossendorf, opening up insights into the large research collaboration CRC 1242. I would like to thank Dr. Gernot Schaller as well as Dr. Friedemann Queisser for their excellent supervision during this project. Our weekly meetings acted as signposts on the path that eventually led to this work. I would like to thank Dr. Christian Kohlfürst for always caring about IT- and organizational matters and for exquisite company in the office. Also, I would like to thank Prof. Roland Ketzmerick for agreeing to review my thesis.

My deepest gratitude goes towards Kathi for supplying me with daily nutritious and delicious meals, especially in the finishing phase of this project. Without her, this level of investment would not have been possible. I would like to thank Julian and Mau for helpful suggestions and proofreading. I want to thank Kira for employing her english expertise to check my spelling and grammer. Finally, I would like to thank my brother Martin and Adrian for their generous self-sacrifice, voluntarily offering to proofread 100 pages of a theoretical physics master's thesis.

Erklärung

Hiermit erkläre ich, dass ich diese Arbeit im Rahmen der Betreuung am Institut für Theoretische Physik ohne unzulässige Hilfe Dritter verfasst und alle Quellen als solche gekennzeichnet habe.

Andreas Weitzel
Dresden, April 2024